High-Speed Tunable Short-Wavelength VCSEL for Optical Interconnects

Dem Fachbereich Elektrotechnik und Informationstechnik
der Technischen Universität Darmstadt
zur Erlangung des akademischen Grades eines
Doktor-Ingenieurs (Dr. -Ing.)
genehmigte Dissertation

von

Dipl. -Ing. Hooman Abdollahzadeh Davani
geboren am 05.04.1981 in Teheran, I.R. Iran

Referent	:	Prof. Dr. -Ing. Peter Meißner
Korreferent	:	Prof. Dr. -Ing. Helmut F. Schlaak
Tag der Einreichung	:	22.04.2014
Tag der mündlichen Prfüng	:	28.10.2014

D17
Darmstadt 2015

To my grandmother Fatemeh Enayatollah

Preface

This dissertation is a summary and a precious memory of my research in the Institute of Microwave Engineering and Photonics of the Technische Universität Darmstadt.
First of all I would like to express my gratitude to my supervisor Prof. Dr. -Ing. Peter Meißner.
My sincere appreciation goes also to my co-examiner Prof. Dr. -Ing. Helmut F. Schlaak.
For the inspiring discussions and constructive cooperation, my fellow colleagues in the Institute of Microwave Engineering and Optics are warmly thanked. Especially, I deeply appreciate Dr. Christian Gierl, Karolina Zogal, Dr. Sandro Jatta, Dr. Benjamin Kögel, Dr. Yuliang Zheng. Dr. Mohsen Sazegar, Dr. Trung Q. Le, Dr. Tuomo von Lerber, Ali Emsia, Sujoy Paul, Peter kiesslich, Andreas Semrad, Dr. Oktay Yilmazoglu, Dr. Chong Jin, Dr. Oleg Cojocari, Ion Oprea, Dr. Cezary Sydlo, Maria Kaiser, Dr. Michael Feiginov and Traudel Micus.
Especially I would like to thank the Colleagues from institutions below involved in the European project Subtune because of the great collaborations during the project:
Dr. Petter Westbergh, Dr. Johan Gustavsson, Dr. Åsa Haglund und Prof. Anders Larsson from Chalmers University of Technology.
Christian Grasse, Tobias Gruendl and Prof. Markus-Christian Amann from Walter Schottky Institute of technical University Munich.
Dr. Pierluigi Debernardi from IEIIT-CNR in Torino.
Dr. Pierre Ferdinand from CEA List, Saclay, France.
Aidan Daly and Dr. Brian Corbett from Tyndall National Institute, Cork, Ireland
Finally i would like to thank my parents Farideh Dehdari and Hossein Abdollahzadeh Davani, My wife Lu Huo and our Son Keyan Abdollahzadeh Davani for their supports during this work and believing in me.

Erklärung laut §9 PromO

Ich versichere hiermit, dass ich die vorliegende Dissertation allein und nur unter Verwendung der angegebenen Literatur verfasst habe. Die Arbeit hat bisher noch nicht zu Prüfungszwecken gedient.

Abstract

The forecast for serial transmission speed used in data communication systems is a continued exponential increase with time. It is directly scaled in concert with silicon integrated circuits and in response to the human society's perpetual hunger for massive increases in the bandwidth. This leads to an increase in the data rate of a single transmission channel and at the same time to an efficient usage of the existing transmission medium by using methods such as wavelength devision multiplexing (WDM). The electrical interfaces for a single channel using a bit rate beyond 10 Gbit/s are being standardized for a variety of applications. As a result, the fundamental electro-magnetic limitations of copper wire-based links at a bit rate $>$10 Gbit/s make fibre-based optics for data communication indispensable for distances $>$1 m. For shorter distances, problems associated with electrical transmission lines at such high frequencies, e. g. the high power consumption, strong signal attenuation, signal distortions and the electromagnetic interferences, lead to an unstoppable and progressive penetration of the optical communication links into traditional copper interconnect markets [1]. This trend greatly expands the applications of vertical cavity surface emitting lasers (VCSELs), VCSEL arrays and tunable VCSELs as inexpensive, efficient, reliable, readily manufacturable and compact laser light sources for the next generation of fibre-optic, free-space, board-to-board, module-to-module, chip-to-chip and on-chip interconnects and related information systems and networks.

This thesis reports the development of a high-speed tunable short-wavelength VCSEL. The goal of our research is developing a device, suitable for optical interconnects.

To achieve this goal, the long tradition and experience in fabrication and development of micro-electro-mechanical system- (MEMS-) mirrors for the long wavelength VCSELs in the Institute of Microwaves and Photonics of the Technische Universität Darmstadt is combined with the long tradition and experience in design and development of high-speed non-tunable short-wavelength VCSELs at Chalmers University of Technology in Göteborg Sweden . The Walter Schottky Institute of Munich has provided wafers for semiconductor mirrors and the IEIIT-CNR in Torino has supported us with cold-cavity simulations.

The developed devices are made of a GaAs based half-VCSEL in combination with a MEMS-mirror. They exhibit a maximum amplitude modulation bandwidth of up to 5 GHz, which was the highest achieved amplitude modulation bandwidth among tunable GaAs based VCSELs at the time of publication of our results according to our knowledge. These devices are also the first developed high-speed tunable VCSELs in the short-wavelength range. They exhibit a wide single-mode continuous tuning range of up to 37 nm, which is the highest reported tuning range around 850 nm achieved by VCSELs.

Additionally to the results mentioned above, which have been achieved by means of bulk-micromachining of the MEMS-mirror, a surface-micromachining technology has been successfully developed and implemented. Additionally the polarization stability of the devices is achieved by implementing a sub-wavelength grating (SWG). Further characteristics of the devices such as linewidth, far field, tuning speed, relative intensity noise (RIN) and large signal

behavior are investigated by means of measurements.

Kurzfassung

Die Prognose für die serielle Übertragungsgeschwindigkeit in Datenkommunikationssystemen zeigt eine kontinuierliche exponentielle Steigerung mit der Zeit. Sie skaliert direkt mit der Anzahl der integrierten Halbleiterschaltungen und stellt eine Lösung für den stetig in der Gesellschaft steigenden Bandbreitenbedarf dar. Dies führt zur Steigerung der Datenrate der einzelnen Übertragungskanäle und gleichzeitig zur effizienten Nutzung der existierenden Übertragungsnetze durch den Einsatz von Methoden wie Wavelength Division Multiplexing (WDM). Die elektrischen Schnittstellen für die einzelnen Kanäle mit Datenraten über 10 Gbit/s sind für die verschiedenen Anwendungen standardisiert worden. Die grundlegenden elektromagnetischen Limitierungen der Datenverbindungen basierend auf Kupferleitungen für Datenraten über 10 Gbit/s macht die faserbasierte Optik bei Übertragungsentfernungen oberhalb eines Meters unabdingbar. Probleme verbunden mit den elektrischen Übertragungsleitungen bei hohen Frequenzen wie z.B. hohe Verlustleistung, starke Signaldämpfung, Signalverzerrung und elektromagnetische Interferenz führen zu einer nicht aufhaltbaren und stetig fortschreitenden Verdrängung der traditionellen Kupferleitungen durch optische Kommunikationssysteme [1]. Dieser Trend fördert die Anwendung von Vertical Cavity Surface Emitting Lasern (VCSELn), Matrizen aus VCSELn und abstimmbaren VCSEL als günstige, effiziente, zuverlässige, leicht herstellbare und kompakte Laserlichtquellen für die nächste Generation von Faseroptik, Freiraumoptik, Board-zu-Board, Modul-zu-Modul, Chip-zu-Chip und auf-Chip Datenübertragung.

Diese Dissertation berichtet über die Entwicklung von einem schnellen, abstimmbaren und kurzwelligen VCSEL. Das Ziel unserer Forschung war die Entwicklung eines Bauteils, das in optischen Interconnects eingesetzt werden kann. Um dieses Ziel zu erreichen ist die lange Tradition und Erfahrung des Instituts für Mikrowellentechnik und Photonik der Technischen Universität Darmstadt in der Entwicklung von Micro-Electro-Mechanical System- (MEMS-) Spiegeln für die Langwellen-VCSELs mit der langen Tradition und Erfahrung der Chalmers University of Technology in Göteborg Schweden im Entwurf und der Entwicklung von high-speed nicht abstimmbaren Kurzwellen-VCSELn zusammengeflossen. Das Walter Schottky Institut in München hat zusätzlich Wafer für die Halbleiter-Spiegel hergestellt und das IEIIT-CNR in Turin unterstützte die Arbeit mit “Cold-Cavity”-Simulationen.

Die entwickelten VCSEL bestehen aus einem GaAs-basierenden Halb-VCSEL in Kombination mit einem MEMS-Spiegel. Sie zeigen eine maximale Amplitudenmodulationsbandbreite von bis 5 GHz. Dies ist nach unserem Wissen die höchste erreichte Amplitudenmodulationsbandbreite für abstimmbare VCSEL. Diese VCSEL sind auch die ersten entwickelten schnell abstimmbaren VCSEL im Kurzwellenbereich. Sie weisen eine breite Abstimmungsbandbreite von bis zu 37 nm auf. Dies stellt die größte bekannte Abstimmungsbandbreite bei VCSELn um 850 nm dar.

Zusätzlich zu den geschilderten Ergebnissen, die mit Bulk-Micromachining erreicht worden sind, ist eine Surface-Micromachining-Technology erfolgreich entwickelt worden. Die

Stabilisierung des Polarisationszustandes des VCSELs mit Hilfe eines “ Sub-Wavelength-Gratings” ist ebenfalls demonstriert worden. Zusätzlich sind weitere Eigenschaften der VCSEL wie Linienbreite, Fernfield, Abstimmungsgeschwindigkeit, relatives Intensitätsrauschen (RIN) und Großsignalverhalten durch Messungen untersucht worden.

Contents

1. Introduction

The first detailed proposal for the construction of a laser, which at that time they called an optical maser (microwave amplification by stimulated emission of radiation), was published in the famous paper “Infrared and Optical Masers” in December 1958 [2] by Townes and Schawlow. This publication was the starting point for the race to build lasers. Meanwhile, Theodor Maiman was trying to use his knowledge of ruby masers to make a laser at Hughes Research Laboratories in Malibu, California. He succeeded in making the ruby laser work for the first time, on May 16, 1960.

In 1962, Robert Hall created the first semiconductor injection edge-emitting laser, which is used in many electronic appliances and communication systems that we use every day. Vertical cavity surface emitting lasers (VCSELs) were first pursued some years later in 1979 by Soda et al. of TIT in Japan [3] [4]. They employed a double heterostructure design with a GaInAsP active region and used metallic mirrors. The device lased at a wavelength of 1.8 μm under a pulsed operation at 77^o K with a high threshold. Advances in epitaxial technologies, in particular the development of semiconductor Bragg reflectors with extremely high reflectivities ($\approx$ 0.999) and the improvement in the control of thickness and composition of epitaxial layers, led to the first demonstration of the continuous-wave (CW), room temperature operation of a low-threshold VCSEL with a single-quantum-well active region in 1989 [5].

Due to the vertical-cavity geometry of the VCSELs, they offer a number of significant advantages compared with edge-emitting lasers [6]. Since VCSELs have a relatively small active volume, very low threshold currents are attainable. Because of the short cavity and symmetry in the structure, the laser output is in the form of a narrow, low-divergence, circular beam, permitting high coupling efficiency to optical fibers with relaxed alignment tolerances, as well as easy focusing into a tight spot for optical storage applications. Furthermore, due to the microscopic cavity length, VCSELs inherently operate in a single longitudinal mode, and are thus suitable for high-bit-rate, fibre-optic data communications. Above all, VCSELs allow a high packaging density in form of two-dimensional arrays, a cost-effective fabrication and testing on wafer level. Thus, VCSELs demonstrate the potential of being a low-cost, easily packaged, compact light source for use in high-volume applications related to optical communications, data storage and optical interconnects.

Because the optical mode is propagating along the axis of the growth direction, the length of the gain medium is as short as the thickness of the quantum wells itself. Without the benefit of a long gain medium as in edge emitters, the losses in the cavity and in particular the output coupling loss of the mirrors must be made much smaller to achieve lasing threshold. As the result, a highly reflective mirror should be used to increase the optical power in the cavity. The candidate for such a mirror in this thesis is a distributed Bragg reflector (DBR). The DBR consists of multiple layers of alternating materials. By changing the number of pairs, different reflectivities can be achieved [7].

The first tunable VCSEL with a tuning range above 10 nm is reported in 1994 by L. Fan [8]. The tuning of that device was achieved by implementing a thin-film heater on the device. With this method a tuning range of 10.1 nm around 950 nm was achieved. M. C. Larsson et.al. demonstrated a widely tunable VCSEL with a tuning range of 19.1 nm around 960 nm in 1995. The tuning principle of the VCSEL was based on a MEMS-membrane. In the short-wavelength area the highest reported tuning range around 950 nm is 44 nm achieved by P. Wang in 1999 [9]. In this work, a tuning range of 37 nm has been achieved around 850 nm.

The first high-speed (in term of the amplitude modulation) tunable VCSEL known to the author is reported in 2001 by G. S. Li et. al. in [10]. The device had a tuning range of 16 nm at 1550 nm wavelength range. A direct modulation of the device with 2.5 Gb/s was also demonstrated. The first high-speed tunable VCSEL in short-wavelength area is demonstrated by us in [11].

Depending on the transmission distance in optical communications one distinguishes between global area networking (GAN), wide area network (WAN), metropolitan area network (MAN) and local area network (LAN). Historically one speaks about telecommunication (telecom) by the longer distances, as in the case of the GAN, WAN and MAN, while it is common to use the term data communication (datacom) by shorter distances, such as within the LAN or shorter [1]. Transmission distances within the GAN can reach many thousand kilometers, e. g. in intercontinental links, while a WAN commonly connects different cities of one or several countries with typical distances of several tens to thousands of kilometers. The area of a MAN is mostly limited to the area of a city and a LAN commonly transfers data between several computers within one building or a building complex.

For longer distances the edge emitting lasers and the wavelengths around 1550 and 1310 nm are utilized. At 1550 nm standard single-mode fibers have a minimum attenuation and at 1300 nm the dispersion of those fibers is zero. For short distances datacom applications oxide-confined VCSELs, emitting around 850 nm, have established themselves as very reliable and cost-effective laser light sources [1]. Tunable high-speed short-wavelength VCSELs can be applied in datacom applications, if the wavelength division multiplex (WDM) is performed.

To bring the signal to a computer is only one important part of the information transfer process. The second, equally important part is to provide technologies for the data exchange between different components within a computer. Again, for this task one can distinguish between different levels of interconnects inside the computer depending on the transmission distance such as the cluster level (rack-to-rack 2-100 m) since 1990s, the rack level (box-to-box 1-10 m) since late 2000s, the box level (board-to-board 10-100 cm) in 2009-2010, the board level (module-to-module 5-30 mm) in 2010-2015, the module level (chip-to-chip 5-100 mm) probably after 2015 and the chip level (on-chip 0-30 mm) beyond 2015 [1] [12].

The ultimate goal for optics inside the computer is to transfer data by light at all levels, even at very short distances on-chip. As distances become shorter and the density of interconnects and the number of the transmission lines grow, the fabrication cost of a single laser starts to play an ever increasing role in the total cost. VCSELs, as very inexpensive, low power and reliable laser light sources, benefit from this trend decisively. Nowadays the oxide-confined GaAs-based VCSELs dominate the datacom market.

Additionally to the WDM applications in datacom, high-speed tunable short-wavelength VCSELs are suitable for the parallel optical interconnects with applications in the massively parallel processing systems [13]. In these applications a single array of tunable VCSELs can replace a multiple array of fixed-wavelength VCSELs. These VCSELs can also be used in the reconfigurable multiprocessor interconnects in combination with the selective optical broadcast components (SOB) as shown in Fig 1.1 [14].

This thesis demonstrates the design, the fabrication and the characterization of a novel high-speed tunable short-wavelength VCSEL. The second chapter provides the reader with the basic theory necessary to understand this thesis. The passive optical resonators, the DBR-structure, the transfer-matrix-method and the basics of active optical resonators are discussed. At the end of the second chapter, the condition for the single-mode operation and the polarization stability of the device are introduced. The third chapter introduces the structure and the design of the half-VCSEL. The half-VCSEL is basically a VCSEL without the top DBR. It includes a bottom DBR, an active region and a current aperture. The forth chapter includes the design and the fabrication of the top movable membrane and the modeling of the device via simulation. Three kinds of movable membranes, namely semiconductor, dielectric and hybrid, which are suitable for integration with the designed half-VCSEL, are developed in this work. The fifth chapter demonstrates the measurement results of the developed devices. Several different characteristics of the devices, such as power-current-voltage (PIV) characteristic, tuning range, tuning speed, linewidth, polarization, far field, relative intensity noise (RIN) and small and large amplitude modulation (AM) are investigated via measurements and the results are demonstrated. The last chapter includes the summary and outlook.

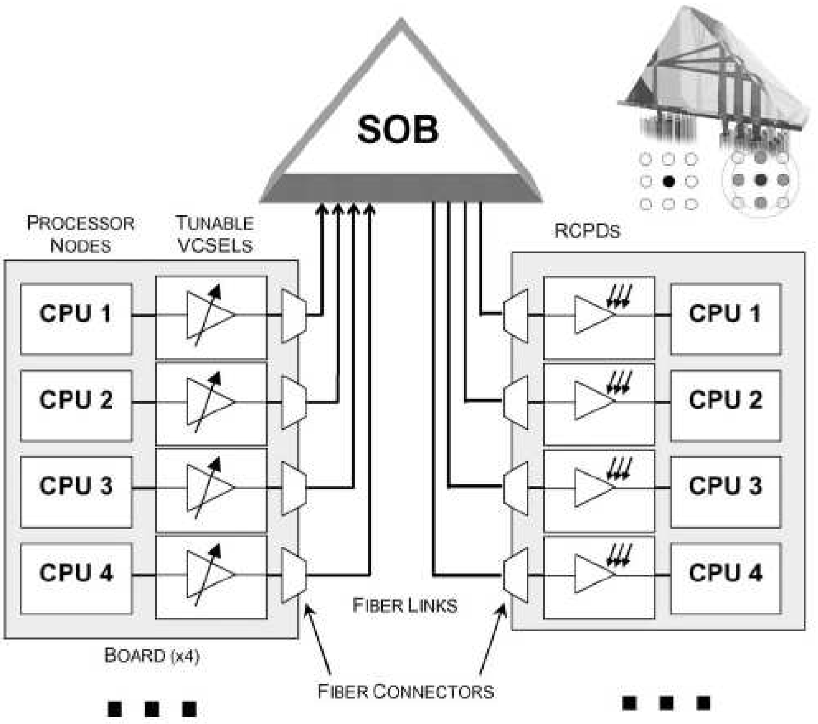

Figure 1.1.: Schematic representation of the complete reconfigurable optical interconnect with processors divided in groups of four per board. A processor node transmits data on one of nine wavelengths $\lambda 1, \ldots, \lambda 9$. The optical broadcast element distributes the signal towards nine fellow processor nodes. Since every receiving processor node is sensitive to one wavelength only, the target processor node is selected by emitting at the appropriate wavelength [14].

Acknowledgment

The content of this work is based on the work performed in the European project ”SUBTUNE” (FP7STREP) under the grant agreement number 224572. Different contributions of the project partners are announced in the work.

2. Theoretical Basics

The basic theory of optical resonators and VCSELs required to understand this work is introduced and discussed in this chapter. Firstly, the ideal optical resonators are described in a plane-plane configuration (Fabry-Pérot (FP)-resonator) and a plane-concave configuration (half-symmetric resonator). Since the resonator of the VCSEL presented in this thesis has a half symmetric structure the intensity distribution and the modal behavior of this type of resonator are investigated. Secondly, the impact of two different media inside the resonator is shown. Thirdly, the distributed Bragg reflectors (DBR), which define the mirrors of the resonator in the devices, are discussed. Fourthly, the transfer matrix method, which is a numeric method to model and to simulate the DBR and the whole VCSEL, is demonstrated. Finally, the active optical resonator by means of the rate equations is introduced. The laser properties such as small-signal amplitude modulation (AM), large-signal AM, relative intensity noise (RIN) and laser linewidth are discussed. The single-mode behavior and the polarization behavior of the VCSEL are briefly introduced as well [15] [16].

2.1. Passive Optical Resonators

Inside a laser exists an optical resonator. For a passive optical resonator, it is assumed that there is no amplification inside the resonator. Although the active medium is required to generate laser emission, the concept of the passive resonator is applicable to the investigation of the physic of laser radiation [17] [18] [19].

2.1.1. FP-Resonator

A FP-resonator is a simple resonator consisting of two plane mirrors with the field reflection factors r_1 and r_2, the field transmission factors t_1 and t_2 and an optical length of L, as is shown in Fig. 2.1(a) [20] [21] [22]. The optical length is calculated from the geometrical length L_0 according to:

$$L = nL_0, \tag{2.1}$$

with n as the refractive index of the resonator medium. The resonance condition for such a resonator is reproducing the phase of the electromagnetic field after each round trip and building a standing wave by constructive and distractive interference. This condition is fulfilled at the resonant wavelengths λ_q, which are equal to:

$$\lambda_q = \frac{2L}{q}, \tag{2.2}$$

where $q \in \mathbb{N}$ is the number of periods of the standing wave in the resonator. Fig. 2.1(a) shows a FP-resonator with $q = 3$. Eq. (2.2) shows additionally the wavelength tuning principle of such

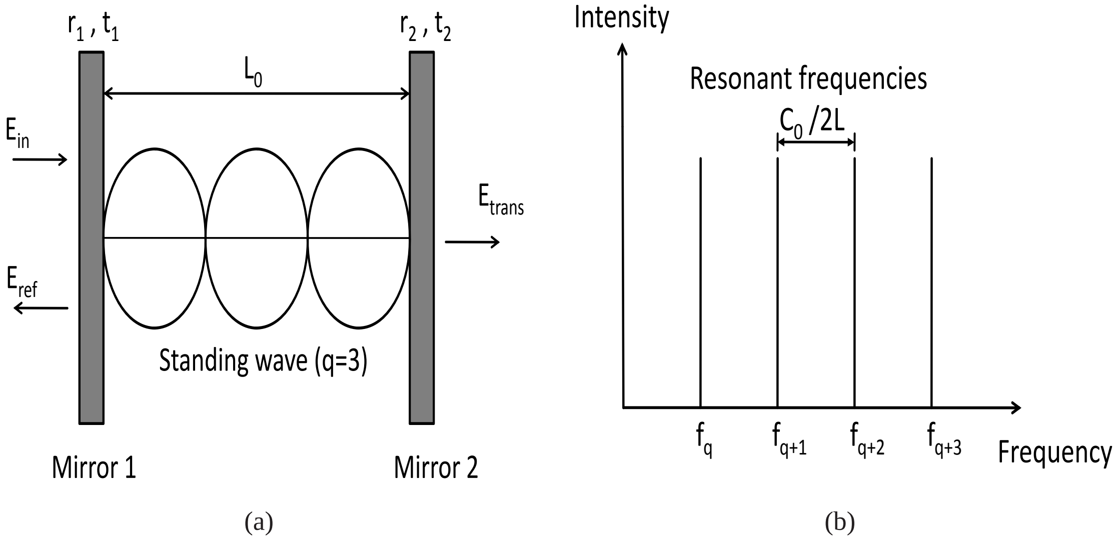

(a) (b)

Figure 2.1.: (a) FP-resonator with standing wave inside the resonator. (b) Resonant frequencies of a FP-resonator.

a resonator. By changing the optical resonator length L, achieved by changing the geometrical length L_0 or the refraction index n (Eq. 2.1), the resonant wavelength λ_q will change and the resonator can be tuned. Eq. (2.2) shows that the wavelength changes linearly with the optical resonator length:

$$\Delta\lambda = \frac{2\Delta L}{q}. \tag{2.3}$$

By replacing q in Eq. (2.2) using Eq. (2.3) the required change of the optical length to achieve a certain change in wavelength is obtained:

$$\frac{\Delta\lambda}{\lambda_q} = \frac{\Delta L}{L}. \tag{2.4}$$

The resonator has a series of equidistance resonant frequencies (corresponding to axial or longitudinal modes) given by $f_q = c_0/\lambda_q$. The frequency distance of the axial modes Δf_{FSR} is called the free spectral range (FSR) and is given by:

$$\Delta f_{\mathrm{FSR}} = \frac{c_0}{\lambda_{q+1}} - \frac{c_0}{\lambda_q} = \frac{c_0}{2L}. \tag{2.5}$$

c_0 is the speed of light in vacuum. Fig. 2.1(b) shows four resonant frequencies of the resonator. From Eq. (2.2) the resonator's longitudinal mode distance expressed in the wavelength $|\Delta\lambda_{\mathrm{FSR}}| = |\lambda_{q+1} - \lambda_q|$ can be derived as:

$$|\Delta\lambda_{\mathrm{FSR}}| = \frac{\lambda_q^2}{2L + \lambda_q}. \tag{2.6}$$

For the resonators with the long resonator length, $2L + \lambda_q$ can be approximated by $2L$. This approximation is not valid for the VCSELs due to the short resonator length.

In an ideal FP-resonator, where the losses can be neglected, the power reflection factor R and the power transmission factor T are given by [20]:

$$\begin{aligned} R &= \frac{\left|\mathrm{E}_{\mathrm{ref}}^2\right|}{\left|\mathrm{E}_{\mathrm{in}}^2\right|} = \frac{(\sqrt{R_1}-\sqrt{R_2})^2 + 4\sqrt{R_1R_2}\sin^2(kL)}{(1-\sqrt{R_1R_2})^2 + 4\sqrt{R_1R_2}\sin^2(kL)}, &(2.7)\\ T &= \frac{\left|\mathrm{E}_{\mathrm{trans}}^2\right|}{\left|\mathrm{E}_{\mathrm{in}}^2\right|} = \frac{T_1T_2}{(1-\sqrt{R_1R_2})^2 + 4\sqrt{R_1R_2}\sin^2(kL)}. &(2.8)\end{aligned}$$

$R_{1,2} = |r_{1,2}|^2$, $T_{1,2} = |t_{1,2}|^2$ and $k = 2\pi/\lambda$ is the wave number. E_{in} is the incoming optical field into the resonator, $\mathrm{E}_{\mathrm{ref}}$ is the reflected field and $\mathrm{E}_{\mathrm{trans}}$ is the transmitted field through the resonator (Fig. 2.1(a)). The bandwidth of the resonator defined by the full-width half-maximum (FWHM) in frequency domain Δf_{FWHM} and in wavelength domain $\Delta\lambda_{\mathrm{FWHM}}$ is approximated by:

$$\begin{aligned} \Delta f_{\mathrm{FWHM}} &= \frac{(1-\sqrt{R_1R_2})c_0}{2\pi L\sqrt{\sqrt{R_1R_2}}} \approx (1-\sqrt{R_1R_2})\frac{c_0}{2\pi L}, &(2.9)\\ \Delta\lambda_{\mathrm{FWHM}} &\approx \frac{(1-\sqrt{R_1R_2})\lambda_0^2}{2\pi L\sqrt{\sqrt{R_1R_2}}} \approx \frac{(1-\sqrt{R_1R_2})\lambda_0^2}{2\pi L}. &(2.10)\end{aligned}$$

In the equations above a high reflectivity ($R_{1,2} \approx 1$) is assumed. With this assumptions $(1-\sqrt{R_1R_2})/\sqrt{\sqrt{R_1R_2}} \approx (1-\sqrt{R_1R_2})$ is approximated. By comparing Eqs. (2.6) and Eq. (2.10), $\Delta\lambda_{\mathrm{FSR}}$ and $\Delta\lambda_{\mathrm{FWHM}}$ are inversely proportional to the optical length L and $\Delta\lambda_{\mathrm{FWHM}}$ increases with the decrease of $R_{1,2}$.

Fig. 2.2 shows the transmission characteristic of a FP-resonator according to Eq. (2.8) as a function of the wavelength for an optical resonator length of $L = 5.95$ μm, mirror reflectivity of $R_1 = R_2 = 90\%$ and transmission factors of $T_1 = T_2 = 10\%$. With these parameters a FSR of 56.68 nm and a FWHM of 1.22 nm are achieved. The two plotted longitudinal modes in Fig. 2.2 have their maximum transmission at the wavelength of $\lambda_{15} = 793.33$ nm and $\lambda_{14} = 850$ nm.

2.1.2. Plane-Concave Resonator

Some basic properties of a stable resonator with the spherical mirrors are explained in this section. The presence of an active medium inside the resonator is neglected. A resonator in general is made of two mirrors with the radius of curvature (RoC) of ρ_1 and ρ_2 in a distance of L_0. For the plane-concave resonator the first mirror has no curvature ($\rho_1 \to \infty$) and can be considered as a plane mirror as is shown in Fig. 2.3. The g-parameters for resonator mirrors are defined as [20] [23]:

$$g_i = 1 - \frac{L}{\rho_i} \quad , \; i = 1, 2. \tag{2.11}$$

The g-parameters are the stability parameters for the resonator. For a stable resonator the following condition must hold: $0 \leq g_1g_2 \leq 1$. For the plane-concave resonator holds $g_1 = 1$. From now on only the plane-concave resonator is considered. The condition for the stability of this kind of resonator is given by:

$$0 < g_2 < 1. \tag{2.12}$$

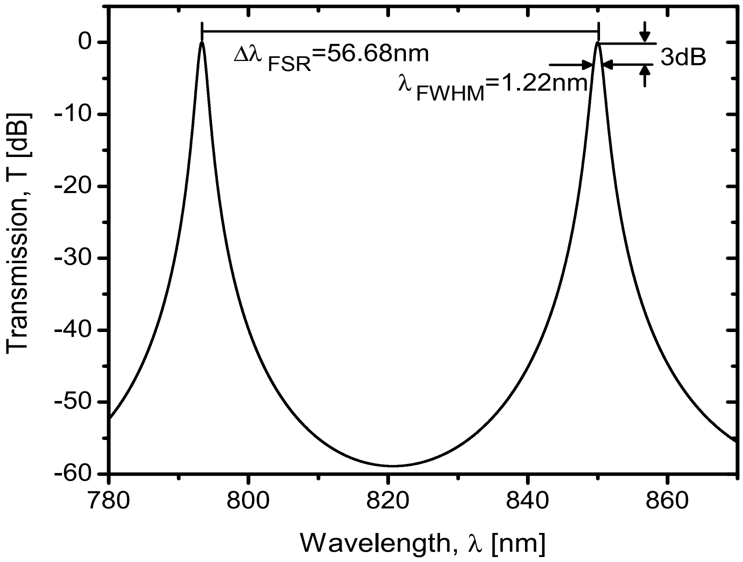

Figure 2.2.: Transmission characteristic of a FP-resonator with $L = 5.95\mu m$, $R_1 = R_2 = 90\%$ and $T_1 = T_2 = 10\%$.

To achieve the stability condition from Eq. (2.12) the RoC of the concave mirror should be larger than the optical length ($\rho_2 > L$). The field distribution that represents the steady-state solutions of the stable resonator will reproduce itself after each round trip. The round trip in the resonator is described mathematically by the Kirchhoff integral equation. The solution of this integral equation represents the eigenmodes of the optical resonator. In general an infinite number of the eigenmodes exists. Which of these eigenmodes will actually be observed in the resonator depends on the geometry and the size of the mirrors. In reality, the mirrors will have a finite size with a shape that usually is round or rectangular. This boundary condition is taken into account by choosing those eigensolutions that exhibit circular or rectangular symmetry, respectively (The VCSEL structure in this work has a circular symmetry). The eigenmodes are characterized by the transverse mode structure (transverse mode index $p, l \in \mathbb{N}$) with the notation TEM_{pl}. The abbreviation TEM represents the fact that the electric and the magnetic field vectors are perpendicular to each other and to the wave vector $\mathbf{k}$.

In the following, it is assumed that the reflectivities of both resonator mirrors exhibit 100% ($R_1 = R_2 = 1$). Since the mirrors are not limited by an aperture and consequently no power can leak out of the resonator, the resonator will face no losses. Since the shape of the resonator (VCSEL) used in this work is circular, only the eigenmode results for the circular symmetry resonators are discussed here. These eigenmodes are called Gauss-Laguerre modes. Their field distribution is Gaussian and is determined on the plane mirror ($z = 0$ in Fig. 2.3) as follows:

$$E_{pl}(r,\Phi) = E_0 e^{-\frac{r^2}{w_0^2}} \left(\frac{\sqrt{2}r}{w_0}\right)^l \left[L_p^{(l)}\left(\frac{2r^2}{w_0^2}\right)\right] e^{jl\Phi}. \tag{2.13}$$

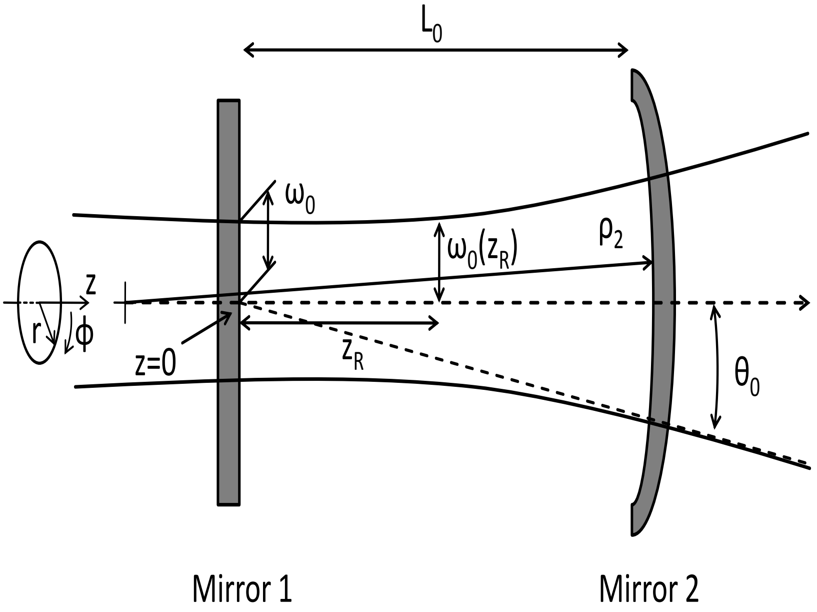

Figure 2.3.: Plane-concave resonator. The change in the beam waist of the first-order Gaussian beam (TEM_{00}) with distance from the plane mirror ($w_0(z)$) is indicated inside the resonator.

$L_p^{(l)}$ is the Laguerre polynomial of order p, l. For low orders $p = 0, 1$ and 2 they read:

$$\begin{aligned} L_0^{(l)}(t) &= 1, \\ L_1^{(l)}(t) &= l + 1 - t, \\ L_2^{(l)}(t) &= 0.5(l+1)(l+2) - (l+2)t + 0.5t^2, \end{aligned} \tag{2.14}$$

where r and Φ present the radial and azimuthal coordinates (Fig. 2.3). w_0 is the beam radius (called as the beam waist) of the TEM_{00} mode (called as the fundamental mode) on the plane mirror and depends on the optical length of the resonator and RoC of the concaved mirror. It can be expressed as:

$$w_0^2 = \frac{\lambda_0}{\pi}\sqrt{L(\rho_2 - L)}. \tag{2.15}$$

At the radial distance of $r = w_o$ (Fig. 2.3) from the optical axis the intensity of the field decreases by the factor of $1/e^2$ and 86.5% of the beam power is contained within the corresponding circle. The intensity distribution $I_{pl}(r)$ of the eigenmodes is derived from the field distribution (Eq. 2.13) on the plane mirror:

$$I_{pl}(r) = |E_{pl}(r,\Phi)|^2 = E_0^2 e^{-\frac{2r^2}{w_0^2}} \left(\frac{\sqrt{2}r}{w_0}\right)^{2l} \left[L_p^{(l)}\left(\frac{2r^2}{w_0^2}\right)\right]^2. \tag{2.16}$$

p and l corespondent to the number of maximums and minimums of $I_{pl}(r)$ in the radial and azimuthal directions respectively. Fig. 2.4 shows the nominal ($E_0 = 1$) intensity distribution for TEM_{00}, TEM_{01} and TEM_{10} modes on the plane mirror for a plane-concave resonator similar to our VCSEL structure (Fig. 2.3) with $L = 6$ μm and $\rho_2 = 5$ mm. The figure shows

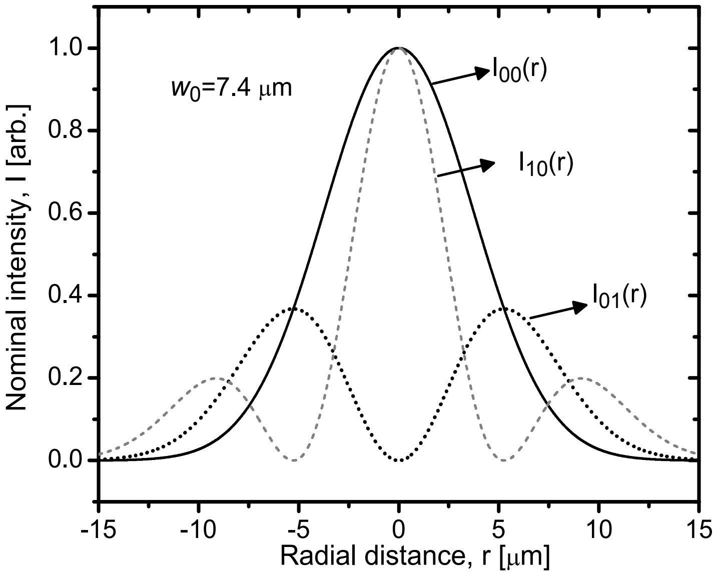

Figure 2.4.: Intensity distribution of TEM_{00}, TEM_{01} and TEM_{10} modes on the plane mirror for a plane-concave resonator.

how the intensity distribution for different modes changes with the radial distance from the optical axis. For the given parameter a beam waist of $w_0 = 7.44$ μm has been calculated with Eq. (2.15). By moving from the plane mirror along the z-axis (Fig. 2.3) toward the second mirror, the beam waist of the fundamental mode changes according to:

$$w_0(z) = w_0\sqrt{1 + (z/z_R)^2}, \tag{2.17}$$

where z_R is the Rayleigh range given by:

$$z_R = \frac{\pi w_0^2}{\lambda_0}. \tag{2.18}$$

At a distance from the plane mirror equal to z_R, the beam width is $w_0(z_R) = \sqrt{2}w_0$. The characteristic of $w_0(z)$ approaches a straight line for $z \gg z_R$ (Fig. 2.3). The angle between this straight line and the axis of the beam is called divergence angle θ_0:

$$\theta_0 \approx \frac{\lambda_0}{\pi w_0} = \frac{w_0}{z_R}. \tag{2.19}$$

The total angular spreed of the beam is then $\Theta = 2\theta_0$.
For a certain axial mode number q (Sec. 2.1.1) the frequency separation of the transverse modes (TEM_{pl}) is given by [20]:

$$f_{plq} = \frac{c_0}{2L}\left(q + \frac{2p + l + 1}{\pi}\arccos\sqrt{g_2}\right). \tag{2.20}$$

Fig. 2.5 shows a plane-concave resonator with two different mediums with different refractive indices n_1 and n_2 inside the resonator. For this resonator the beam waist can be obtained by:[1]

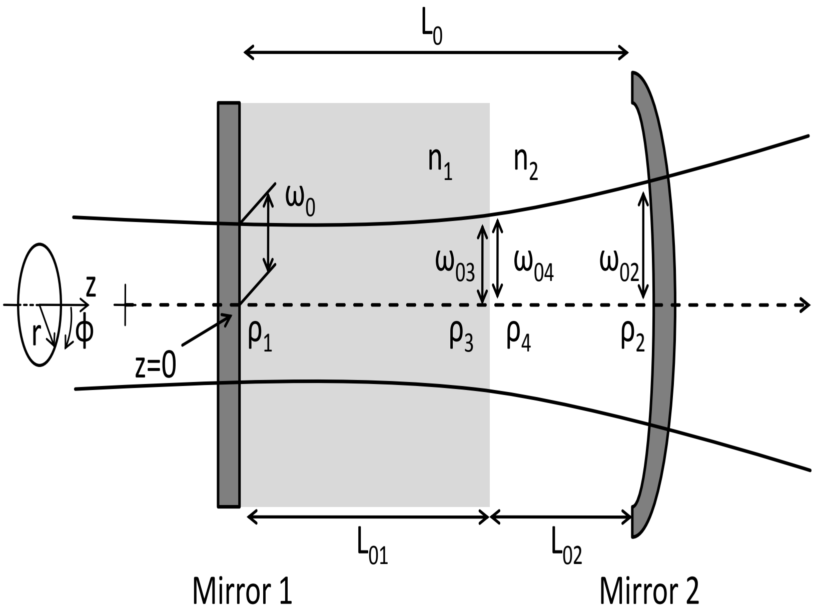

Figure 2.5.: plane-concave resonator with two different mediums with different refractive indices inside the resonator.

$$w_0 = \sqrt{\frac{\lambda_0}{\pi n_2}\sqrt{M(\rho_2 - M)}} \;\; ; \;\; M = \frac{n_2}{n_1} L_{01} + L_{02}, \tag{2.21}$$

where L_{01} and L_{02} are the geometrical length of the two mediums. The derivation of Eq. (2.21) is done in App. A.

---

[1] A loss free homogeneous medium and mirror reflectivity of 100% are assumed.

2.2. Distributed Bragg Reflector

A distributed Bragg reflector (DBR) is a high reflective mirror made of several pairs of layers with alternating materials. The complex refractive index $\underline{n}$ of a material is defined as:

$$\underline{n} = n + jn^{''}. \tag{2.22}$$

n is the real part of $\underline{n}$ and $n^{''}$ is the imaginary part. For simplicity we assume materials with real refractive indices in this explanation. Each pair of the DBR consists of two layers with a high n_H and a low n_L refractive index, respectively. Fig. 2.6 shows a DBR with 1.5 pairs (3 layers). The idea of using DBRs is to obtain the constructive interference of the reflected light from the different layers and thus to achieve a high reflectivity from the mirror. To achieve the constructive interference, the geometrical length of each layer should be:

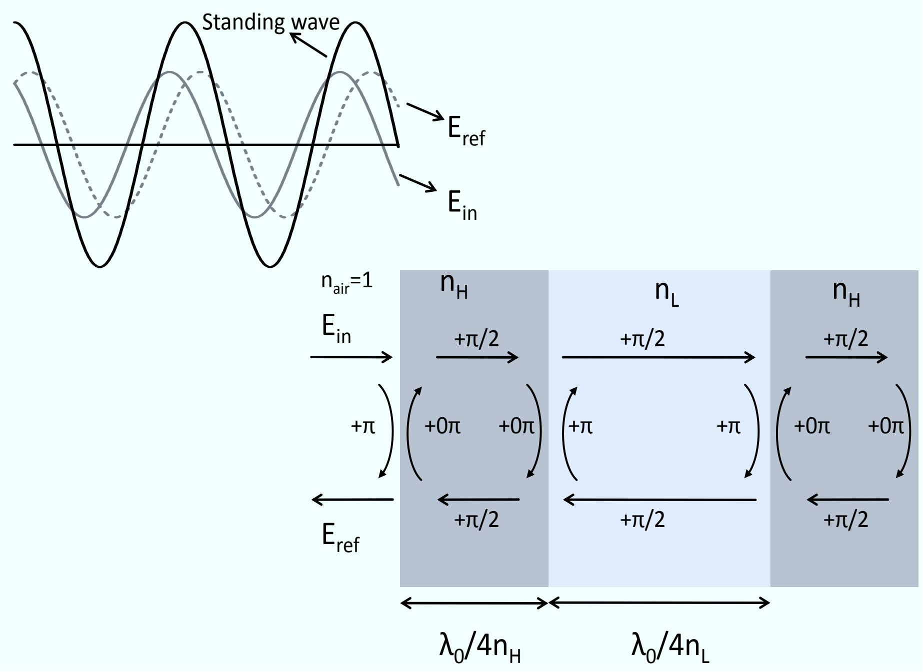

Figure 2.6.: DBR with 3 layers and the resulting standing wave generated from the combination of incident and reflected field on DBR at the time $t = t_0$.The phase shifts of the reflected and the transmitted fields are indicated in the Figure.

$$L_{H,L} = (2m-1)\frac{\lambda_0}{4n_{H,L}} \quad ; \quad m \in \mathbb{N}. \tag{2.23}$$

Fig. 2.6 demonstrates the propagation of the field in a DBR with three layers. By the incidence of field E_{in} on the high reflective layer of the first pair, a portion of the field will reflect with a phase shift of $\varphi = \pi$. This phase shift is due to the penetration of the field from a material with a low refractive index (air) to a material with a higher refractive index. The part of the field, which is not reflected, enters the first layer. The reflectivity of the field r from one material to another material with the complex refractive indices n_1 and n_2 respectively is given by:

$$r = \frac{n_1 - n_2}{n_1 + n_2}, \tag{2.24}$$

where the power reflectivity is:

$$R = |r|^2 = \left|\frac{n_1 - n_2}{n_1 + n_2}\right|^2 . \tag{2.25}$$

The field then travels through the first layer. At the interface to the second layer the field has already experienced a phase shift of $\phi = \pi/2$ because of the $\lambda/4$ optical length of the layer. At the second interface, again, a part of the field is reflected and another part passes through. This reflected field, due to the reflection from a material with higher refractive index, will not experience any additional phase shift. After traveling back to the first layer-air interface and experiencing another $\phi = \pi/2$ phase shift, it adds to the first reflected field in phase. This process is repeated in each layer. The maximum reflectivity of the DBR for the central wavelength of λ_0, in the case of a loss free DBR in the air, is given by [20] [24]:

$$R_{\text{DBR}} = \left(\frac{1 - \left(\frac{n_L}{n_H}\right)^{2M}}{1 + \left(\frac{n_L}{n_H}\right)^{2M}}\right)^2 , \tag{2.26}$$

where M is the number of pairs of the DBR. Eq. (2.26) shows that by increasing the number of pairs and decreasing the ratio n_L/n_H, the maximum reflectivity of DBR R_{DBR} increases.
The delay of the reflected field in a distributed reflector is most commonly associated with an apparent depth of penetration L_{eff} into the mirror given by [25] [26]:

$$L_{\text{eff}} = \frac{\lambda_0}{4\Delta n}.\tanh\left(\frac{n_H^2 - n_L^2}{2n_H n_L}.M\right) \approx \frac{\lambda_0}{4\Delta n}. \tag{2.27}$$

In short resonators like VCSELs, the penetration depth should be taken into account for calculating the whole resonator length. The total resonator length is then given by:

$$L_{0(\text{res})} = L_0 + L_{\text{eff}}^1 + L_{\text{eff}}^2. \tag{2.28}$$

L_{eff}^1 and L_{eff}^2 are the penetration depth in the first and the second DBRs. As is demonstrated in Fig. 2.6 the interference of E_{in} and the reflected field from the whole DBR E_{ref} results in a standing wave. The example in the figure is done for $R_{\text{DBR}} = 1$ and a loss free DBR.

Transfer-matrix method

The transfer-matrix method is an important instrument to calculate the phase and the amplitude of the reflection- and the transmission-factors in the multilayer structures like DBR or even in the whole VCSEL. It is a one dimensional method and assumes that the layers in lateral direction are infinite. Additionally it is also valid for the plane waves in the multilayer structures. The transfer matrix method can be applied to the layers with real or complex refractive indices, therefore it can include the material losses of the passive layers and the gain of the active layers. Fig. 2.7 shows the model of a multi layer structure made of M (M $\in \mathbb{N}$) homogeneous single layers. The electrical field (E_i) inside each layer results from the interference between in $(+z)$-

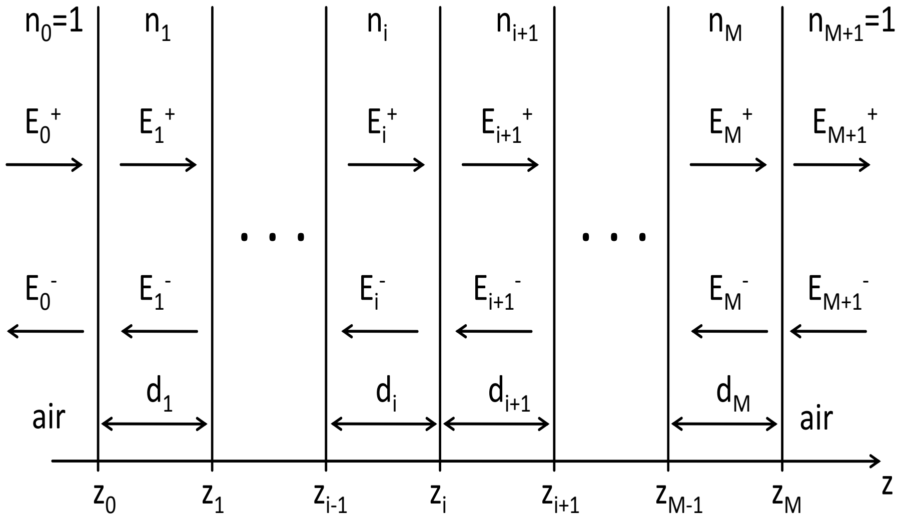

Figure 2.7.: One dimensional wave propagation in a multi layer structure. The electrical field in each layer is the superposition of the incident and reflected wave in that layer.

direction and in $(-z)$-direction propagating plane waves with the amplitudes E_i^+ and E_i^- given by:

$$E_i = E_i^+ e^{jk_i(z-z_i)} + E_i^- e^{-jk_i(z-z_i)}, \tag{2.29}$$

with

$$k_i = \frac{2\pi}{\lambda}(\underline{n_i}), \tag{2.30}$$

as the complex propagation constant. By using the continuity of the tangential components of the electrical field E and the magnetic field H on each border between the layers and the relation between the electrical field and the magnetic field given by Maxwell's equations, the field amplitude from each layer can be determined from the previous layers by [20]:

$$\begin{pmatrix} E_i^+ \\ E_i^- \end{pmatrix} = M_i \begin{pmatrix} E_{i+1}^+ \\ E_{i+1}^- \end{pmatrix}, \tag{2.31}$$

where M_i is the transfer matrix of the i-th layer:

$$M_i = \begin{pmatrix} \frac{e^{-jk_id_i}}{2} + \frac{n_{i+1}e^{-jk_id_i}}{2n_i} & \frac{e^{-jk_id_i}}{2} - \frac{n_{i+1}e^{-jk_id_i}}{2n_i} \\ \frac{e^{jk_id_i}}{2} - \frac{n_{i+1}e^{jk_id_i}}{2n_i} & \frac{e^{jk_id_i}}{2} + \frac{n_{i+1}e^{jk_id_i}}{2n_i} \end{pmatrix}. \tag{2.32}$$

By cascading the transfer matrices of the neighbor layers, the incoming field and the outcoming field of the structure can be related as:

$$\begin{pmatrix} E_0^+ \\ E_0^- \end{pmatrix} = \prod_{i=0}^{M} M_i \begin{pmatrix} E_{i+1}^+ \\ E_{i+1}^- \end{pmatrix} = \begin{pmatrix} m_{11} & m_{12} \\ m_{21} & m_{22} \end{pmatrix} \begin{pmatrix} E_{M+1}^+ \\ E_{M+1}^- \end{pmatrix}, \tag{2.33}$$

with the assumption that $E^-_{M+1} = 0$.[2] From Eq. 2.33 the power reflection coefficient R and the power transmission coefficient T are defined as:

$$R = \left|\frac{E_0^-}{E_0^+}\right|^2 = \left|\frac{m_{21}}{m_{11}}\right|^2 \quad ; \quad T = \left|\frac{E^+_{M+1}}{E_0^+}\right|^2 = \left|\frac{1}{m_{11}}\right|^2 . \tag{2.34}$$

Fig. 2.8 shows the simulated power reflection factor R and the phase of the reflection factor ($\angle r$) versus wavelength of a DBR with 12 pairs of dielectric layers (SiO_2 and Si_3N_4) with the refractive indices of $n_H = 1.96$ and $n_L = 1.46$ respectively. The layers have been assumed to have no loss and the center wavelength of the DBR is 850 nm. The maximum reflectivity achieved by this number of pairs (which depends on the ratio of the refractive indices) at center wavelength is 99.6%. The figure shows additionally how the phase and the amplitude of the power reflection change if the wavelength of the incoming wave differs from the designed wavelength. This knowledge is important for designing the tunable VCSELs and will be discussed later.

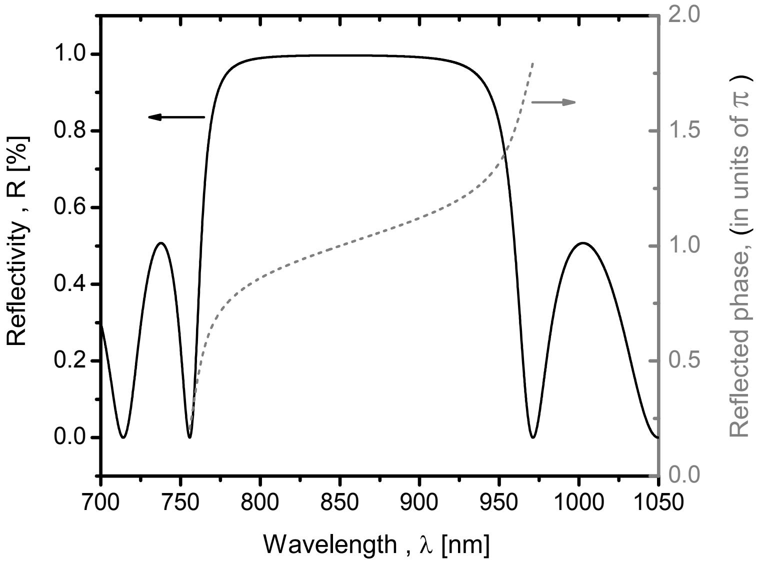

Figure 2.8.: Simulated power reflection factor (with amplitude and phase for different wavelength) with transfer-matrix method for a DBR with 12 pairs.

---

[2] It has been assumed that there is only an incoming field on one side.

2.3. Active Optical Resonators

The influence of the active medium on the properties of the resonator properties was so far neglected and the stationary field distribution inside the empty resonator was calculated. It is assumed that the losses of the resonator are compensated by an active medium. The active medium affects the electromagnetic wave oscillating inside the resonator in different ways. With every transit through the medium the intensity of the light is amplified by a gain factor. Furthermore, the refractive index and the geometry of the medium change the propagation characteristics of the beam. As a result the resonator parameters (g-parameters, optical length) depend on the dimensions and the material properties of the medium [21].

2.3.1. Laser Condition

In following the theory of a semiconductor FP-VCSEL is discussed. As is shown in Fig. 2.9 the VCSEL consists of two high reflective mirrors (DBRs) and an active medium to compensate the losses. The influence of the gain of the quantum wells is considered by the introduction of a confinement factor. Additionally, it is assumed that the real part of the refractive index inside the cavity is approximately constant. Starting from Maxwell's equations a wave equation (sometimes referred as Helmholtz equation), which is very analogous to Schrödinger's equation, can be derived as [28]:

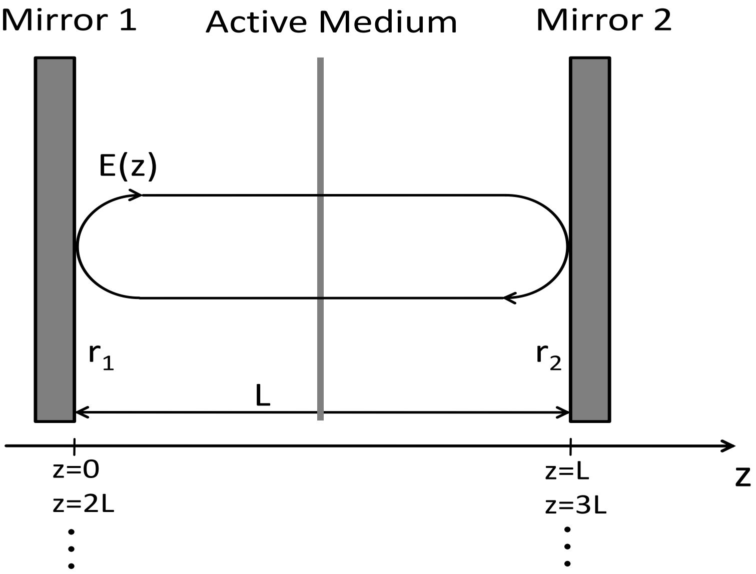

Figure 2.9.: FP-laser with active medium inside the resonator.

$$\nabla^2 \vec{E} = \mu\epsilon \frac{\partial^2 \vec{E}}{\partial t^2}, \tag{2.35}$$

where ϵ is the dielectric constant and μ is the magnetic permeability. The time-harmonic space-varying electric field propagating in z-direction as the solution of Eq. (2.35) can be written in a simple form as:

$$E(z) = E_0 e^{-j\beta z + \frac{1}{2}(\Gamma g - \alpha_i)z}. \tag{2.36}$$

$\beta = 2\pi n/\lambda$ in Eq. 2.36 is the real propagation constant and g is the transverse modal gain factor from the active medium. Γ is the confinement factor modeling the fact that there is only gain in the active region. α_i is the internal modal loss. In order for a mode of the laser to reach threshold, the gain in the active section g must be increased to the point g_{th}, where all the propagation and mirror losses are compensated, so that the electric field exactly replicates itself after one round-trip in the cavity. Equivalently we can unravel the round-trip to lie along the z-axis and require that $E(z = 2L) = E(z = 0)$, provided we insert the mode reflection coefficients r_1 and r_2 at $z = 0$ and $z = L$ (Fig. 2.9). As a consequence of inserting these boundaries into Eq. (2.36), the laser condition can be obtained:

$$r_1 r_2 e^{-2j\beta_{th}L + (\Gamma g_{th} - \alpha_i)L} = 1. \tag{2.37}$$

The subscript $_{th}$ denotes that this characteristic equation defines the values of β and g at threshold and above. The amplitude condition of Eq. 2.37 is:

$$r_1 r_2 e^{(\Gamma g_{th} - \alpha_i)L} = 1. \tag{2.38}$$

Here g_{th} is the threshold gain and is given by:

$$g_{th} = \frac{1}{\Gamma}\left(\alpha_i + \frac{1}{L}\ln\left(\frac{1}{r_1 r_2}\right)\right), \tag{2.39}$$

where L is the optical resonator length. Γ is defined as [27]:

$$\Gamma = \frac{\int_{active} E^2(z)dz}{\int_{Res} E^2(z)dz}, \tag{2.40}$$

where the numerator is the integral over the square of the field in active medium and the denominator is the integral over the whole resonator. In fact, for active regions with a very small thickness ($L_a << \lambda$), such as in many VCSELs, the confinement factor may be as large as:

$$\Gamma \approx \frac{2L_a}{L}, \tag{2.41}$$

if the active segment is placed at the peak of the standing wave inside the resonator [7]. By introducing of α_m as the mirror loss term given by [28]:

$$\alpha_m = \frac{1}{L}\ln\left(\frac{1}{r_1 r_2}\right), \tag{2.42}$$

the photon decay rate τ_p can be obtained from:

$$\frac{1}{\tau_p} = \frac{1}{\tau_i} + \frac{1}{\tau_m} = v_g(\alpha_i + \alpha_m), \tag{2.43}$$

where $v_g = c_0/n$ is the group velocity. The phase condition of Eq. 2.37 is:

$$e^{-2j\beta_{th}L} = 1, \tag{2.44}$$

which requires:

$$\beta_{th}L = m\pi, \tag{2.45}$$

and determines the condition of the modal wavelength λ_{th}:

$$\lambda_{th} = \frac{2}{m}nL, \tag{2.46}$$

where m is the longitudinal mode number.

2.3.2. Rate Equations

The applications of VCSELs in data transmission systems rely on the dynamic and noise properties of the source. These characteristics are generally obtained from the rate equations describing the interaction of the electrons and photons in the laser cavity [29] [30] [31]. The dynamic behavior is most easily inferred from the small-signal current modulation transfer function. Noise originates from the spontaneous emission, whose statistic nature is expressed in the rate equations by Langevin forces for carriers $F_N(t)$ and photons $F_P(t)$. The amplitude noise is quantified by the relative intensity noise spectrum and the phase noise is visible as a finite laser linewidth [31]. The well-accepted laser rate equations characterize the carrier and the photon reservoirs in terms of time derivatives d/dt for a single mode laser as [31]:

$$\frac{dN}{dt} = \frac{\eta_i I}{qL_a} - \frac{N}{\tau_{sp}(N)} - \Gamma_r g(N, N_p) N_p v_g + F_N(t), \tag{2.47}$$

$$\frac{dN_p}{dt} = \Gamma \beta_{sp} \frac{N}{\tau_{sp,r}(N)} + \Gamma \Gamma_r g(N, N_p) N_p v_g - \frac{N_p}{\tau_p} + F_P(t), \tag{2.48}$$

where N is the carrier (electron or hole) density and N_p is the photon density of the laser mode. In regular VCSELs without extended cavity, only transverse modes with identical longitudinal mode order can oscillate. The mode volume $V_p = V_a/\Gamma$ is the effective volume occupied by the lasing mode or the photon volume.

η_i is the current injection efficiency accounting for the lateral leakage currents and carrier overflow over the confining barriers. In the well-designed VCSELs with high-quality active regions, $\eta_i > 95\%$ can be achieved. I is the total injected current. $\tau_{sp}(N)$ is the spontaneous recombination lifetime depends on the carrier density given by [31]:

$$\frac{1}{\tau_{sp}(N)} = \frac{1}{\tau_{sp,r}(N)} + \frac{1}{\tau_{sp,n}(N)}, \tag{2.49}$$

where $\tau_{sp,r}(N)$ is the radiative spontaneous lifetime and $\tau_{sp,n}(N)$ is the non radiative spontaneous recombination lifetime. Γ_r is the relative confinement factor given by $\Gamma_r = L\Gamma/L_a$ and β_{sp} is the spontaneous emission factor. The gain is aproximated by:

$$g(N, N_p) = \frac{g(N)}{1 + \epsilon N_p}. \tag{2.50}$$

The parameter ϵ quantifies the gain compression caused by spectral hole burning or carrier heating. In a more detailed rate equation model [32], the transport effects are considered by assuming the current injection into the barrier layers surrounding the QWs and by distinguishing between carrier reservoirs in the active QW region and in the adjacent barriers. The carrier exchange is then governed by the supply- and the escape-time constants. It is found out experimentally that the transport effects do not limit the VCSEL modulation speed up to frequencies of at least 20 GHz. In addition to carrier transport in the inner cavity region, the rate equations Eqs. (2.47) and (2.48) neglect spatial hole-burning effects and the associated lateral carrier diffusion, as well as the fact that many parameters depend on temperature.

2.3.3. Small-Signal Amplitude Modulation

The small-signal amplitude modulation frequency, the relaxation resonance frequency and the relation between the relaxation resonance frequency of a laser and its modulation bandwidth are discussed here. From the rate equations we can infer the dynamic response of the VCSEL to a harmonic current variation $\Delta I(t)$ at an operating point $I_0 \gg |\Delta I(t)|$. The equations are first of all linearized with respect to the resulting variations $\Delta N(t)$ and $\Delta N_p(t)$ (which are small compared to carrier density N_0 and photon density N_{p_0} at I_0, respectively). After that, they are Fourier transformed into quantities $\Delta\tilde{I}(f)$, etc., to obtain the spectral fluctuations as a function of the modulation frequency f. The carrier-dependent part of the gain coefficient g is also linearized and the Langevin forces F_N, F_P are both set to zero since the noise is not of interest here. Neglecting the spontaneous emission contribution in Eq. (2.47) owing to the small magnitude of β_{sp}, the resulting modulation transfer function that relates the photon density fluctuations to the modulating current is finally obtained as [31]:

$$H_{AM}(f) = \frac{\Delta\tilde{N}_p(f)}{\Delta\tilde{I}(f)/q} = \frac{Af_r^2}{f_r^2 - f^2 + j\frac{f}{2\pi}\gamma}, \tag{2.51}$$

with the magnitude square of:

$$|H_{AM}(f)|^2 = \frac{A^2 f_r^4}{(f_r^2 - f^2)^2 + (\frac{f}{2\pi})^2(\gamma)^2}, \tag{2.52}$$

where A is the amplitude factor given by [31]:

$$A = \frac{aN_p\Gamma\Gamma_r\tau_p v_g\eta_i}{(1+\epsilon N_p)}. \tag{2.53}$$

f_r is the resonance frequency given by [28]:

$$f_r \approx \frac{1}{2\pi}\frac{v_g a N_p}{\tau_p}\Gamma_r, \tag{2.54}$$

with a as the gain slope. γ is the damping rate and by using the simplified definition of f_r in Eq. (2.54) it can be obtained as [31]:

$$\gamma = Kf_r^2 + \gamma_0, \tag{2.55}$$

Here, the so-called K-factor and damping factor offset γ_0 are given by:

$$K = 4\pi^2\left(\tau_p + \frac{\epsilon}{v_g\Gamma_r a}\right) \quad ; \quad \gamma_0 = \frac{\partial}{\partial N}\frac{N}{\tau_{sp}(N)}. \tag{2.56}$$

For large resonance frequencies, the K-factor describes the damping of the response and is an important parameter in the characterization of high-speed lasers. The damping factor offset γ_0 is important at low powers, where the relaxation resonance frequency is small. In practice, K and γ_0 are used as the fitting parameters to be extracted from the laser modulation response [28].
Fig. 2.10 shows the transfer function of the intensity modulation for a resonance frequency

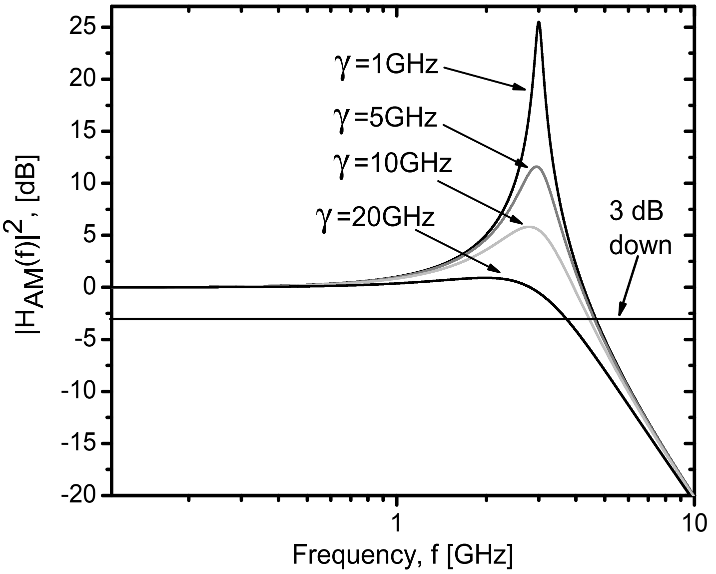

Figure 2.10.: Small signal intensity modulation of an ideal laser for a resonance frequency of 3 GHz and different damping rates.

of $f_r = 3$ GHz and different damping rates. 3-dB modulation bandwidth f_{3dB} of the laser is defined as the modulation frequency, at which the intensity of the small-signal transfer function drops to the half of its value (Fig. 2.10). The effect of damping rate on the amplitude of the resonance frequency is illustrated in Fig. 2.10. By increasing the damping rate, the resonance amplitude decreases and thus the modulation bandwidth for a fixed resonance frequency as well. Fig. 2.11 shows the modulation response for different resonance frequencies according to Eq. (2.52). The damping rate is calculated using Eq. (2.55) and the constant values of $\gamma_0 = 1\text{GHz}$ and $K = 0.5$ ns are chosen. The choice of these parameters is made in a way that it simulates the real condition of the laser. Depending on the output power or the current through the laser - here the first or second term of Eq. 2.55 is significant - the resonance is more damped at low and high output powers for a given resonance frequencies. The intensity modulation can follow the current modulation up to frequencies close to f_r. Beyond the resonance, the response drops off dramatically with $40\text{dB}/\text{decade}$. The actual peak frequency of the resonance f_p is slightly less than f_r depending on the damping and is given by [28]:

$$f_p^2 = f_r^2 \left[1 - \frac{1}{2} \left(\frac{\gamma}{2\pi f_r} \right)^2 \right]. \tag{2.57}$$

f_{3dB} is slightly higher than f_r for small damping and is given by [28]:

$$f_{3dB}^2 = f_p^2 + \sqrt{f_p^4 + f_r^4}. \tag{2.58}$$

Because the damping increases proportional to f_r^2 (Eq. 2.55), as we attempt to drive the laser harder to increase f_r, the response flattens out as illustrated in Fig. 2.11. At some point, the damping becomes large enough that the response drops below the 3 dB cutoff at frequencies less than f_r. As a result, there is a maximum bandwidth that can be achieved. Using the Eqs. (2.57)

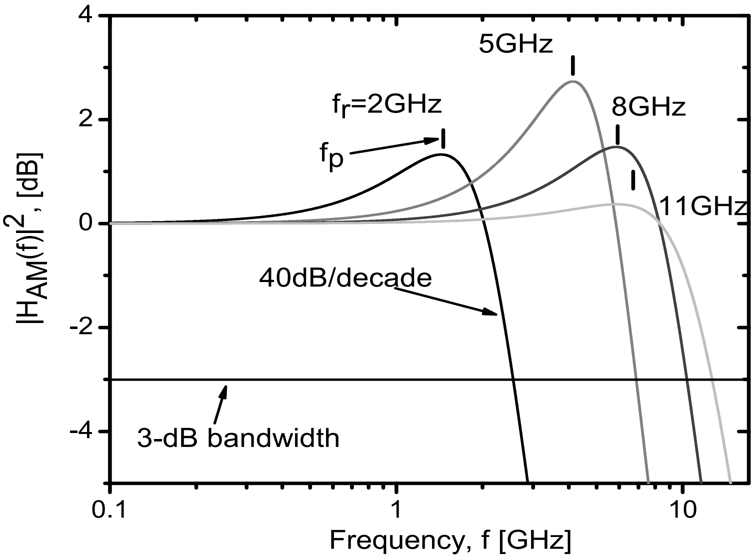

Figure 2.11.: Small-signal intensity modulation of an ideal laser for different resonance frequencies and fixed damping rate.

and (2.58) combined with the definition of γ (neglecting γ_0) from Eq. (2.55), the modulation bandwidth for a low damping as well as the maximum possible bandwidth $f_{3dB|damping}$, which is limited by the damping rate in the absence of the thermal and parasitic limitations, can be determined [28] [33]:

$$f_{3dB} \approx f_r\sqrt{1+\sqrt{2}} \approx 1.55 f_r \qquad (\gamma/\omega_r \ll 1), \tag{2.59}$$

$$f_{3dB|damping} = \sqrt{2}\frac{2\pi}{K} \qquad (\gamma/\omega_r = \sqrt{2}). \tag{2.60}$$

The modulation bandwidth increases linearly with the relaxation resonance frequency and remains about 50% larger than f_r until the damping becomes strong. With the strong damping the bandwidth is compromised and decreases as f_r and γ further increase.

Ideally a wide-band laser should have a large 3-dB modulation bandwidth and a strongly damped resonance peak to provide a flat response. These objectives are achieved simultaneously if f_r is large (Fig. 2.11).

According to Eq. (2.54), there are three direct methods to increase the value of f_r [34]. The first method is to increase the photon density N_p. For a given output power this can be achieved by decreasing the width of the optical field distribution in the transverse direction. The photon density can be further increased by driving the laser well above threshold. Heating may lead to reliability problems at high current levels and limit the available bandwidth due to a reduction in the value of the gain. Well-designed wide-band lasers should therefore have low threshold currents and good heat sinking.

A second method to increasing f_r is to increase the gain slope a. This can be achieved by decreasing the temperature and by increasing the doping level in the active layer. A third method to increase f_r is to reduce the photon lifetime τ_p by reducing the cavity length of the device or using mirrors with higher reflectivities.

In the reality the measured transfer function of the small-signal amplitude modulation includes additionally parasitic and thermal distortions and they will affect the shape of the characteristic of the transfer function.

2.3.4. Large-Signal Amplitude Modulation

The large-signal dynamic response of a semiconductor laser can be quite complex due to the highly nonlinear properties of the device. The output waveform depends strongly on the frequency and the amplitude of the input signal. The rate equations can be used to model large-signal modulation dynamics, but the complexity of the large-signal waveform will often necessitate a numerical solution technique. On the other hand, analytical solutions (where feasible) can give insights into the parameters which limit speed of response and pulse width [34] [35] [36]. For a system employing single-mode VCSELs, mainly three terms have an impact on the modulation performance and have been investigated experimentally in [37]. Firstly, a turn-on delay occurs if the VCSEL is biased below threshold and time is taken to build up the threshold carrier density in the active layer. Secondly, there is a turn-on jitter as the standard deviation of the turn-on delay which is caused by the fluctuations due to the spontaneous emission. Finally, the so-called pattern effects, due to the memory-like behavior of the carrier reservoir, resulting in cavity build-up time variations, play a major role in practice, even for the bias points above threshold.

A simple analytical expression is derived for the turn-on time of a laser switched using a step current waveform above threshold. This turn-on time is an important parameter affecting the maximum achieved bit rate in digital systems, and influences the chirp characteristics. The analysis shows how the large-signal switching speed can be related to the small-signal bandwidth. Fig. 2.12 shows the idealized step input current and the resulting large-signal time response.

The off-level drive current and the output power are I_{off} and P_{off}, respectively, and the cor-

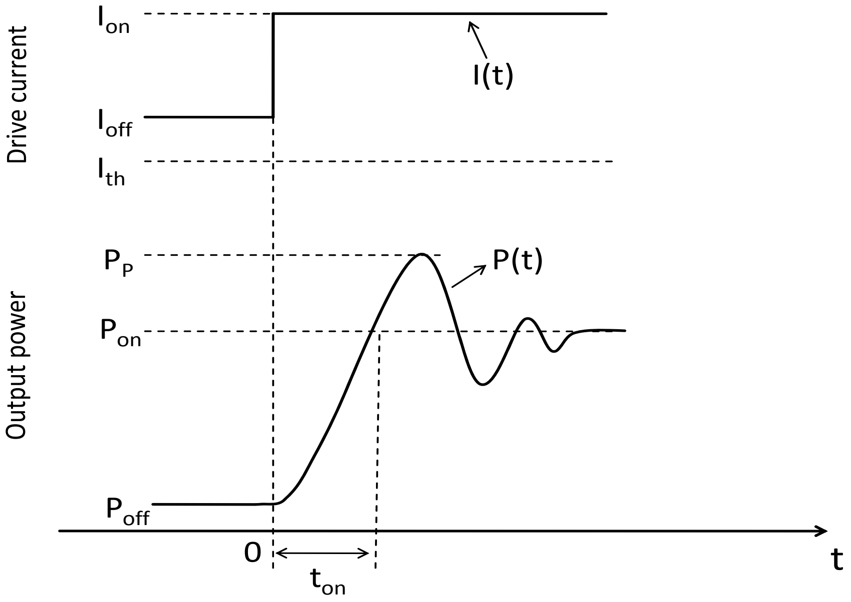

Figure 2.12.: Step input current and laser response for $I_{off} > I_{th}$.

responding on-level values are I_{on} and P_{on}. It is common practice in the high bit-rate systems to bias the laser above threshold such as $I_{off} > I_{th}$. The turn-on time t_{on} is defined as the time taken for the output power $P(t)$ to reach the value P_{on}. The peak value of $P(t)$ is P_p. A numerical analysis of the full rate equations [34] [38] shows that if the laser is switched on from below threshold, then the stimulated and spontaneous recombination term in the carrier rate equation are small and can be ignored for $t < t_{on}$. The same conclusion applies if I_{off} is just above the threshold. Therefore for $t < t_{on}$, Eq. (2.47) becomes [34]:

$$\frac{dN}{dt} \approx \eta_i \frac{I}{qV_a}. \tag{2.61}$$

The solution to this simple differential equation (for $0 \leq t \leq t_{on}$) is [34]:

$$N = N_{off} + \frac{(I_{on} - I_{off})t}{qV_a}, \tag{2.62}$$

where N_{off} is the off-level electron density. For low and moderate output power levels the output power becomes [34]:

$$P(t) = P_{off}\, exp\left\{\frac{g(N_{P,on} - N_{P,off})t^2}{2\tau_p}\right\}, \tag{2.63}$$

where $N_{P,on}$ and $N_{P,off}$ are the on-level and the off-level photon densities. For $N_{P,off} \ll N_{P,on}$ the turn-on time becomes [34]:

$$t_{on} = \frac{\sqrt{2}}{2\pi f_{r,on}}\left[\ln\left(\frac{P_{on}}{P_{off}}\right)\right]^{1/2}, \tag{2.64}$$

where $f_{r,on}$ is the on-level value of f_r. Eq. (2.64) highlights the importance of the resonance frequency from the small-signal analysis and the on-off ratio P_{on}/P_{off} for determining the turn-on time. The turn-on time decreases by increasing f_r or by decreasing P_{on}/P_{off}. A similar analysis has shown that the overshoot P_p/P_{on} also decreases with decreasing P_{on}/P_{off} but the turn-off time is almost independent of P_{on}/P_{off} [39]. The calculations show that the turn-on behavior is improved if the device is biased above threshold and the eye-diagram measurements show that as I_{off}/I_{th} increases, the overshoot decreases and the pulse width increases due to the decreasing value of t_{on} [34]. In communication applications it may be necessary to trade off this improvement in laser response against the effective receiver sensitivity, which decreases at low on-off ratios.

If the bias current is below the threshold, the carrier density N is smaller than the threshold density N_{th} yielding a normalized gain g considerably smaller than unity [40]. Appreciable photon numbers are obtained only if the gain is extremly close to unity. Therefore, for $N < N_{th}$, the photon number N_P is very small and may be neglected in the rate equations [40]. If the current is switched on at $t = 0$ from $I = I_{off}$ below the threshold to $I = I_{on}$ above the threshold as in Fig. 2.13, the carrier density will steadily increase from its below-threshold value until the threshold carrier density N_{th} is reached. This turn-on delay t_s is governed by the carrier life time τ_{Δ_N} and is given by [40]:

$$t_s = \tau_{\Delta_N} \ln\frac{I_{on} - I_{off}}{I_{on} - I_{th}}, \qquad I_{off} < I_{th} < I_{on}. \tag{2.65}$$

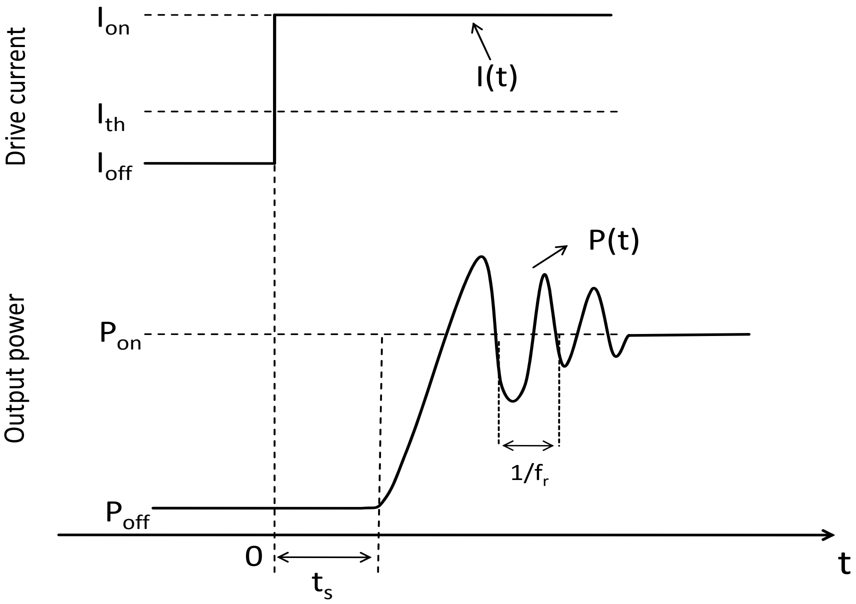

Figure 2.13.: Step input current and laser response for $I_{off} < I_{th}$.

Since the carrier life time τ_{Δ_N} is of the order of several ns, one obtains a turn-on delay of a similar order of magnitude if the laser diode is biased below the threshold. For the high bit rate transmission such a large turn-on delay can not be tolerated.

2.3.5. Relative Intensity Noise and Linewidth

In the steady state, it has been assumed that the carrier- and photon-densities are constant. However, in reality the random carrier and photon recombination and generation events produce instantaneous time variation in the carrier and the photon densities, even without applying current modulation. The variation in the photon density leads to the variations in the magnitude of the output power, which provides a noise floor and the variations in the carrier density result in variations in the output wavelength, which creates a finite spectral linewidth for the lasing mode [28].

To determine the laser RIN and linewidth, output power and carrier noise fluctuations should be determined. For this purpose the Langevin noise source $F_N(t)$ and $F_P(t)$ as the driving sources for the fluctuations of carrier- and photon-densities with $S_N(f)$ and $S_{N_P}(f)$ as their power spectrum densities are introduced. These sources are assumed to be white noise and are assumed small enough that a linearization of the rate equations can be used.

Relative Intensity Noise (RIN)

In terms of the spectral density of the noise $S_{\delta P}$ accompanying the signal intensity P_0, the RIN spectrum per unit frequency $\mathrm{RIN}(f)$ can be defined as:

$$\mathrm{RIN}(f) = \frac{S_{\delta P}(f)}{P_0^2}, \tag{2.66}$$

with $S_{\delta P}$ as the spectral density of the power fluctuation δP per unit frequency and P_0 as the average optical output power. It can be shown that $S_{\delta P}$ is obtained from the $S_{N_P}(f)$ and $S_N(f)$. In the absence of the shot-noise, the simplified form of $S_{\delta P}$ for the above-threshold condition is given by [28] [33]:

$$S_{\delta P}(f) = P_0^2 \frac{Af^2 + B}{(f_r^2 - f^2)^2 + \left(\frac{\gamma}{2\pi}\right)^2 f^2}. \tag{2.67}$$

From Eq. (2.67), RIN(f) can be obtained as [31]:

$$\text{RIN}(f) = \frac{Af^2 + B}{(f_r^2 - f^2)^2 + \left(\frac{\gamma}{2\pi}\right)^2 f^2}. \tag{2.68}$$

A and B are constants defined as:

$$A = \frac{\beta_{sp}\Gamma N_0}{\pi^2 \tau_{sp} \langle N_p \rangle} \quad B = \frac{\beta_{sp}\Gamma N_0 \gamma^{*2}}{4\pi^4 \tau_{sp} \langle N_p \rangle}, \tag{2.69}$$

with the modified damping coefficient [31]:

$$\gamma^* \approx \gamma_0 + 4\pi^2 f_r^2 \tau_p. \tag{2.70}$$

$\langle N_p \rangle$ is the mean value of the photon density N_p. If the emitted field is in a perfectly coherent state, the output power noise spectral density $S_{\delta P}$ is limited to a minimum value of S_{shot}. This quantum noise floor of the coherent field is often referred to as the standard quantum limit or the shot-noise (this is different as the photo detector shot-noise) floor and is given by:

$$S_{\text{shot}} = hfP_0. \tag{2.71}$$

S_{shot} is the standard quantum limit for the minimum RIN. Considering the shot noise, $S_{\delta P}(f)$ and RIN(f) from Eq. (2.67) and Eq. (2.68) will turn to:

$$\begin{aligned} S_{\delta P}(f) &= P_0^2 \frac{Af^2 + B}{(f_r^2 - f^2)^2 + \left(\frac{\gamma}{2\pi}\right)^2 f^2} + S_{\text{shot}}, && (2.72) \\ \text{RIN}(f) &= \frac{Af^2 + B}{(f_r^2 - f^2)^2 + \left(\frac{\gamma}{2\pi}\right)^2 f^2} + \frac{hf}{P_0}. && (2.73) \end{aligned}$$

Linewidth

In addition to the intensity noise, the laser also produces frequency noise that can adversely affect the lasing spectrum. The linewidth of a diode laser results from the phase fluctuations in its output [28]. It is well known that the statistical phase fluctuations of the electric field introduced by spontaneous emission processes are responsible for the finite linewidth of the laser diode oscillation. The spectral power density of a single-mode laser emission line is well approximated by the Lorenzian line-shape function [31]:

$$\left|\widetilde{E}(f)\right|^2 = \left|\widetilde{E}(f_m)\right|^2 \frac{(\Delta f_L/2)^2}{(\Delta f_L/2)^2 + (f - f_m)^2}, \tag{2.74}$$

where f_m is the center frequency of the mode and Δf_L is the full linewidth at half maximum. The linewidth is given by [31]:

$$\Delta f_L = \frac{\beta_{sp}\Gamma_t \langle N \rangle}{4\pi\tau_{sp}\langle N_p \rangle}(1+\alpha_H^2), \tag{2.75}$$

where α_H is the linewidth enhancement factor (also called Henry factor) that typically takes values between -2 and -7. Eq. (2.75) shows that the linewidth increases linearly with the inverse output power $1/P$ ($P \propto N_p$). However, a residual linewidth Δf_0 is observed for the extrapolation $P \rightarrow \infty$, which is attributed to mode competition with imperfectly suppressed side-modes or $1/f-$noise contributions [31] [40].

The onset of the higher transverse order modes at the higher currents generally leads to an increase of the fundamental mode linewidth due to the reduction of modal power, although the total power is still increasing [31].

In typical applications of the diode lasers some light is unintentionally reflected back into the laser cavity. For example, the reflection from the front surface of a fiber is about 4% and perhaps one-tenth of this may be coupled back into the laser cavity in a pigtailing arrangement. Surprisingly, even such small amounts of feedback can have dramatic effects on the laser linewidth noise properties. This is specially true for the single-frequency lasers. In fact, 0.4% (-24 dB) is considered to be a large feedback. Experiments have shown that even -60 dB of feedback can be unacceptable with the single-frequency lasers [28].

2.3.6. Single-Mode Operation and Polarization Stability

There are several techniques to suppress the higher order transverse modes in VCSELs. Some of them are using an oxide aperture [41], extended cavity technique [42], introducing two-dimensional photonic crystals in the VCSEL [43] [44], introducing shallow surface relief in the top mirror [45] and using a buried tunnel junction [24]. All these techniques have their advantages and disadvantages and are described and discussed in [46].

In the device presented here, a half-symmetric resonator, achieved by a curved membrane and in combination with an oxide aperture, supports the fundamental mode (Gaussian beam) of the VCSEL and makes the single transversal mode operation of the device possible. This plane concave resonator makes it possible to fit the beam waist of the fundamental mode (by changing the air-gap and the RoC) into the oxide aperture. We are thus able to use a larger oxide aperture. The larger oxide aperture enhances the temperature behavior of the device and thus increases the output power during the single-mode operation. The limitation for the single-mode operation is then the non homogeneous current distribution in the half-VCSEL. If the current density is much higher at the edges compared to the center of the device, then the next transverse modes will get a higher gain and start to lase.

The polarization properties of the light emitted by a semiconductor laser are predominately determined by the polarization properties of the gain, i.e., by the interband optical transition matrix element [47], and by the polarization properties of the optical cavity [48]. The anisotropic cavity shape and the perpendicular direction of carrier injection to the light emission fix the polarization in edge-emitter lasers in a specific direction (i.e., parallel with the active layer).

The polarization behavior of VCSELs is not a trivial matter and the polarization state in a

VCSEL is not defined a priori by its structure. Due to the VCSEL's direction of lasing perpendicular to the active region, the transition strength is the same for all polarization directions perpendicular to the direction of light emission. Furthermore, the quasi-cylindrical symmetry of the VCSEL's structure leads only to a small waveguide anisotropy. In summary, the gain and optical properties of VCSELs are isotropic for all polarizations perpendicular to the direction of light emission and therefore there is no intrinsic polarization selection mechanism in VCSELs. Nevertheless, real VCSELs do emit linearly polarized light. Sometimes the direction of the state of polarization in the transverse plane is randomly distributed from VCSEL to VCSEL, but usually there is a preference for a polarization direction along the $[110]$ and $[1\bar{1}0]$ crystallographic axes for VCSELs grown on a (011) oriented substrate. This has been attributed to birefringence introduced by unintentional stress during manufacturing and by the electro-optic effect in the cavity and the mirrors.

But even VCSELs grown on the same wafer do not necessarily all have the same polarization direction preference. Polarization switching (PS) from one state to the orthogonal one is often observed as the current is changed. Quite some experimental and theoretical work has been performed aimed at understanding the origin of the linear polarization state and the polarization switching that can occur in VCSELs when the current is modulated the substrate temperature is changed or external stress is applied e.g. [48].

This switching can occur in both the single-mode and multi-mode region of the power-current curve. In the fundamental mode, the switching mostly takes place between two orthogonal modes having a small frequency difference of the order of 1 to 40 GHz. This splitting is due to residual stress, birefringence and the electro-optic effect induced by the voltage drop over active region.

To be able to control the state of polarization, the introduced anisotropy must of course be stronger than the inherent anisotropy of the device [46]. For non-tunable VCSELs some polarization controlling techniques have been reported. For example, gain anisotropy is achieved by epitaxial growth on non-(100) substrate such as GaAs (311)A [49] and GaAs (311)B [50]. The drawback of using non-(100) substrates is that it becomes more difficult to fabricate a symmetric oxide aperture. Other polarization stabilizing techniques are using an asymmetric current injection to introduce both anisotropic gain and cavity losses [51], introducing anisotropic strain in the VCSEL via etching deep trenches close to the VCSEL aperture along the preferential polarization direction [52] or via using strained T-bars [53] and implementing a surface grating [46]. All these methods have their drawbacks and advantages discussed partly in [46].

In this work a sub-wavelength grating (SWG) is implemented on the half-VCSEL air interface to select one polarization mode. A SWG is a grating which has a periodicity shorter than the optical wavelength in the material [54]. The electrical field of the wave polarized parallel or perpendicular to the SWG experiences the grating as a homogeneous medium, but with different effective refractive indices ($n_{\|}$ for the parallel field and $n_{\perp}$ for the perpendicular field) given by [55]:

$$n_{\|}^2 = \frac{d_1 n_1^2 + d_2 n_2^2}{d_1 + d_2} \quad ; \quad n_{\perp}^2 = \frac{(d_1 + d_2) n_1^2 n_2^2}{d_2 n_1^2 + d_1 n_2^2}. \tag{2.76}$$

Here, d_1 is the width of the ridges, n_1 is the refractive index of the material, d_2 is the width of the grooves and n_2 is the refractive index of the ambient material (i.e. $n_2 = 1$ in case of air) as shown in Fig. 2.14. The effective refractive index is higher in the direction parallel to the

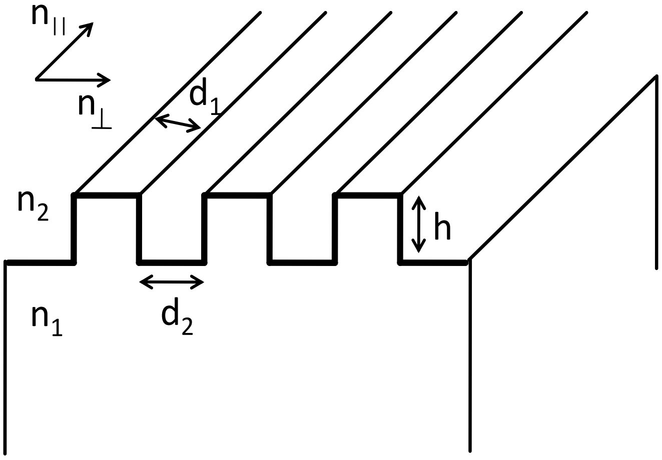

Figure 2.14.: Sub-wavelength grating.

grating. The difference is maximum for a duty cycle ($d_1/(d_1+d_2)$) of around 50%, i.e. $d_1 = d_2$. This can be used to manipulate the reflection phase and adjust the threshold gain (difference) of two polarization modes. Using this simple model, the polarization selectivity can be calculated by means of one-dimensional transfer matrix simulations.

3. Half-VCSEL

A half-VCSEL is basically a VCSEL without the top DBR. It includes a bottom DBR, an active region and a current aperture. In the first section of this chapter, the general structure and materials of the half-VCSELs and their transmission line structure are introduced. The second section includes the fabrication steps of the whole half-VCSEL starting from the epitaxial material without SWG. In the third section, the structure and the fabrication of the half-VCSEL with SWG is introduced and its difference from the one without SWG is described.

3.1. Design and Material

The half-VCSEL presented in this work can be divided in two parts. The first part is the mesa which includes the bottom DBR, the active region and the current aperture. The second part is a microstrip transmission line for high amplitude modulation applications as is shown in Fig. 3.1. Fig. 3.1(a) shows the top view of a half-VCSEL with the mesa and its transmission line. Fig. 3.1(b) shows the microscope image of the top view of the half-VCSEL chip with several half-VCSELs on it. Fig. 3.1(c) is the cross section view of the half-VCSEL and Fig. 3.1(d) is a microscope image with a higher resolution of the mesa of a single half-VCSEL.

The mesa structure of the half-VCSEL without the sub-wavelength grating is presented in details in Fig. 3.2. Starting from the bottom, the GaAs-based half-VCSEL consists of an undoped GaAs substrate and a n-type GaAs contact layer above the bottom n-contact (Ni/Ge/Au). Above the n-contact there is a n-doped DBR with 36.5 pairs of $\mathrm{Al_{0.9}Ga_{0.1}As/Al_{0.1}Ga_{0.9}As}$ and a reflectivity of $\approx 100\%$. The active region consists of three GaAs/AlGaAs quantum wells (QW) located at an anti-node of the optical field for maximum amplification. The current aperture is formed in a later process by selective lateral oxidation of an $\mathrm{Al_{0.98}Ga_{0.02}As}$-layer for minimum optical confinement [46], which is located at a node of the standing wave. Three 50 nm thick highly p^+-doped (5.10^{18}cm^{-3}) current spreading layers are inserted at the nodes above the oxide aperture to reduce the effect of current crowding. These layers are followed by a highly p-doped (1.10^{20}cm^{-3}) GaAs top-contact layer with a thickness of 3 nm. Additionally the semiconductor-air interface is covered with a $\lambda/4$-thick SiN_x anti reflection coating (extended cavity design from Sec. 4.5) to enhance the nominal reflectivity of the upper Bragg mirror. The epitaxial structure of the GaAs-based half-VCSEL is shown in App. B.

In order to provide the VCSEL with high frequency modulation signals via microwave pico-probes and to avoid physical interaction between the pico-probes and the later adjusted (or deposited) membrane, a microstrip transmission line has been implemented. The microstrip line is made of a ground plane and a signal line with a width of 15 μm (Fig. 3.1(a)). The space between the ground plane and the signal line (5 μm) is filled by Benzo-cyclo-buteno (BCB), which has a low dielectric constant of $\epsilon_r = 2.5$ (Fig. 3.1 (c)).

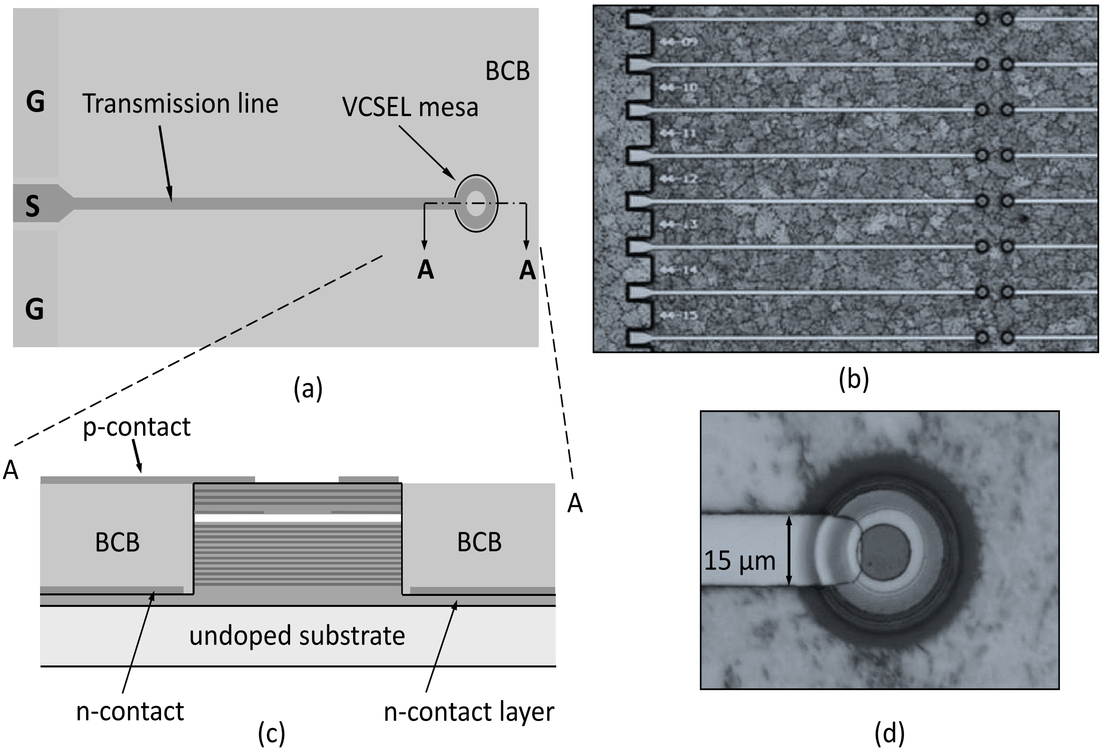

Figure 3.1.: (a) Top view of the half-VCSEL with mesa and transmission line. (b) Microscope image of the half-VCSEL chip. (c) Cross-section view of the half-VCSEL. (d) Microscope image of a single device.

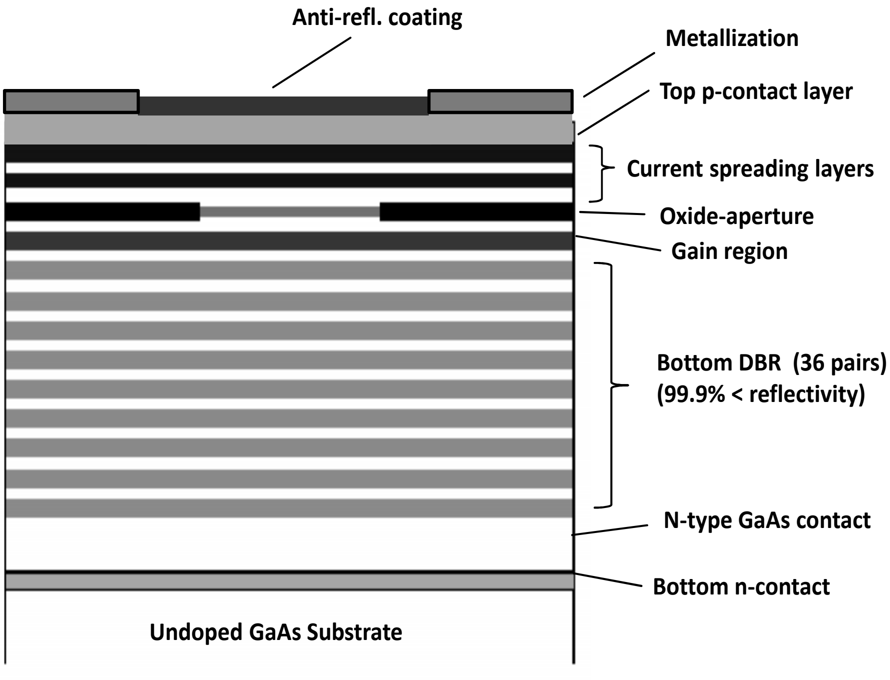

Figure 3.2.: Detailed cross view of the mesa structure.

3.2. Fabrication Steps

This section summarizes briefly the process steps to fabricate the half-VCSEL from the epitaxial material. The fabrication of the half-VCSEL has been done by Chalmers University of Technology in Gothenburg Sweden. The fabrication process comprises 6 to 7 lithography steps. A similar full-VCSEL technology is outlined in [56]. After cleaving the wafer into pieces of 14×18 mm^2 and cleaning them in solvents, top contact rings and several alignment marks are defined by image reversal photo lithography. The p-contact metals (Ti/Au) are sputtered and structured in a lift-off process.

To protect the device during the subsequent oxidation steps the chips are coated with siliconnitride (SiN$_x$) using plasma-enhanced chemical vapor deposition (PECVD). The mesa structure is defined by photo lithography and is dry etched by means of reactive ion etching (RIE). The RIE system is equipped with a laser interferometer for in-situ control of the etching depth.

The Al-rich (98$\%$) layer is laterally wet-oxidized in a furnace at 420^oC for 30-40 min to form current apertures. Fig. 3.3 shows the infrared microscope image of the half-VCSEL. The oxide aperture of the half-VCSEL is indicated in this figure. The directed horizontal stream of the oxidant (N$_2/$H$_2$o) results in a gradual oxidation rate of 0.37 to 0.44 μm/min, which can be compensated by a proper alignment of different mesa diameters.

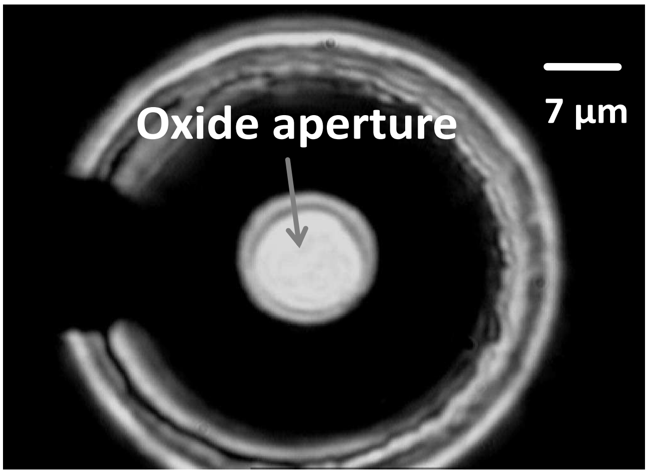

Figure 3.3.: Infrared microscope image of the mesa. The white circle in the mesa is the oxide aperture.

After removal of the SiN$_x$ cap by means of RIE, the n-contact plane (ground plane) is defined by lithography. The n-contact (Ni/Ge/Au) is deposited using e-beam evaporation and then rapidly annealed at 420^oC for 30 s. The contact layer is supported by additionally sputtering Ti/Au.

BCB is spun on the half-VCSEL chip to plane the mesa structures with a height of around 5.6 μm. The BCB (via negative photo-resist) is structured in a lithography step, cured at 260^oC for 60 min, and dry etched to clear the mesa surface and adjust the desired thickness.

Finally, the top contact ring is connected with a microstrip transmission line, which is sputtered on the BCB. The Ti/Au-microstrip has a width of 15 μm and is designed to match 50 Ω. The half-VCSELs can be contacted with a 100 μm pitch size GSG-probe.

3.3. Half-VCSEL with SWG

There are several positions to implement the SWG into the VCSEL as shown in Fig. 3.4. The grating can be implemented on top of the top mirror (pos. 1), on bottom of the top mirror (pos. 2), at the half-VCSEL air interface (pos. 3), on top of the bottom mirror (pos. 4) and on bottom of the bottom mirror (pos. 5). All these positions have different difficulties to be implemented with SWG and they have different impact on polarization selectivity. The selection of the location is a trade off between theoretical investigations and technological constraints. Although the theoretically optimal locations were at position 1 and 5, to make the fabrication easier, the grating is implemented on position 3 in (011) crystallographic direction (Fig. 3.4).

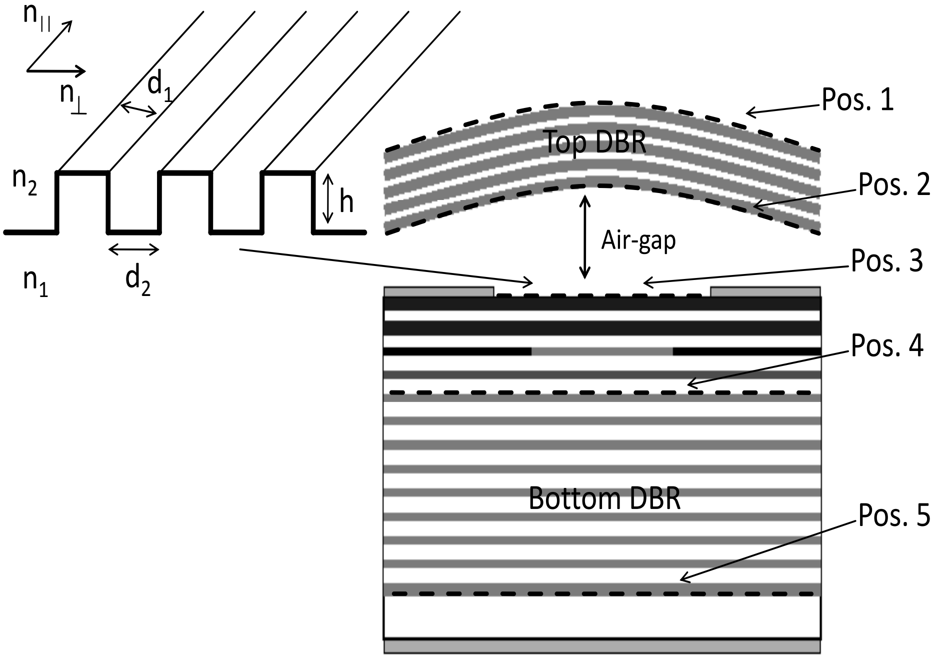

Figure 3.4.: SWG pattern and possible positions to implement the grating in the VCSEL.

To realize the SWG on top of the half-VCSELs, electron beam lithography (EBL) in combination with dry etching has been utilized. EBL offers an accurate nm-sized patterning by scanning an electron beam in a pre-determined pattern across the sample covered with resist. The electrons will experience both forward and backscattering both in the resist and in the sample. For this type of pattern exposure the effects of the backscattered electrons are most important to consider.

If no proximity-effect compensation is included, the backscattered electrons will give a background that is not uniform over the exposed area and result in larger ridge width in the outer region of the grating compared to the center. To avoid this variation of duty cycle across the grating, optical proximity correction (OPC) was included in the file preparation and compensated patterns were exposed.

The half-VCSEL chip, which has been used for the SWG, has two main differences beside the grating with the chip introduced in Sec. 3.1. The first difference is that the top p-contact layer (below the SiN$_x$-coating) after epitaxial growth is 92 nm thick instead of 3 nm in the first design. The second difference is changing the chip layout from double-columns (two columns of half-VCSELs next to each other) to a single-column as shown in Fig. 3.5. This makes the assembly of the membrane on the half-VCSEL chip easier. The first processing step for the half-VCSELs with SWG is to etch back the top p-contact layer. The underlying material has a 92 nm-thick highly p-doped GaAs top-contact. This layer has to be etched back. A contact layer with a thickness of 10 nm is chosen as a trade-off between the absorption loss and the contact resistance. After dry-etching of the contact layer, e-beam lithography and dry-etching of the SWG, p-contact rings are sputtered onto the half-VCSEL chip. The rest of the processing steps are the same as the device without grating.

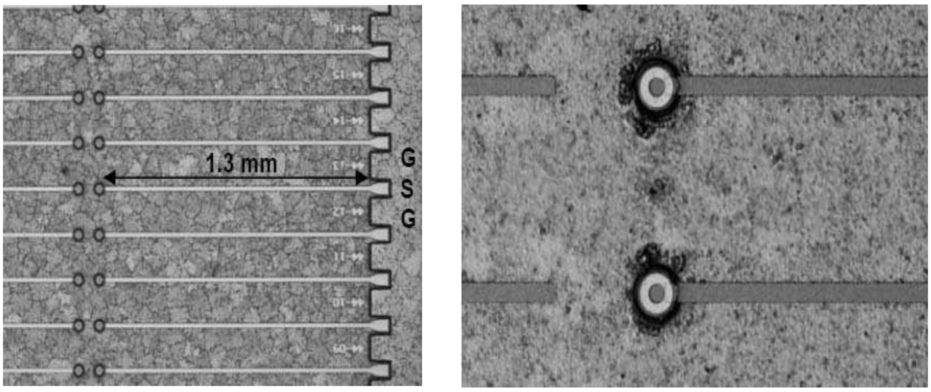

(a) (b)

Figure 3.5.: (a) Double-column layout of the chip without the grating. (b) single-column layout of the chip with grating.

Fig. 3.6 and 3.7 show the high resolution electron microscope (HREM) image and atomic force microscope (AFM) image of the grating on the investigated half-VCSEL after finishing the device processing. The images show that finally a period of $d_1 + d_2 = 200$ nm (Fig. 3.4) and an etch depth of $h \approx 50$ nm have been achieved. The irregularity in the grating (Fig. 3.6) compared to the case from Fig. (3.4) is due to the $\lambda/4$-thick coating on the grating that is deposited after implementing of the grating.

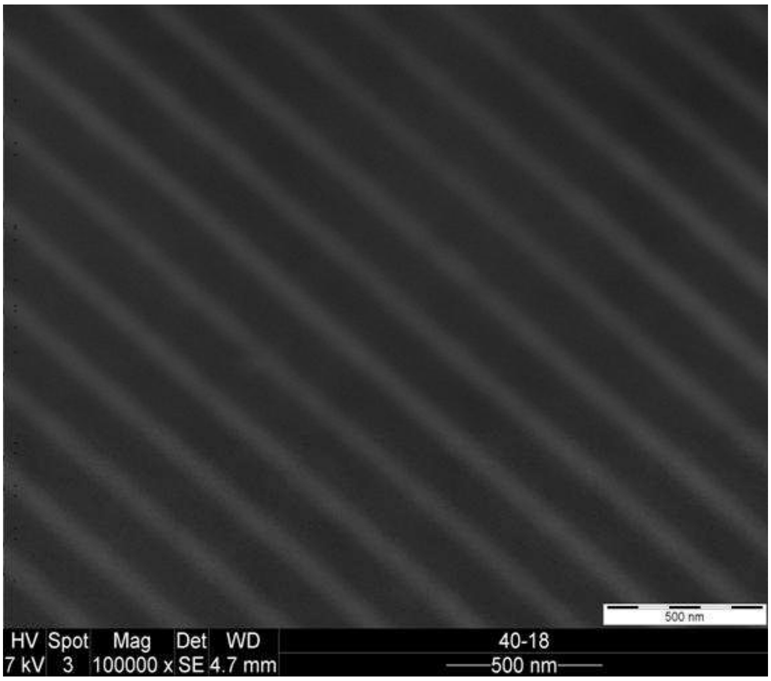

Figure 3.6.: HREM image of the half-VCSEL after deposition of the $\lambda/4$-thick SiN$_x$-coating.

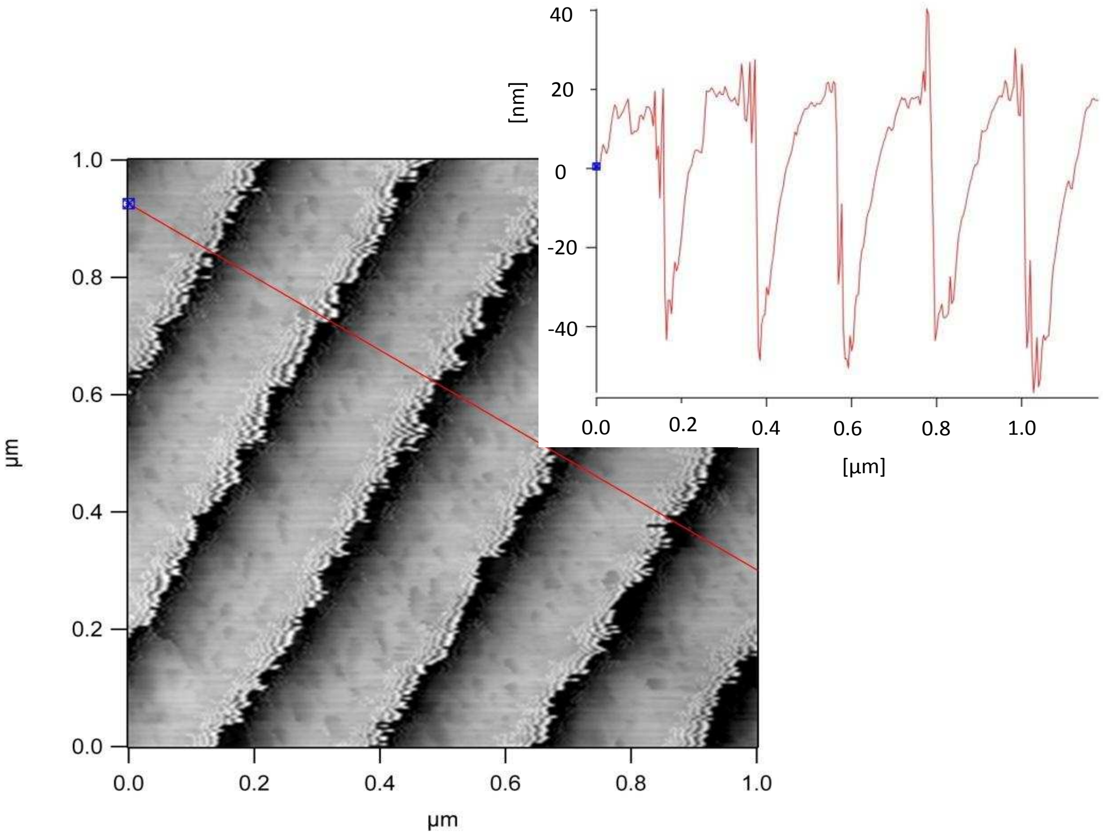

Figure 3.7.: AFM image of the half-VCSEL after deposition of the $\lambda/4$-thick SiN$_x$-coating.

4. Movable Top MEMS-Membrane and VCSEL Modeling

To be able to change the cavity length of the VCSEL and obtain the tuning, a Micro-Electro-Mechanical System (MEMS) -membrane as the top mirror is applied. Different assembly methods of the membrane on the half-VCSEL and different materials for the membrane have been investigated and implemented in this work. The properties of the VCSELs are modeled via simulations and the results are reported. The first section of this chapter describes the general shape and structure of the membrane, as well as different assembly methods of the membrane on the half-VCSEL. The second section is about semiconductor membranes. Different types of semiconductor membranes and their fabrication methods are introduced. The third section describes a hybrid membrane, consisting of dielectric and semiconductor layers, its structure and fabrication method. The forth section is about the dielectric mirror membranes. In the last section the whole VCSEL is modeled using one-dimensional simulations. The influence of the membrane on the modulation bandwidth of the transmission line is investigated at the end of the chapter.

4.1. General Shape and Assembly

Three kinds of membranes have been developed and fabricated in this work. They are semiconductor, hybrid and dielectric membranes. The shape of the mirror membrane, which is common in all types of the membranes, is shown in Fig. 4.1. Fig. 4.1(a) shows the two dimensional layout of the membrane. The MEMS-membrane in this work consists of the main mirror, suspension beams and the frame. The main mirror is suspended from the membrane frame with four suspension beams. The suspension beams hold the mirror, connect it with the frame of the membrane and additionally transport the current through the membrane for electro thermal actuation and tuning.

In all structures an electro thermal tuning current, connected to the membrane frame, flows through the suspension beams and the mirror. It cause a thermal expanding of the suspension beams and thus an increase of the resonator length causing a wavelength tuning. Fig. 4.1(b) shows the three dimensional (upside down) confocal microscope image of the membrane. The air gap and the membrane curvature are indicated in the figure. Fig. 4.2 shows the current flow through the membrane. There is a difference between the current flow in the semiconductor-based membranes and in dielectric ones that is discussed in the next section.

Two methods are applied in this work to join the membrane and the half-VCSEL. The first one is a two-chip concept called bulk-micromachining [60]. The second one is a monolithic concept called surface-micromachining [58]. In the first method the half-VCSEL and membrane are processed and optimized separately before they are joined together. This method is applied in

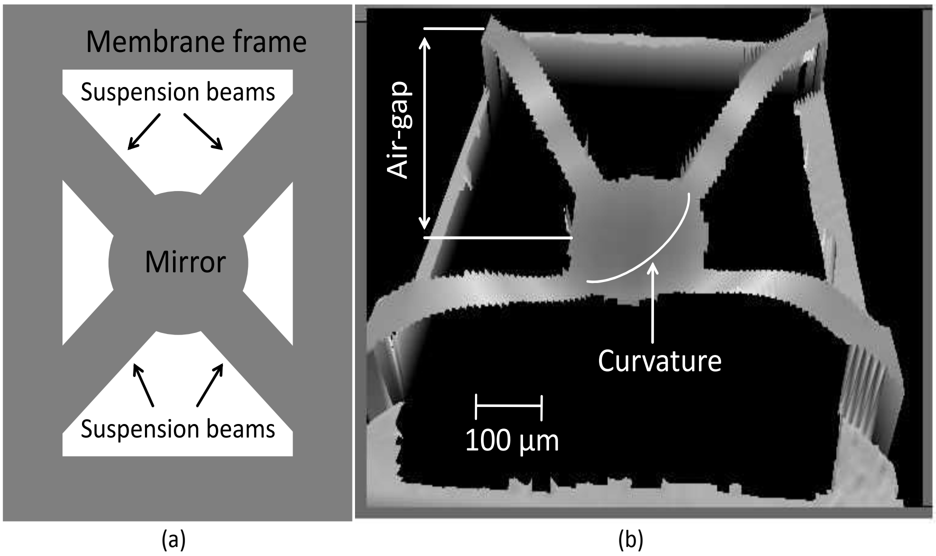

Figure 4.1.: (a) Two dimensional design of the membrane. (b) Three dimensional (upside down) confocal microscope image of the membrane.

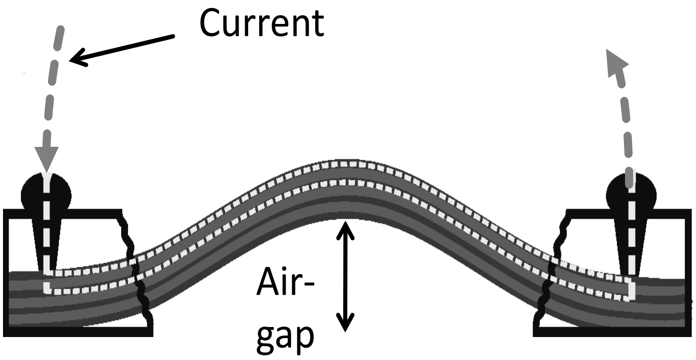

Figure 4.2.: Electro thermal tuning current through the membrane.

this work to make VCSELs with semiconductor-based membranes. The processing and fabrication of those membranes is introduced in the next section. After processing of the membrane, it is placed on the half-VCSEL and is adjusted there using micro-manipulators. After adjustment and controlling the properties by coupling the output light into the fiber, the membrane is fixed to the half-VCSEL using an ultra violet adhesive. The adhesive will fix the membrane to the half-VCSEL at three locations. Fig. 4.3 shows the microscope image of a bulk-micromachined VCSEL.

The main advantage of the two-chip concept compared to a monolithic solution is that both chips can be optimized separately without the need of making disadvantageous compromises either for the micro-mechanical part or for the VCSEL. On the other hand there are also certain drawbacks of the two-chip concept. One is the necessity of an additional assembly step to join both parts. It is time consuming, expensive and a good reproducibility is difficult to achieve. Another drawback is that a mass production of these VCSELs is not easy at all.

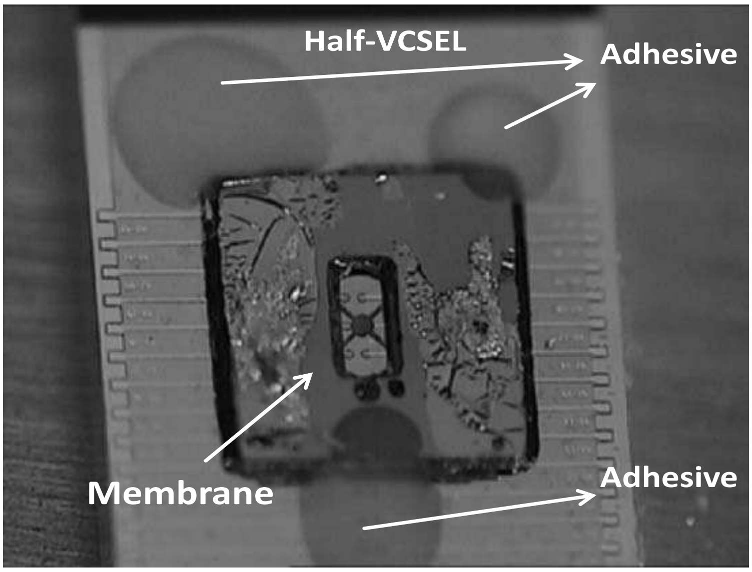

Figure 4.3.: Bulk-micromachined VCSEL with a semiconductor membrane.

In this work also the surface-micromachining method is applied to the VCSELs with dielectric mirrors. This method allows a direct deposition of the membrane on the half-VCSEL, resulting in an accuracy defined by the used lithography. Using this technology the RoC and the air-gap of the membrane can be fabricated accurate and reproducible. Additionally, this method is suitable for mass production too. Fig. 4.4 shows a surface-micromachined VCSEL with a deposited dielectric mirror.

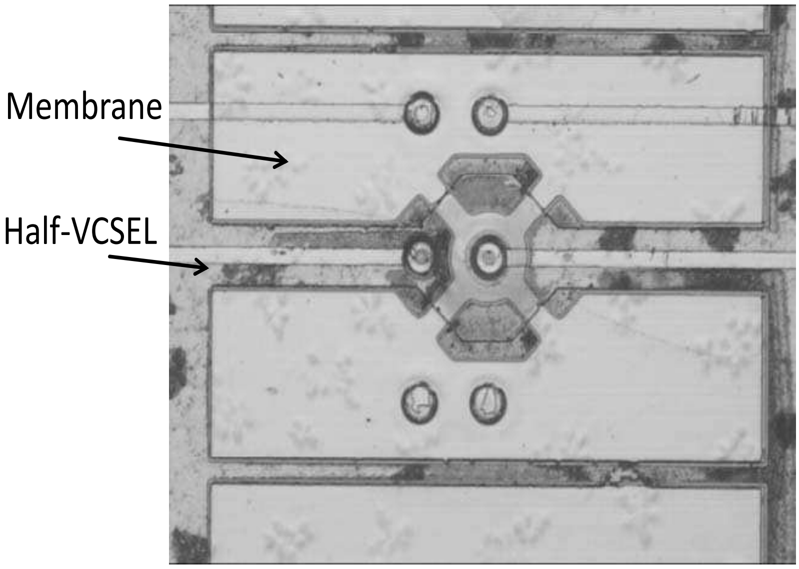

Figure 4.4.: Surface-micromachined VCSEL with a dielectric membrane.

4.2. Semiconductor Membrane

The semiconductor membrane in this work is a highly reflective DBR made out of semiconductor layers. The design and fabrication of these DBRs are introduced in following.

4.2.1. Structure and Design

The membrane consists of AlGa(In)As layers grown by the molecular beam epitaxy (MBE) on undoped GaAs substrate. The high-index layers have an aluminum-content of 15 $\%$ and a refraction index of about $n \approx 3.4$. The low index layers on the other hand have an aluminum-content of 85 $\%$ and a refractive index of about $n \approx 3$. In total a refractive index difference of about 0.4 is achieved. A maximum reflectivity of about 99.8 $\%$ has been designed for the top mirror and it is realized by 22.5 $Al_xGa_{1-x}(In)As$ pairs (45 layers).
According to the thickness of the layers, two different DBR structures have been implemented and tested. The first DBR was based on the experiences with the 1.5 μm tunable VCSELs achieved in TU-Darmstadt. The DBR structure consists of 22.5 pairs. The whole thickness of this structure amounts about 3 μm (App. C, table C.1). Due to the small thickness of the DBR, the processing of it is difficult. To overcome this problem, a second DBR is developed. It consists of 15 pairs with $\lambda/4$-thickness and 8 pairs with $3\lambda/4$-thickness. The structure of this DBR is shown in table C.2 of App. C. By applying the $3\lambda/4$-thick pairs the total thickness of the DBR amounts to about 5 μm.
The advantage of using a thicker DBR to fabricate the membrane is due to the robustness to the process environment during the fabrication. The disadvantage of this measure is the reduced bandwidth, which is illustrated in Fig. 4.5. Fig. 4.5(a) shows the simulated reflection spectrum

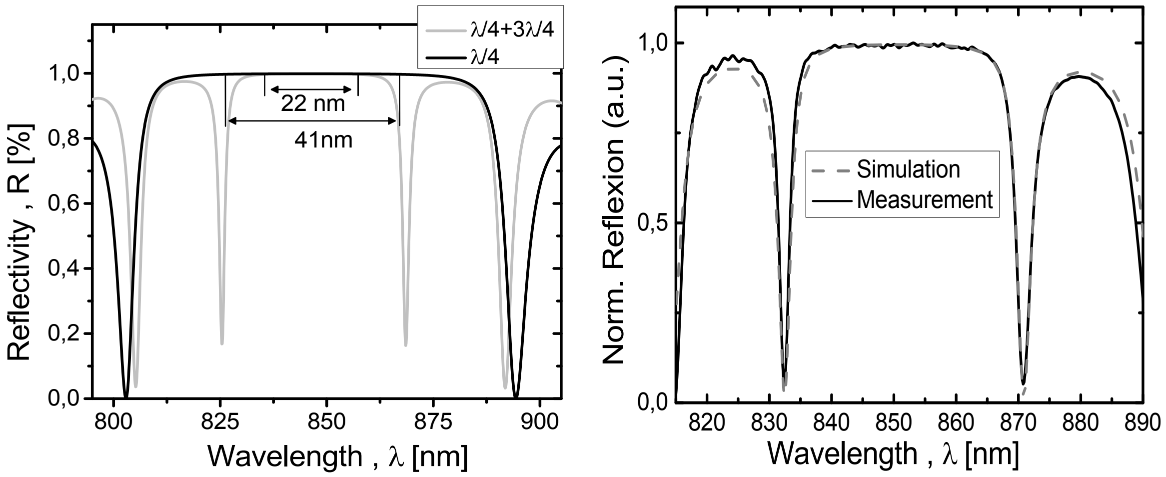

(a) (b)

Figure 4.5.: (a) Simulated reflection spectrum of two semiconductor DBRs. One of them with 22.5 pairs of $\lambda/4$ pairs and the other one with 22.5 pairs of combination of $\lambda/4$ and $3\lambda/4$ pairs. The 99.7% stop bandwidth of both DBRs is illustrated. (b) Simulated reflection spectrum and the measured spectrum of a semiconductor DBR with 22.5 pairs of $\lambda/4$ and $3\lambda/4$-thick layers.

of two semiconductor DBRs. The stop bandwidth of the DBRs has been defined by 99.7 $\%$ reflection. It can be seen that the introduction of $3\lambda/4$ pairs reduces the stop bandwidth of the mirror from 41 nm to 22 nm.

The semiconductor DBRs in this work are grown by Walter-Schottky institute of TU-Munich and are further processed in TU-Darmstadt. The thickness of the layers is controlled by in-situ measurement during the growth, which provides a very high accuracy. In this method the black body radiation of the heated substrate interferes with the growing layer, which results in oscillations of temperature. These oscillations are monitored by a pyrometer. The oscillation frequency is correlated with the growth rate, which means that after the growth of the layer, the thickness can be measured. With this technique the average deviation of the center DBR wavelength between simulation and growth could be reduced to below 1 $\%$.

Fig. 4.5(b) shows the simulated and the measured reflection spectrum of a semiconductor DBR with 22.5 pairs and a thickness of $3\lambda/4$. The measurement of the central DBR wavelength and the reflection has been done with Bruker Vertex 70 FTIR spectrometer equipped with an extended InGaAs detector at the Walter-Schottky institute of TU-Munich.

In order to influence the deflection direction of the membrane after resolving from the substrate (Sec. 4.2.2) and adjusting the air-gap and RoC, a stress gradient has been implemented inside the DBR layers. The lattice constants of the high-index and the low-index first AlGaAs layers without indium are 5.6543 $\AA$ and 5.6599 $\AA$ respectively. Compared to the lattice constant of the GaAs-substrate (5.6533 $\AA$), the DBR layers have a compressive stress and will expand after removing from the substrate.

However the lattice constant difference in AlGaAs layers is not sufficient to introduce a significant air-gap and curvature in the mirror. Fig. 4.6 shows the confocal microscope image of such a membrane after processing including just high- and low-index layers according to App. C, table C.3. As it can be seen, the resulting membrane does not show any significant air-gap or curvature in the mirror compared to the one in Fig. 4.1(b).

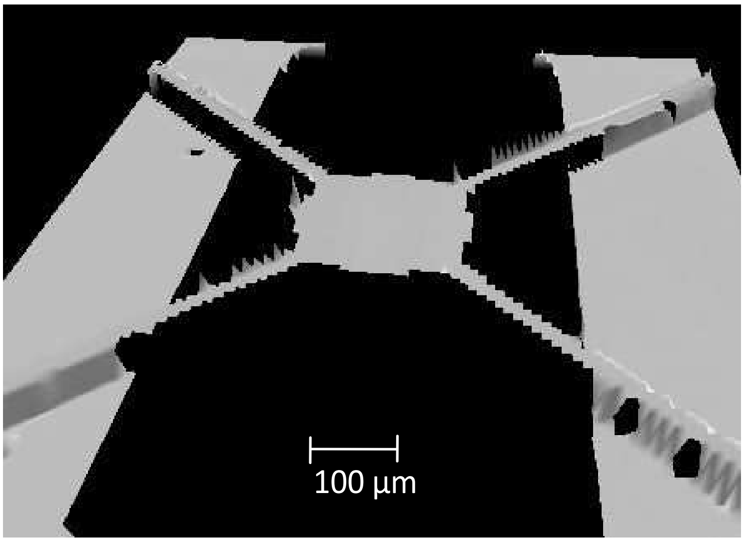

Figure 4.6.: Three dimensional (turned up) confocal microscope image of a membrane without any Indium in DBR layers.

To solve this problem a stress gradient has to be introduced into the DBR. This has been achieved by adding Indium (max. 2.5 $\%$) in the upper layers close to the GaAs-substrate (App. C, table C.1 and table C.2). The indium atoms replace the gallium atoms in high index AlGa(In)As layers and thus increase the lattice constant of the crystal (5.6646 $\AA$ for 2.5 $\%$ Indium). This introduces a stress gradient and a higher compressive stress between the layers, which means after removing from the substrate those layers will expand stronger, resulting in a significant air-gap and curvature. The tables in App. C include the calculated stress of the layers in MPa (mega Pascal) for semiconductor DBRs according to:

$$P = E_{\text{Young}} \frac{l_{\text{layer}} - l_{\text{substrate}}}{l_{\text{layer}}} \tag{4.1}$$

E_{Young} is the Young modulus and l_{layer} and $l_{\text{substrate}}$ are the lattice constants of the layer and the substrate, respectively.

The upper layers in semiconductor DBRs are highly n-doped with Si (App. C, table C.2, table C.1 and table C.3). This causes the current flow through the membrane and thus the electro thermal tuning of the membrane.

To be able to etch the substrate from the DBR selectively, a low-index AlGaAs layer with a thickness of 300 nm has been implemented between the DBR and the substrate. This layer is called etching stop layer and should be removed after removing the substrate. The thickness of the etching stop layer is chosen experimentally depending on the processing environment.

4.2.2. Fabrication

After deposition of the semiconductor DBR on a 2 inch GaAs-substrate with the substrate thickness of 350 μm, the fabrication of the membrane begins as follows ([61], [25], [20]):

1. Substrate thinning to 150 μm with a chemical -mechanical polishing method. After polishing the 2-inch wafer is cut to smaller pieces suitable for further processing.

2. Definition of the transmission line trenches on the DBR by means of photo lithography and wet etching (HCl:H_2O) (1:10). In these trenches the non-highly n-doped layers have been removed. The trench avoids the direct contact between the frame and the transmission line but does not disturb the current flow through the membrane (Fig. 4.7).

3. Definition of the front shape of the membrane on the DBR by means of photo lithography and wet etching with (H_3PO_4:H_2O_2:H_2O) (1:1:4). A current separation is introduced to the frame to separate two electrodes for current tuning (Fig. 4.7).

4. Removing the substrate behind the mirror and releasing the membrane by photo lithography and wet spray etching from the back side. The first step is a fast etching by (H_2O_2:NH_3OH) (10:1). The solvent has a fast etching rate but is low selective against the etching stop layer. The second step is a slow etching by (H_2O_2:NH_3OH) (100:2). This solution has a slow rate but is highly selective against the etching stop layer. These two steps have been done with a spray-etching system. The last step is then removing the etching stop layer by (HCl:H_2O) (1:3). At the same time two small holes are etched for electrical via-hole contacting. The tuning current will flow through these contacts from the back side into the high n-doped DBR layers (Fig. 4.8).

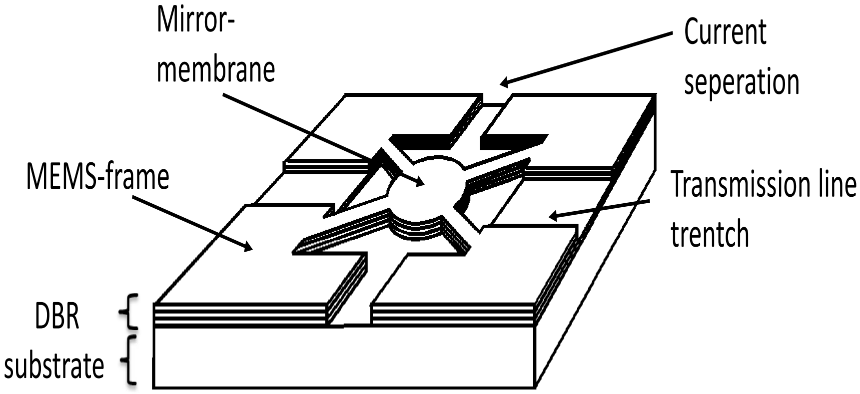

Figure 4.7.: Front side of the fabricated semiconductor membrane.

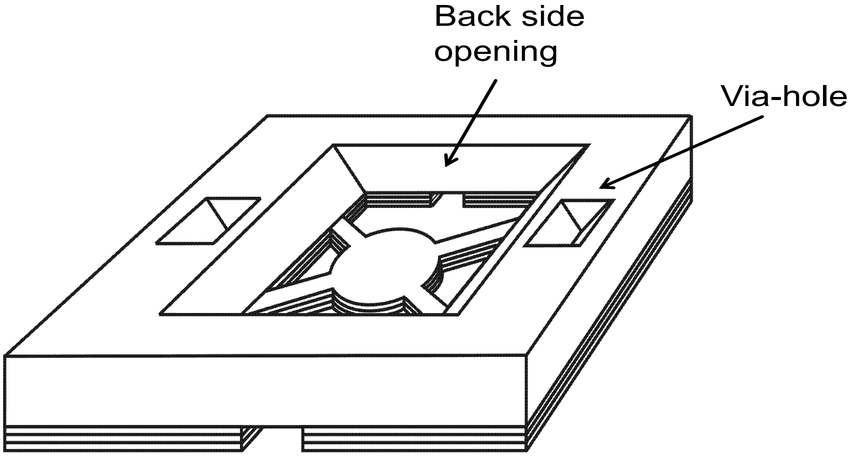

Figure 4.8.: Back side of the fabricated semiconductor membrane.

5. The last step is the metallization of the via-holes (Fig. 4.9). The metallization is done by depositing a Ni-Au-Ni-layer in these holes. To make an ohmic contact between the deposited metal and the membrane semiconductor layers, a rapid thermal annealing (RTA) process by 450^oC is carried out (Fig. 4.9).

In order to ease the connection of the tuning electrodes with the membrane and in the same time to protect the via holes from the mechanical damage, the via-holes are covered by a conductive silver glue.

Besides the number of the layers, the thickness of the layers and the amount of the stress in the layers, which are responsible for the deflection of the membrane, the geometry of the membrane is very essential to set the desired air-gap and RoC. Table 4.1 shows how the variation of the geometric parameters of the membrane such as beam length, beam width and membrane diameter can influence the air-gap and RoC. The parameters of the fabricated membranes are given in App. C, table C.1. The air-gap and RoC are measured by a confocal microscope.

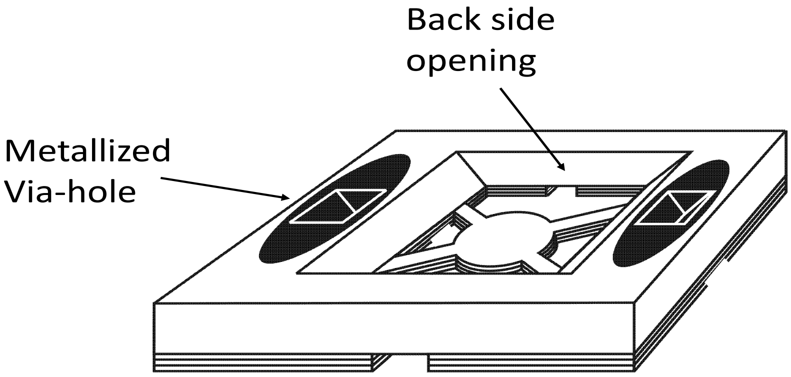

Figure 4.9.: Back side of the fabricated semiconductor membrane with metallized via-holes.

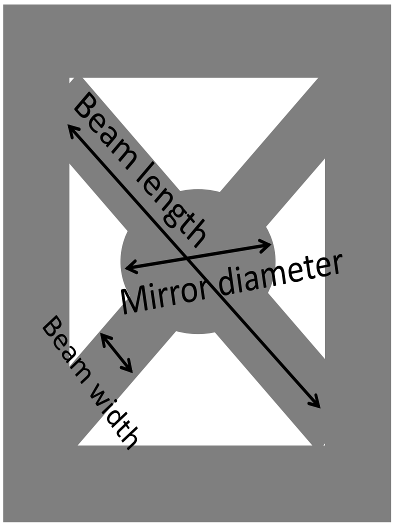

Membrane	Mirror diameter [um]	Beam width[um]	Beam length [um]	RoC [mm]	Air -gap[um]
A	200	70	565	3.2	9.6
B	200	70	480	3.2	8.5
C	200	70	325	2.9	5.5
D	150	70	254	2.5	2
E	100	50	197	2	0.4

Table 4.1.: Different geometry parameters of the membrane result in different air-gaps and RoCs.

4.3. Hybrid Membrane

The hybrid membrane is a DBR made of semiconductor and dielectric layers. The dielectric layers provide the high stop-bandwidth of the mirror and the semiconductor layers act for current transport. In the following the design and the fabrication of these membranes are introduced. The test of the hybrid membrane on the half-VCSEL is not included in this work due to the limited number of available half-VCSELs.

4.3.1. Structure and Design

The semiconductor part of the hybrid membrane is made of 4.5 pairs of alternating high- and low-index AlGa(In)As layers grown by MBE on undoped GaAs substrate in the Walter-Schottky Institute of TU Munich (App. C, table C.4). The maximum indium content of the high-index layers is 3 $\%$, which is equivalent to a compressive stress of about 200 MPa. After depositing the semiconductor layers, the dielectric layers are deposited by a low temperature PECVD at the TU Darmstadt [62].

The first deposited dielectric layer is a $\lambda/2$-thick SiO_2 layer that acts as a cleaving layer between the semiconductor and the dielectric layers. After that, 8 pairs of alternating SiO_2 and Si_3N_4 layers with the thickness of $\lambda/4$ are deposited. The Si_3N_4 layers have a compressive stress of 70 MPa and the SiO_2 layers have a tensile stress of -120 MPa. The stress amount in dielectric layers is measured from the deposited test layers on the GaAs substrate by using a surface contact measurement technique (Dektak-profilometer).

The total thickness of the DBR layers is 4987 nm. If we take the cleaving layer and etching stop layer into the account, the total thickness is 5290 nm. The designed hybrid membrane described above has a maximum reflectivity of 99.89 $\%$ at the central wavelength of 850 nm. The stop bandwidth of the DBR, defined by the minimum reflectivity of 99.7 $\%$ is 78 nm, as is shown in Fig. 4.10. Comparing the stop bandwidth of the hybrid DBR with the semiconductor DBRs clarifies the impact of using the dielectric layers: by applying the hybrid membrane the bandwidth of the membrane is increased about 37 nm.

The PECVD machine available at the TU Darmstadt did not have an in-situ thickness control. Therefore, a variation of the central wavelength is possible. The thickness and the refractive indices of the layers are controlled by the test depositions of the single layers by using a reflectometer before the deposition of the dielectric layers of DBR.

Fig. 4.10 shows the simulated reflection spectrum and the measured spectrum of the hybrid membrane. The spectrum has been measured by illuminating a white light source on the mirror and measuring the spectrum of the reflected light using an optical spectrum analyzer (OSA). The figure shows a mismatch of about 20 nm in the central wavelength between the simulation and the measurement due to the thickness variation of the dielectric layers during the deposition. Although the designed center wavelength was 850 nm, the achieved one is about 830 nm.

4.3.2. Fabrication

After deposition of the semiconductor and the dielectric layers on a 350 μm thick GaAs substrate, the processing of the membrane was performed. The fabrication of the membrane from

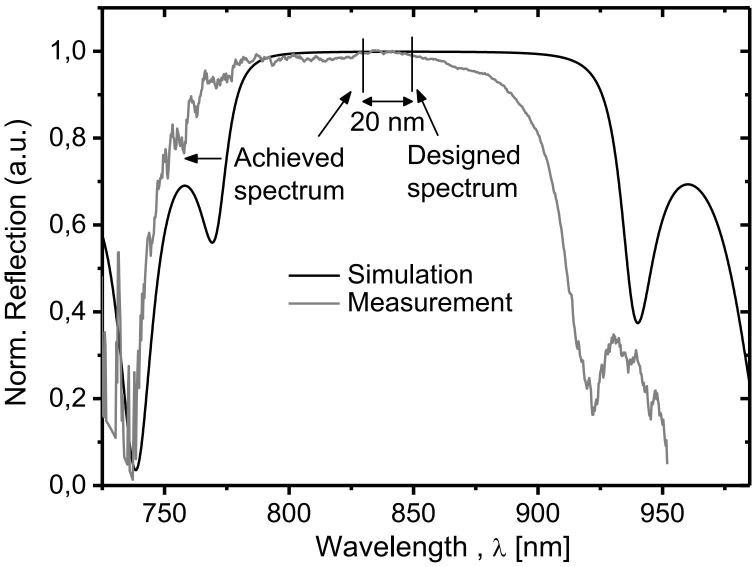

Figure 4.10.: Simulated and measured reflection spectrum of hybrid DBR. A mismatch of 20 nm in central wavelength is appeared due to the variation of the thickness of layers in dielectric part.

the wafer is very similar to that of the semiconductor DBRs but, it has some additional steps as explained in the following:

1. Substrate thinning to 150 μm with a chemical -mechanical polishing method. Thereafter the 2 inch wafer is cut into smaller pieces suitable for further processing.
2. Covering the whole sample by a 500-nm-thick nickel layer with a sputter machine. This layer acts as an etching mask to etch the dielectric layers.
3. Definition of the front shape of the membrane on the nickel etching mask by means of photo lithography and wet etching (HNO_3:H_2O) (1:20).
4. Dry etching of the dielectric layers with the SF_6-plasma in a reactive ion etching- (RIE)-machine.
5. Wet etching of the semiconductor layers and introducing the current separation by (H_3PO_4:H_2O_2:H_2O) (1:1:4).
6. Removing the rest of the nickel etching mask by wet etching (HNO_3:H_2O) (1:20). The front side of the membrane in this step is shown in Fig. 4.11.
7. Removing the substrate behind the mirror and releasing the membrane by photo lithography and wet etching from the back side. The first step is a fast etching by (H_2O_2:NH_3OH) (10:1). The second step is (H_2O_2:NH_3OH) (100:2). These two steps are done with a spray-etch system. The last step is then the removing of the etching stop layer by (HCl:H_2O) (1:3). At the same time the via-holes have been etched into the substrate too (Fig. 4.8).

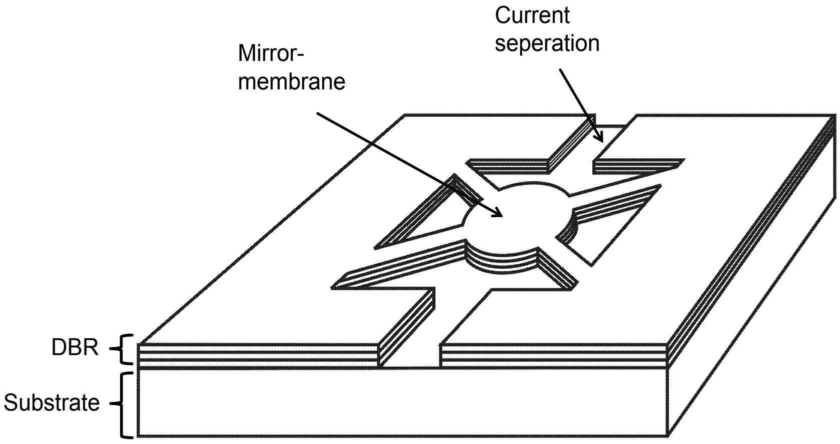

Figure 4.11.: Front side of the fabricated hybrid membrane.

8. The last step is the metallization of the via-holes by depositing a Ni-Au-Ni-layer in these holes. To make an ohmic contact between the deposited metal and the membrane semiconductor layers, a RTA process by 450^{o}C is carried out (Fig. 4.9).

Due to the fabrication complexity of the hybrid membrane, the transmission line trenches are not implemented any more.

4.4. Dielectric Membrane

A dielectric membrane is a DBR just made of dielectric layers. The dielectric layers provide a very large stop-bandwidth of the mirror. Due to the fact that the dielectric layers are non conductive, an additional metallization has to be implemented on the top of the DBR to support the current flow and the electro thermal tuning. In the following the design and the fabrication of the dielectric membranes are discussed.

4.4.1. Structure and Design

The dielectric membrane in this work consists of 12.5 alternating pairs of SiO_2 and Si_3N_4 with the optical thickness of $\lambda/4$, as shown in App. C, Table C.5. These layers are deposited by a low temperature PECVD. The designed central wavelength is 850 nm.

The SiO_2 layers have a constant compressive stress of 100 MPa, while the first six layers of Si_3N_4 have a compressive stress of 250 MPa and the rest of six Si_3N_4 layers have a tensile stress of -75 MPa. This stress gradient together with the geometry of the membrane results into the desired air-gap and curvature.

The maximum reflectivity of this dielectric mirror is 99.9 $\%$ at the central wavelength of 850 nm and the 99.7 $\%$-reflectivity stop-bandwidth is 97 nm, as shown in Fig. 4.12. Comparison of Fig. 4.12 to the Fig. 4.5(a) and Fig. 4.10 shows that the smaller reflective indices of dielectric layers and larger reflective indices difference between dielectric layers provide the largest reflectivity stop-bandwidth among the introduced DBRs.

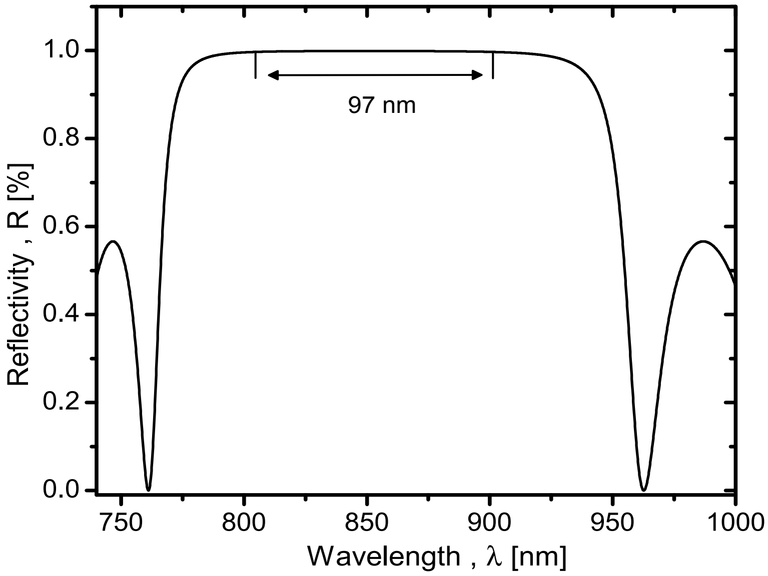

Figure 4.12.: Simulated reflection spectrum of the dielectric DBR with 12.5 pairs and center wavelength of 850 nm.

Due to the absence of the in-situ measurement during the deposition of the layers in PECVD a variation of about 20 nm in the central wavelength is expected.

4.4.2. Fabrication

The dielectric membrane has been designed and fabricated at the TU Darmstadt. Fig. 4.13(a) shows the half-VCSEL chip without the top dielectric membrane. As has been already noticed in Sec. 4.1, the fabrication of the tunable VCSELs with the dielectric DBR is done by applying the surface micromachining technology. This method is based on using a sacrificial layer and depositing and processing the whole membrane directly on the half-VCSEL chip, as it is described in the following steps.

1. Covering of the whole half-VCSEL chip with a 300-nm-thick layer of sputtered nickel. After structuring this layer by means of photo lithography and wet etching (HNO_3:H_2O) (1:20), it acts as the sacrificial layer for the deposited DBR and protects the transmission lines against etching during the fabrication. Fig. 4.13(b) shows the structured sacrificial layer on the half-VCSEL.

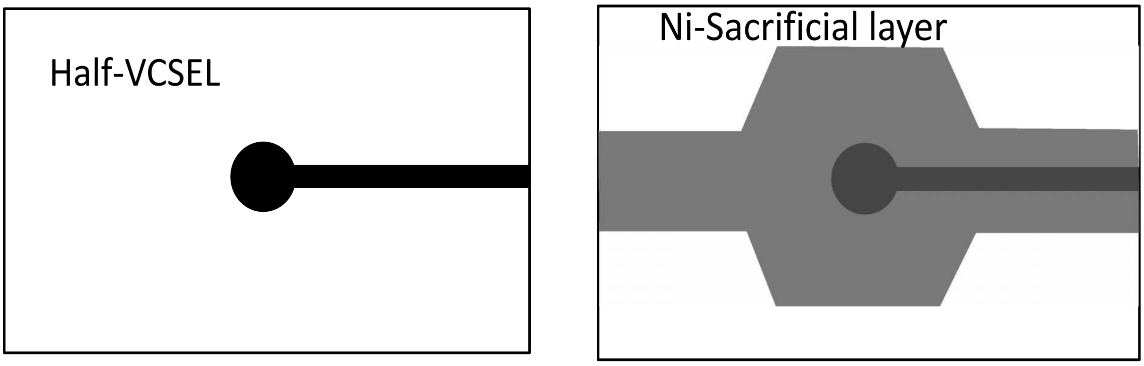

(a) (b)

Figure 4.13.: Processing steps to deploy the dielectric DBR on the half-VCSEL: (a) Half-VCSEL chip before starting the processing. (b) After deposition and structuring of the sacrificial layer.

2. Deposition of the whole DBR on the chip using PECVD (Fig. 4.14(a)).
3. Introduction of the negative photo mask for the lift-off process.
4. Evaporation of 40-nm-thick Cr/Au-metallization on the chip. This layer acts for the current transport through the membrane and electro thermal actuation.
5. Applying an opening in the metallization by means of the lift-off process (Fig. 4.14(b)). The illuminated light from the VCSEL leaves the device from this opening.
6. Covering the whole sample with a 500-nm-thick layer of sputtered nickel. This layer acts as a etching mask to etch the dielectric layers.
7. Structuring the membrane on the nickel etching mask by means of photo lithography (Fig. 4.15(a)) and wet etching (HNO_3:H_2O) (1:20).

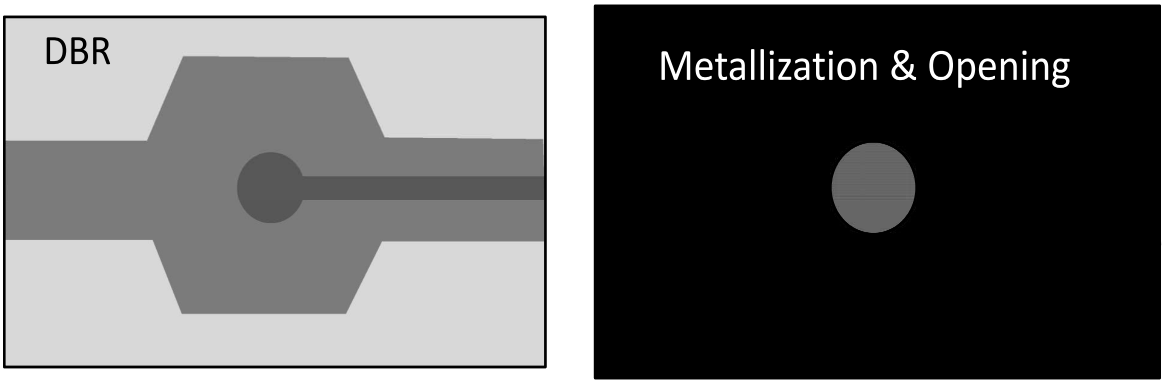

(a) (b)

Figure 4.14.: Processing steps to deploy the dielectric DBR on the half-VCSEL: (a) After the depositing the DBR. (b) After the metallization and the introduction of the membrane opening for lasing.

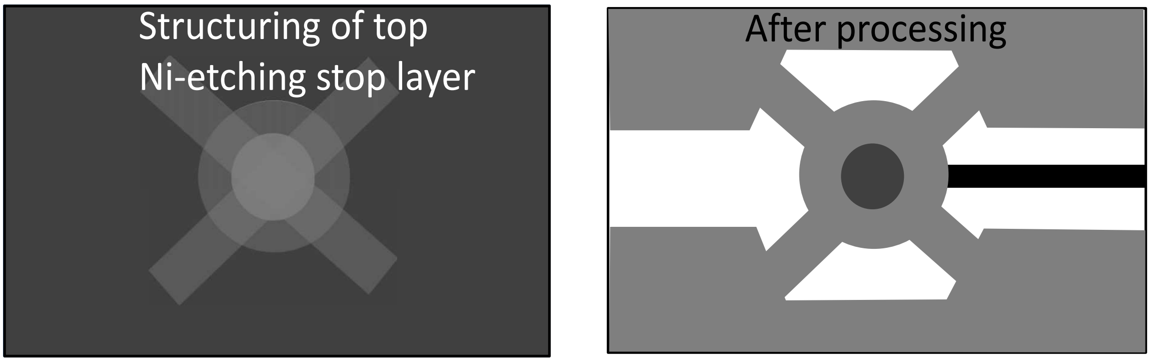

(a) (b)

Figure 4.15.: Processing steps to deploy the dielectric DBR on the half-VCSEL: (a) After the depositing of the top etching stop Ni-layer and the structuring the photo resist on it. (b) Deposited membrane after etching the layers and finishing the processing.

8. Wet etching of the gold (J_2:KJ:H_2O) (1g:4g:40ml) and chromium ($(NH_4)_2Ce(NO_3)_6$: HNO_3:H_2O) (82g:45ml:500ml).

9. Dry etching of the dielectric layers with SF_6-plasma in a RIE-machine.

10. Removing of the rest of the nickel etching mask and the nickel sacrificial layer by the wet etching (HNO_3:H_2O) (1:20) (Fig. 4.15(b)).

Fig. 4.16(a) shows a microscope image of the half-VCSEL after the depositing and the structuring of the sacrificial layer. Fig. 4.16(b) shows a microscope image of the whole device after processing. After the removing of the sacrificial layer, the mirror will deflect due to the embedded stress in the layers. The deflection causes the air-gap and the RoC of the membrane.

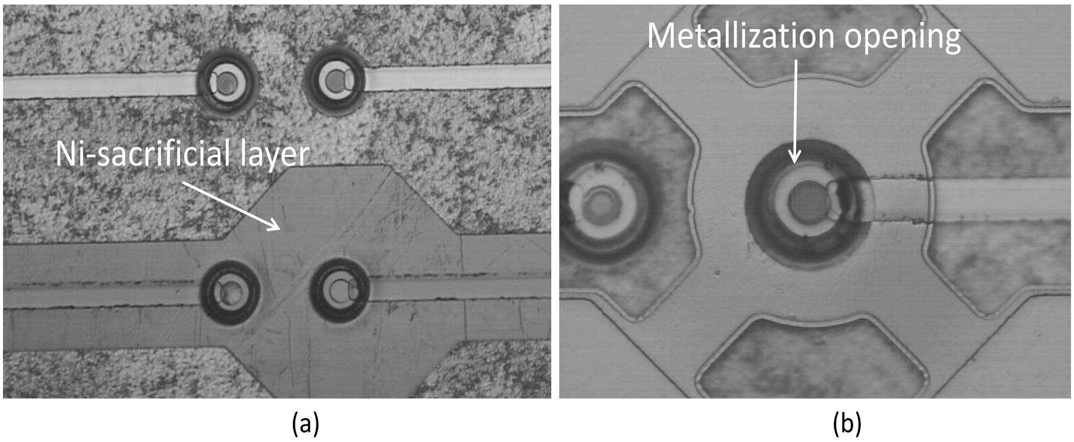

Figure 4.16.: (a) Ni- sacrificial layer on the half-VCSEL. (b) The whole membrane on the half-VCSEL after finishing the fabrication

4.5. Modeling of Tunable VCSEL

The tuning properties of the VCSEL can be modeled by means of one-dimensional transfer-matrix simulations. One can distinguish three basic designs for the micro-machined tunable cavities, each differing only in the reflection properties of the semiconductor-air interface of the half-VCSEL [64] [7]. These three designs are:

1. **Resonant design**
   In this configuration the optical field has a maximum (anti-node) at the semiconductor-air interface and the reflectivity of the external mirror is effectively enhanced at the design (i. e. center) wavelength. Tuning away from the center wavelength degrades the effective reflectivity and thus, it decreases the threshold gain and limits the tuning range.

2. **Non-resonant design**
   In this configuration the optical field has a minimum (node) at the semiconductor-air interface and the effective reflectivity of the external mirror is reduced at the design (i.e. center) wavelength. But detuning away from the center wavelength enhances the effective reflectivity and thus, it compensates the losses and potentially enables a wider tuning range. The threshold gain is larger in this case.

3. **Extended cavity design**
   As a trade-off between the above configurations an anti-reflection (AR) coating is applied on the half-VCSEL, which, compared to the non-resonant design, affectively enhances the reflectivity and reduces the threshold gain.

To investigate the high-speed properties of the transmission lines and their interaction with the membrane, three dimensional microwave simulations are carried out with the simulation tool CST (computer simulation technology). The simulation results are presented at the end of this section.

4.5.1. VCSEL without SWG

The structure of the half-VCSEL that is used for simulations for the device without SWG has been introduced in Sec. 3.1 and is shown in App. B. The simulations in this section have been done at the University of Turino. A semiconductor mirror (App. C table C.3) is used as the external mirror for simulations. Fig. 4.17 shows the simulated resonance wavelength for the three basic designs of a micromachined tunable cavity.

The characteristics in Fig. 4.17 are non-linear for the resonant and the non-resonant cases as an effect of the coupled cavities, while the characteristic of the extended cavity is linear. The tuning efficiency, i.e. the change in the wavelength per change in the air-gap, is the lowest for the resonant design and the highest for the non-resonant design.

Fig. 4.18 shows the simulated threshold gain over the wavelength for the three configurations above. The figure shows that the non-resonant design compared to the other designs has a small variation in the threshold gain during the tuning, however a much higher material gain needs to be provided. Finally the tuning range is limited by FSR. The threshold gain of the non-resonant

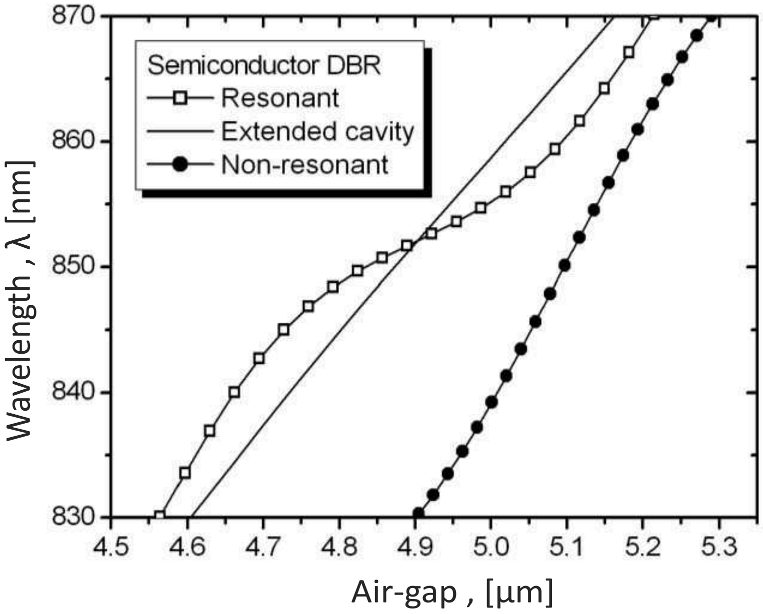

Figure 4.17.: Simulated resonance wavelength for micromachined air-gap cavities in the three configurations.

design can be significantly reduced with an AR coating (Fig. 4.18). In fact, this extra layer enhances the intensity in the half-VCSEL and thus enhances the longitudinal confinement and the modal gain, respectively.

Fig. 4.19 shows the refractive index profile and the simulated field intensity ($|E^2|$) for a VCSEL (resonant design) with and without the AR-coating. The external mirror is a dielectric DBR (Sec. 4.4.1). As can be seen in Fig. 4.19(a), the intensity in the half-VCSEL with the AR-coating is increased compared to the one without the AR-coating (Fig. 4.19(b)) thus the requirement on high gain is decreased.

In order to achieve a large tuning range with a small threshold gain, the extended cavity design is chosen for all the VCSELs in this work.

4.5.2. VCSEL with SWG

The one-dimensional cold cavity simulations and the polarization selectivity for the fundamental mode are calculated using the transfer-matrix method. The simulations here are for the case that the grating has been implemented on the surface of the half-VCSEL without AR-coating, as introduced in Sec. 3.3. The simulations in this section have been done at the University of Turin. The external mirrors used in the simulations are hybrid DBRs (Sec. 4.3.1)

There are several design parameters, which have a significant influence on the impact of grating. They are:

1. Thickness of the top p-contact layer (Fig. 3.2).
2. Grating period (Sec. 3.3).
3. Etch depth (Sec. 3.3).

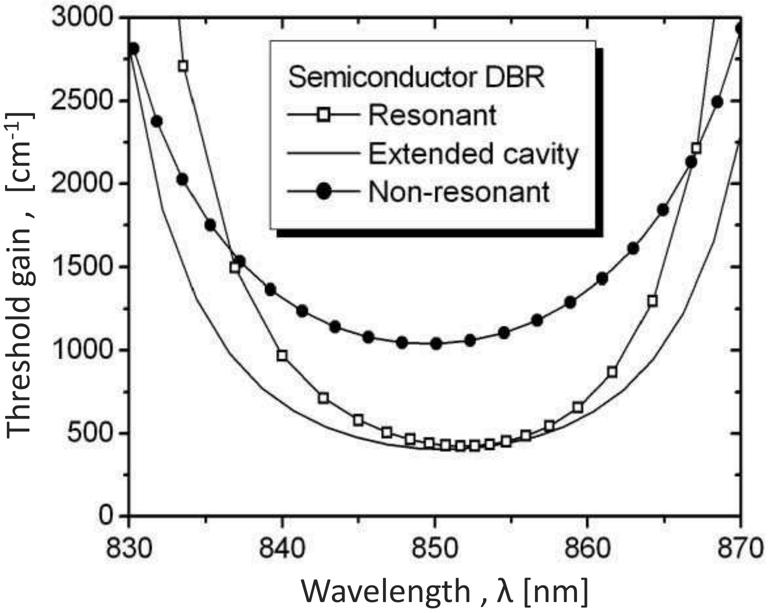

Figure 4.18.: Simulated threshold gain for the tunable VCSEL with a semiconductor DBR.

4. Duty cycle ($d_1/(d_1 + d_2)$) from Fig. (3.4)).

The effects of the partly etched p-contact layer on the threshold characteristics of the tunable VCSELs for a contact layer thickness of 10 nm, 20 nm and 30 nm are shown in Fig. 4.20(a). The simulations have been done for the case of a fixed SWG period of 200 nm, duty cycle of 20 $\%$ and the etch depth of 42.4 nm. The figure shows that the device with 10 nm p-contact layer has the lowest threshold gain of around 860 cm^{-1}. In order to make VCSELs with a low threshold, the required gain should not exceed 1000 cm^{-1} (dashed line).

The dependency of the threshold gain on the grating period is shown in Fig. 4.20(b). The simulations are carried out for the different grating values of 200 nm, 160 nm and 120 nm. The fixed parameters are the 10 nm contact layer, the 20 $\%$ duty cycle and the etch depth of 42.4 nm. As can be seen in the figure, the threshold gains of the two polarization modes (dots, line) are similar for all periods. Of course, larger periods are easier to fabricate, especially when it comes to the small duty cycles.

The impact of changing the duty cycle on the threshold gain of the two polarization modes is shown in Fig. 4.21(a). The absorption in the contact layer and thus the threshold gain are minimized for the small duty cycles, whereas the gain difference between the two polarization modes is nearly identical for all the three cases in Fig. 4.21(a).

The etch depth is investigated as the last parameter. Fig. 4.21(b) shows the simulation results for different etch depths of the sub-wavelength grating. The contact layer in these simulations is 10 nm thick, the period is 200 nm and the duty cycle is 20 $\%$. The number in the brackets correspondents to the number of etched layers in the basic material. A deeper etching lowers the threshold gain but at the same time reduces the tuning range.

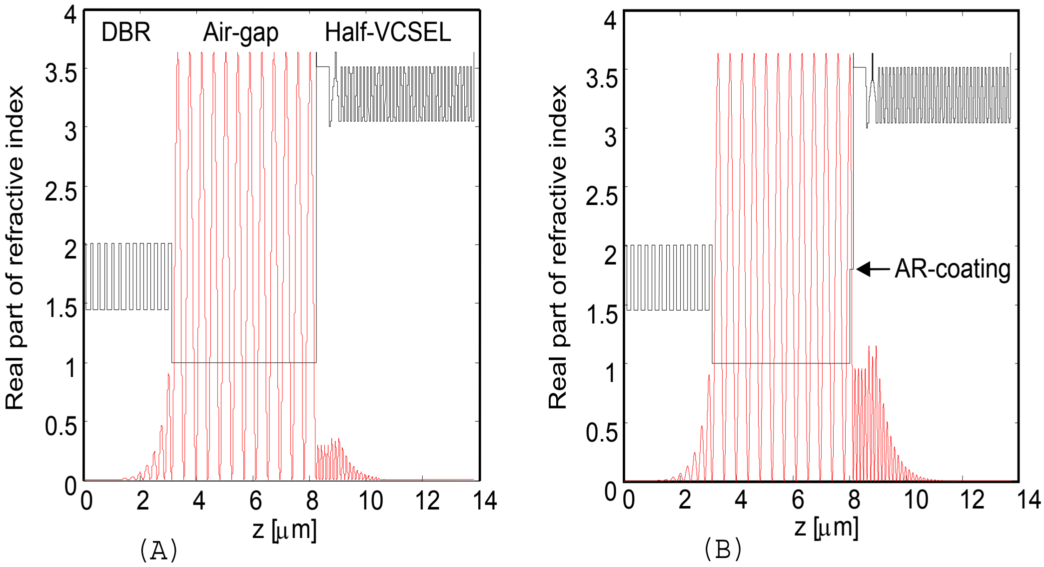

Figure 4.19.: Refractive index profile (dark) and simulated field intensity in arbitrary units (red) for a VCSEL without the AR-coating (A) and with the AR-coating (B).

4.5.3. Transmission Lines

The field propagation on the transmission lines can be influenced by the environment such as the movable membrane and its frame. It may interact with the membrane thus the modulation bandwidth decreases. The simulations in this section have been done at the TU Darmstadt. Fig. 4.22(a) shows the electromagnetic simulation model for simulating the transmission line with and without a mirror on it. The simulated mirror contains a round membrane above the transmission line with its frame. The membrane has a distance of about 6 μm from the line and its frame is directly placed on the line. The simulation results of the S_{11}- and S_{21}-parameters for the transmission line with and without the mirror are shown in Fig. 4.22(b). Comparing the two cases shows that the mirror, due to its conductive high-doped layers, influences the fields and degrades the transmission (S_{21}) and reflection (S_{11}) parameters.

To avoid the direct contact of the frame with the line, a trench with the depth of about 1 μm is implemented into the frame, as is shown in Fig. 4.23(a). The trench has significantly improved the transmission and reflection characteristics as can be seen in Fig. 4.23(b).

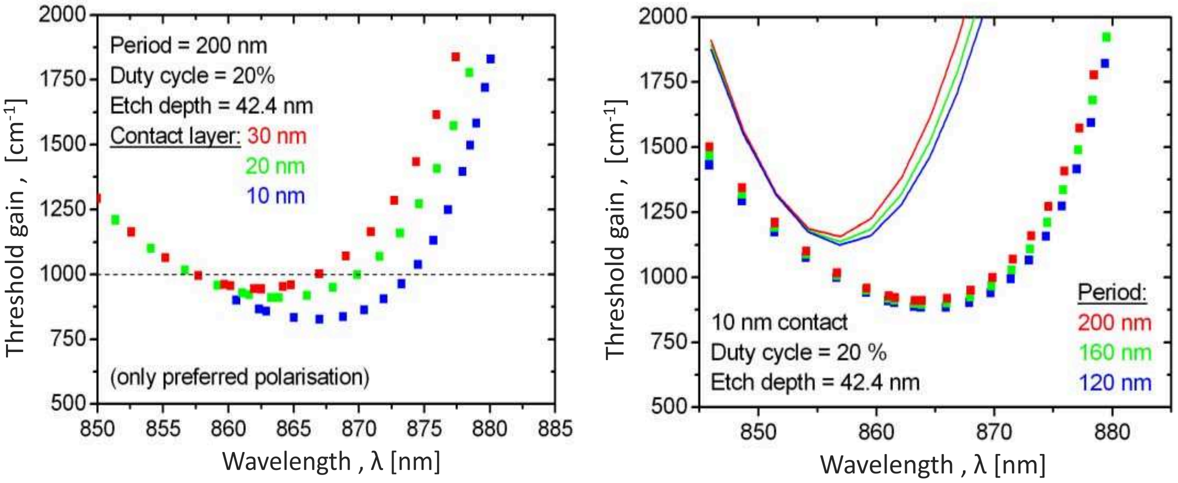

(a) (b)

Figure 4.20.: (a) Threshold gains for the preferential polarization modes for a top p-contact layer thickness of 10 nm, 20 nm and 30 nm respectively. (b) Influence of the grating period on the threshold gain of the two polarization modes (dots and line). The simulated periods are 200 nm, 160 nm and 120 nm.

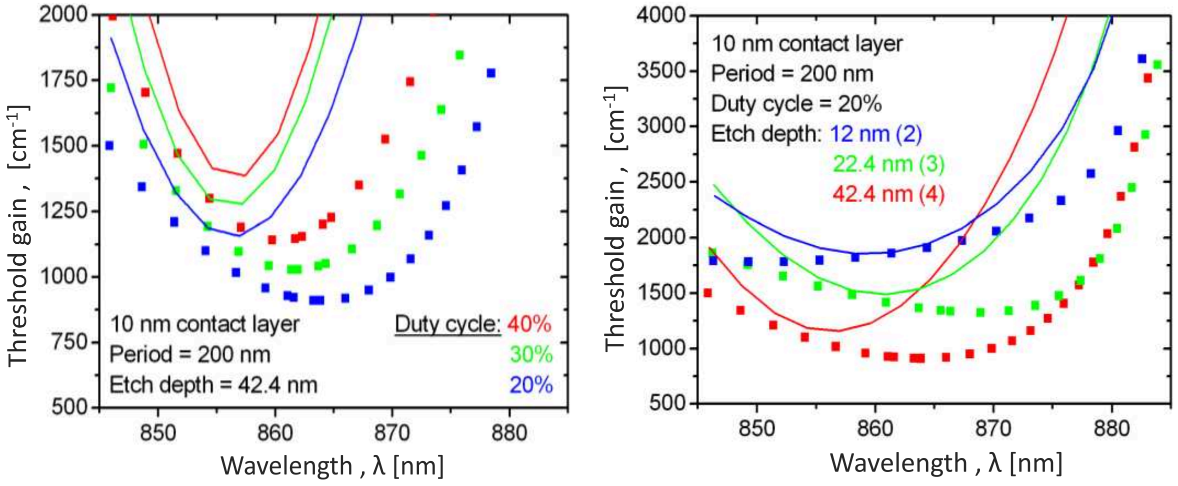

(a) (b)

Figure 4.21.: (a) Threshold gains of the two polarization modes (dots and lines) for duty cycles of 20 %, 30 % and 40 %. (b) Threshold gain of the two polarization modes (dots and lines) for the etch depth of 12 nm, 22.4 nm and 42.4nm.

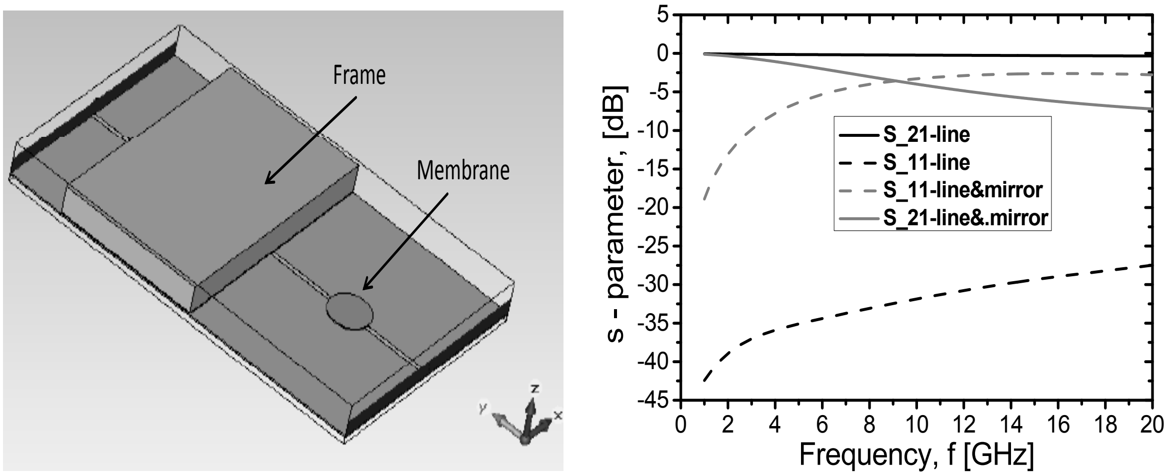

(a) (b)

Figure 4.22.: (a) Simulation model for the transmission line and the mirror on the top. (b) Simulation results including S_{11} and S_{21} for the cases with and without the mirror.

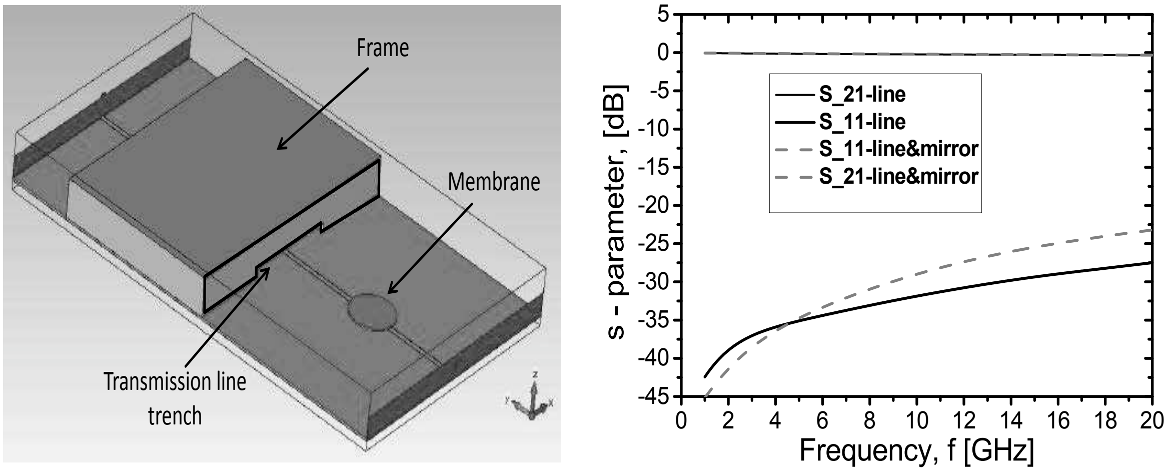

(a) (b)

Figure 4.23.: (a) Simulation model for the transmission line and the mirror (with the trench in frame) on the top. (b) Simulation results including S_{11} and S_{21} for the cases with and without the mirror.

5. Measurements

This chapter is about the characterization and verification of the devices introduced in the previous chapters by means of different types of measurements. These measurements are divided in two categories. The first category includes the static measurements of the PIV-characteristic, the tuning range, the tuning speed, the far field, the linewidth and the polarization. The second category includes the dynamic measurements of the small signal AM, the large signal AM and the RIN. In following sections the measurement setups are introduced and the results are presented and discussed. The characterized VCSELs in this chapter are listed in App. D

5.1. PIV-Measurement and Tuning Range

The PIV-measurement is about the measuring of the power-current-voltage characteristic of the VCSEL and determining the differential resistance and slope efficiency of the device. Tuning range-measurement determines the tuning range and the modal behavior such as the side-mode suppression ratio (SMSR) and the free spectral range (FSR) based on spectrum measurements.

5.1.1. Measurement Setup

The measurement setup for the PIV-measurement and the spectral measurement is shown in Fig. 5.1. In all measurements, the VCSEL is mounted on a thermoelectric cooler built on a peltier-element with a heat sink to stabilize the temperature at 20^oC. A thermo-resistor is applied to determine the operation temperature of the VCSEL. The cooler and the resistor are connected to a temperature control device, which reads the temperature via the resistor and sets the desired temperature by controlling the cooling power of the used peltier element.

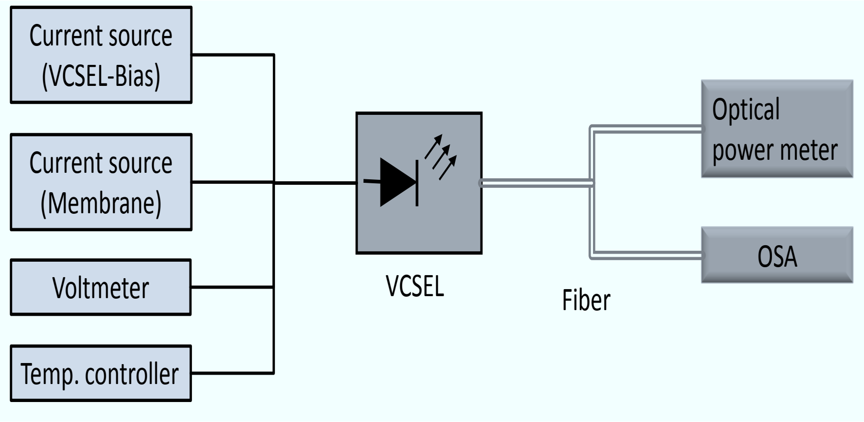

Figure 5.1.: Measurement setup for PIV-measurements and spectrum measurements.

A current source connected via the contact probes to the transmission lines of the VCSEL sets the bias current of the device. Another current source, which is connected to the membrane contacts, provides the tuning current for the membrane. A voltmeter with two inputs connected to the transmission lines and the membrane, respectively, measures the applied voltage on the VCSEL and the membrane.
The outcoming light from the VCSEL is coupled directly into the fiber, which is placed above the VCSEL. The fibre is connected to an optical power meter for the PIV-measurements or to an OSA for the spectrum measurement. The measurement devices are automatically connected by a computer via the general purpose interface bus (GPIB).

5.1.2. Measurement Results

This section is divided into three parts. The first part presents the measurement results for a bulk-micromachined VCSEL with a semiconductor membrane according to Table C.2 from App. C. The second part includes the measurement results of a bulk-micromachined VCSEL with a semiconductor membrane according to Table C.1 from App. C. The last part demonstrates the measurements on a surface-micromachined VCSEL according to Table C.5 from App. C.

Bulk-Micromachined VCSEL 1

The DBR used in this section is a semiconductor DBR with a stop bandwidth of about 22 nm (Table C.2 of App. C). Fig. 5.2(a) shows the spectrum of the VCSEL (VCSEL (A)) during the actuation of the membrane with a constant bias current of 8 mA through the VCSEL and a tuning current of maximum 12 mA [11]. The figure shows that a mode-hop-free continuous single-mode tuning of about 19 nm (from 840 nm to 859 nm) is achieved. The tuning range in

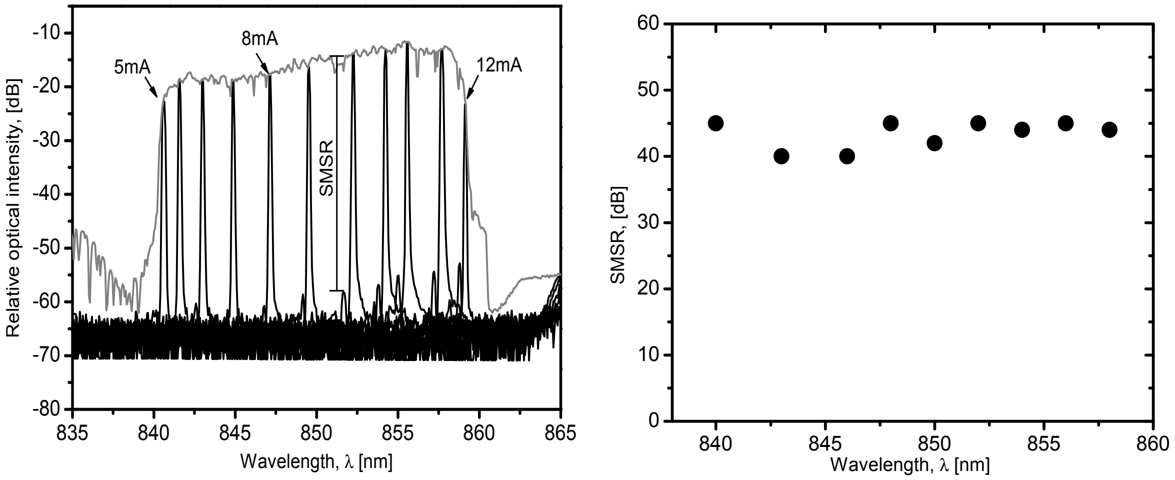

(a) (b)

Figure 5.2.: (a) Spectrum of the VCSEL (A) during the tuning for different tuning currents and a fix bias current of 8 mA. The envelope indicates the tuning range. (b) SMSR of the VCSEL (A) for different wavelength during the tuning.

this work is defined as the entire lasing range. The SMSR throughout the tuning range is shown in Fig. 5.2(b). The figure shows that the SMSR changes during the tuning between 40 dB and 45 dB.

The membrane in this device has an air-gap of about 2.8 μm and a RoC of 6 mm (App. D). The length of the cavity in the half-VCSEL is 0.8 μm with a refractive index of about 3.25. A penetration depth of about 5 μm is calculated for the semiconductor and dielectric mirrors. With these parameters a beam-waist of ω_0=6.35 μm can be calculated (Eq. 2.21). This beam-waist corresponds to a spot size of $2\omega_0$=12.7 μm. On the other side, the half-VCSEL in this device has an oxide aperture of about 13 μm, which is in the range of the spot size of the beam and it causes the single-mode operation.

To understand the limitation of the tuning range and the lasing area, the electroluminescence of the half-VCSEL is plotted versus the mirror stop-bandwidth (Fig. 5.3(a)). The electroluminescent is the spectrum of the VCSEL without the top mirror. It gives an idea about the gain of the VCSEL in combination with the bottom mirror. The maximum of electroluminescent is at 830 nm but the lasing and the tuning happen in the range of the stop-bandwidth of the membrane (from 840 nm to 859 nm) as shown in Fig. 5.3(a). That shows clearly that the limiting effect for the tuning range is the stop-bandwidth of the top mirror.

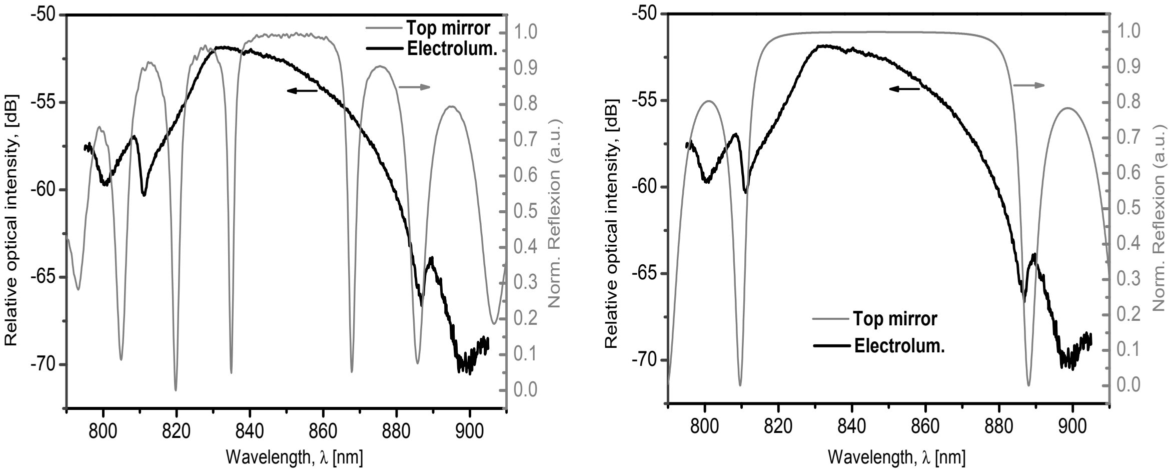

(a)

(b)

Figure 5.3.: Electroluminescent of the half-VCSEL (VCSEL (A)) vs. the stop-bandwidth of (a) the top membrane for a DBR with a small bandwidth (Table C.2 of App. C) and (b) a DBR with a large bandwidth (Table C.1 of App. C).

The PIV-characteristic of the VCSEL at the central wavelength of 850 nm is shown in Fig. 5.4(a). The threshold current of the VCSEL is 2.3 mA at 2.8 V and the thermal rollover is about 8 mA at 4.4 V. The maximum output power of the device at the central wavelength by the rollover is 0.17 mW or -7.5 dBm. The differential resistance of the VCSEL is shown in Fig. 5.4(b). The VCSEL shows a quiet high resistance between 300 Ω and 150 Ω.

The high serial resistance increases the device temperature and is one of the reasons that the thermal rollover appears at lower currents, thus the output power is small. To overcome this problem the thickness of the top p-contact layer in the half-VCSEL is increased from 3 nm to 10 nm to reduce the serial resistance. This measure decreases the serial resistance and enhances

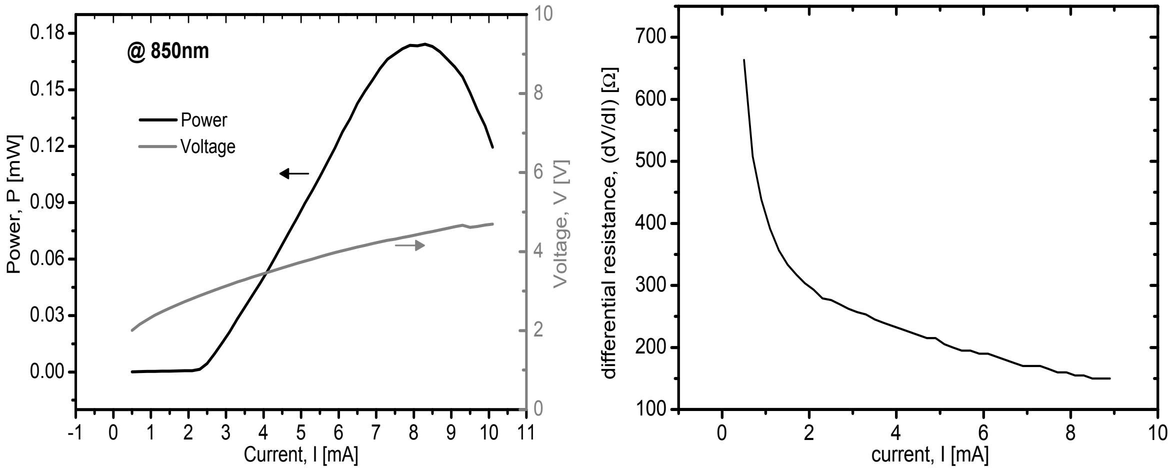

(a)

(b)

Figure 5.4.: (a) PIV-characteristic of the VCSEL (A) at 850 nm. (b) Differential resistance of the VCSEL (A) at 850 nm.

the output power of the VCSEL (VCSEL (B)). By detuning this VCSEL from the designed wavelength, due to the increase of the absorption loss and thus the threshold gain caused by thicker p-contact layer, the tuning range is limited to a maximum of 16 nm in this device. The improved PI-characteristic and the serial resistance of this device are shown in Fig. 5.5(a). As can be seen in Fig. 5.5(a), the increasing of the p-contact layer has increased the rollover current from 8 mA to 9 mA and thus the output power from 0.17 mW to 0.8 mW. The slope efficiency ($\delta P/\delta I$) is increased from 0.04 to 0.13. It should be taken into account that the power losses due to the membrane tilt or the coupling losses into the fiber may affect these results too.

Fig. 5.5(b) shows the differential resistance of the above two designs. The differential resistance of the device with a thicker p-contact is improved from the values between 300 Ω and 150 Ω to the values between 200 Ω and 100 Ω.

Bulk-Micromachined VCSEL 2

To increase the tuning bandwidth, a semiconductor DBR with a stop-bandwidth of about 41 nm (Table C.1 of App. C) is applied. The geometrical parameters of the membrane are the same as the membrane in VCSEL (A). Fig. 5.6(a) shows the tuning spectrum of the VCSEL for different tuning currents and a fixed laser bias of 5mA. The figure shows a mode-hop-free continuous single-mode tuning range of about 37 nm (from 827 nm to 864 nm). The SMSR throughout the tuning range is shown in Fig. 5.6(b). The SMSR varies between 30 dB and 45 dB during tuning.

Compared to Fig. 5.2(a), due to the increase of the stop bandwidth of the membrane, the tuning range is improved by about 18 nm (from 19 nm to 37 nm) and is in the range of the stop bandwidth of the mirror (Fig. 5.3(b)). The FSR of the device is 39 nm, which sets the ultimate limit for the tuning range (Fig. 5.6(a)). First of all, to increase the tuning range, the FSR should be increased by means of applying a shorter cavity length. That can be achieved by using membranes with shorter air-gaps or reducing the cavity length in the half-VCSEL. The

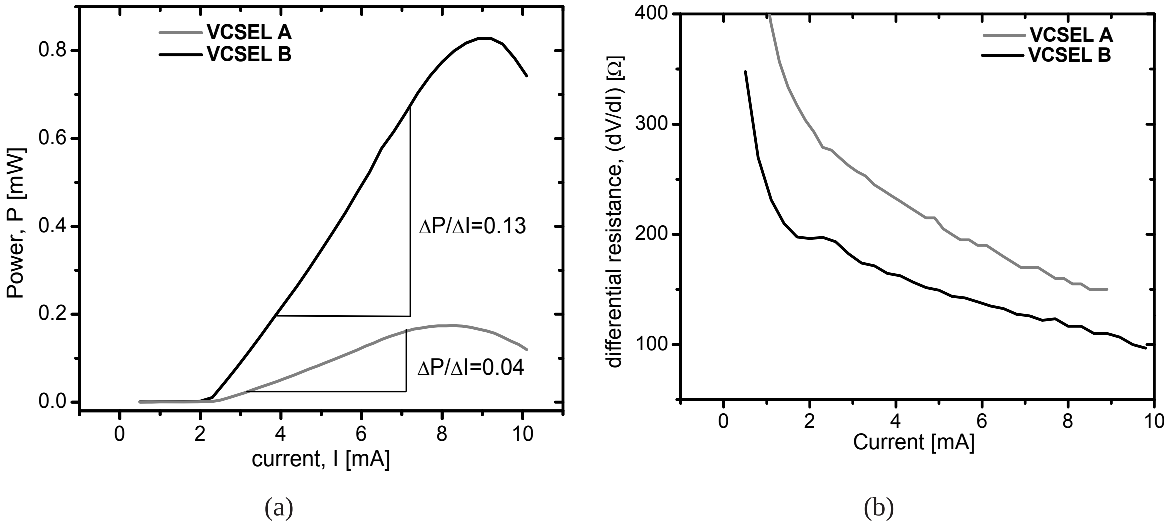

Figure 5.5.: (a) PI-characteristics of the VCSELs (A) and (B) at 850 nm for two different p-contact thickness. (b) Differential resistance of two VCSELs (A) and (B) at 850 nm for two different p-contact thickness.

next step is using the mirrors with larger stop-bandwidth such as dielectric mirrors.

If the spot-size of the beam is mismatched to the oxide aperture, or if the spot-size is smaller than the aperture, an unstable multi-mode behavior is observed. Fig. 5.7(a) shows the tuning characteristic of a VCSEL (VCSEL (D)) with an oxide aperture of about 16 μm and a calculated spot-size of about 12 μm [65]. The figure shows a total tuning range of 37 nm for a bias current of 7 mA. The used DBR is the same as the one used for the device with the tuning characteristic from Fig. 5.6(a).

This multi-mode behavior is caused by an device aperture larger than the spot-size (Fig. 5.7(a)). Fig. 5.7(b) shows the SMSR of the VCSEL during the tuning. The SMSR changes from -3 dB to about 40 dB during the tuning.

Surface-Micromachined VCSEL

As already described in the last chapter, the surface micromachining uses a dielectric DBR with a large stop-bandwidth. After the fabrication, the membrane has a RoC of 2 mm and an air-gap of 3.5 μm. The electrical resistance of the membrane is 19 Ω. Fig. 5.8(a) shows the tuning characteristic of the VCSEL (VCSEL (E)) with a bias current of 6 mA. The tuning begins at the wavelength of 861 nm and ends after 13 nm of continuous mode-hop-free single-mode tuning at 874 nm. The FSR of the VCSEL is 25 nm.

Although the dielectric DBR used for surface micromachining has a large stop-bandwidth of 97 nm and the FSR is much larger than the achieved tuning range, the tuning range of the VCSEL is limited to 13 nm. This limitation has two major reasons. The first one is a membrane tilt and the other is the influence of the fabrication steps of the mirror on the half-VCSEL and degradation of the half-VCSEL properties.

The SMSR of the VCSEL during the tuning is shown in Fig. 5.8(b). The figure shows that the

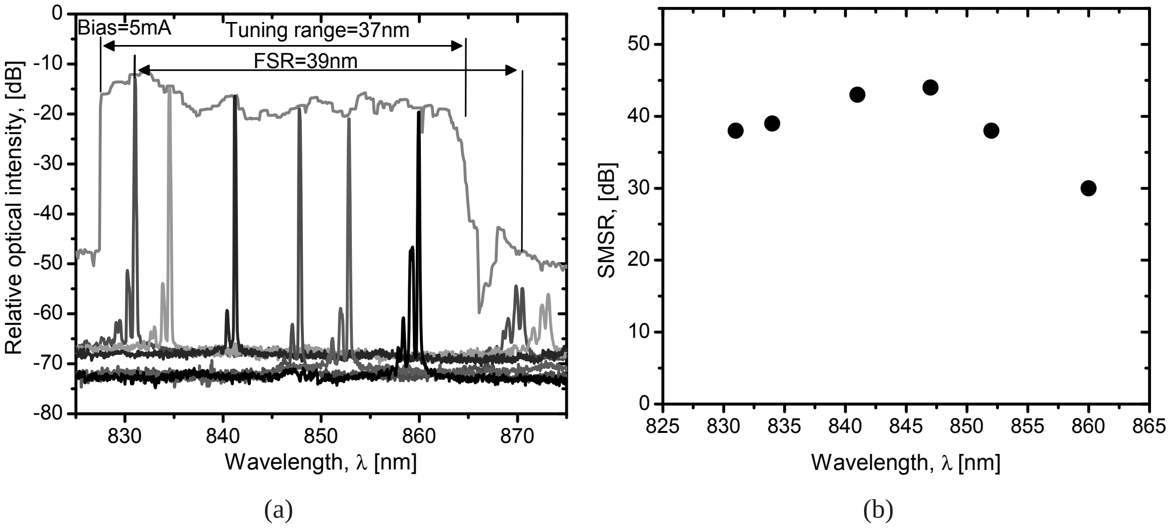

Figure 5.6.: (a) Spectrum of the VCSEL (C) during the tuning for different tuning currents and a fix bias current of 5 mA. The envelope indicates the tuning range. (b) SMSR of the VCSEL (C) for different wavelength during the tuning.

SMSR changes between 30 dB and 45 dB.

The VCSEL has a fibre-coupled maximum output power of 0.35 mW (-4.5 dBm) at the center wavelength of 868 nm. The threshold current is 3 mA and the thermal rollover is at 7 mA (Fig. 5.9(a)). Compared to the previous PIV-characteristics, it can be noticed that the threshold current is increased too. The increase of the threshold current is due to the small aperture of the VCSEL and the increased demand for current injection to reach the required gain.

Fig. 5.9(b) shows the differential resistance of the VCSEL for different bias-currents. The figure shows a quite high differential resistance between 300 Ω and 400 Ω. The higher resistance, compared to the previous values, is caused by the smaller aperture of the half-VCSEL as well. The ripples in the characteristic are caused by measurement inaccuracies.

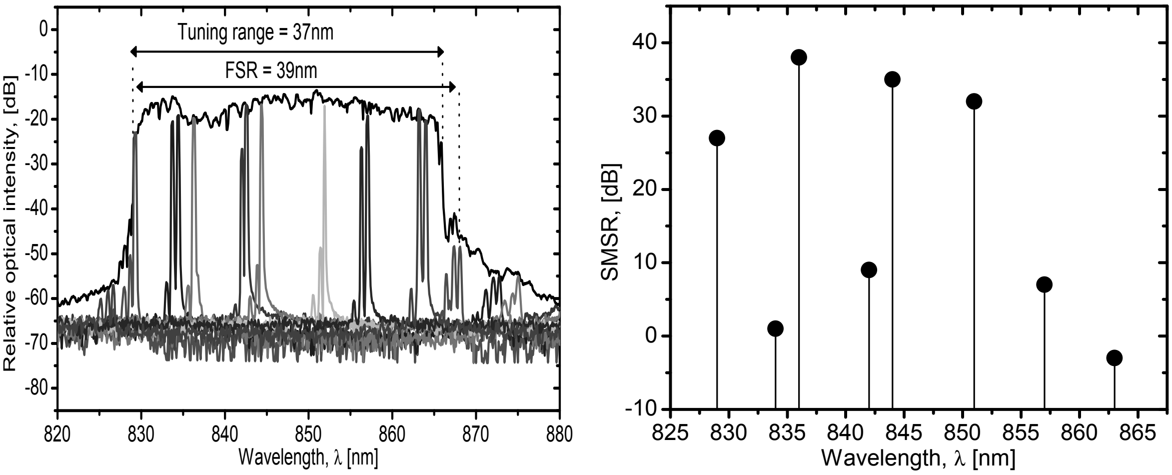

(a) (b)

Figure 5.7.: (a) Spectrum of the VCSEL (D) during the tuning for different tuning currents and a fixed bias current of 7 mA. The envelope indicates the tuning range. (b) SMSR of the VCSEL (D) for different wavelengths during the tuning.

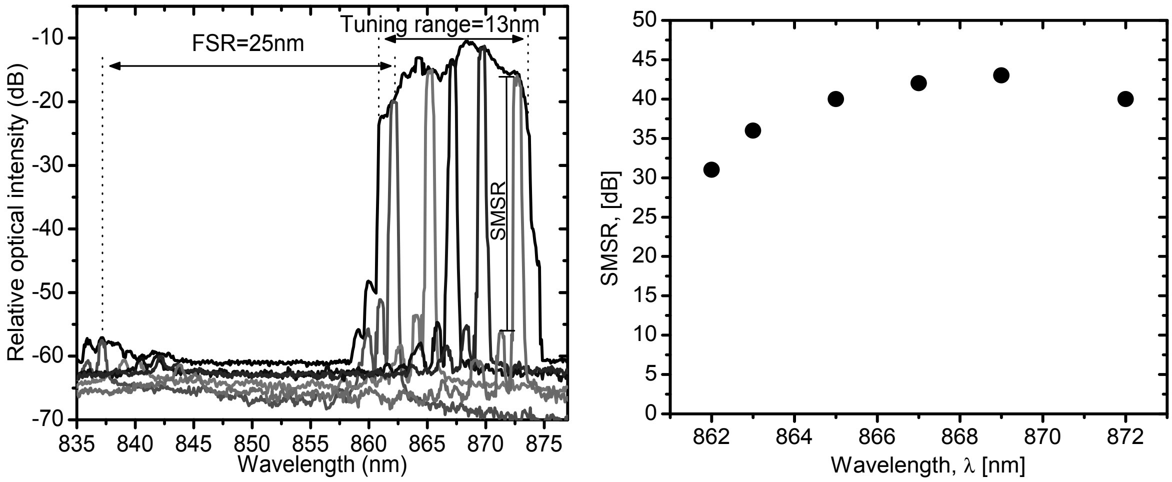

(a) (b)

Figure 5.8.: (a) Spectrum of the VCSEL (E) during the tuning for different tuning currents and a fixed bias current of 6 mA. The envelope indicates the tuning range. (b) SMSR of the VCSEL (E) for different wavelengths during the tuning.

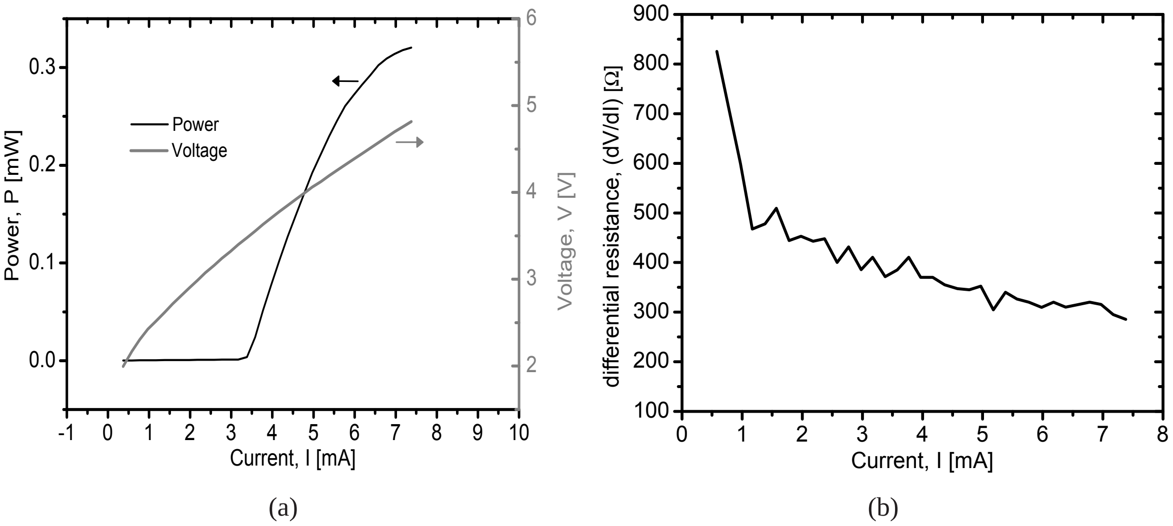

(a)

(b)

Figure 5.9.: (a) PIV-characteristics of the VCSEL (E) at 868 nm. (b) Differential resistance of the VCSEL (E) at 868 nm.

5.2. Tuning Speed

In many applications of the tunable VCSELs, it is essential to know how fast the device can be tuned. Compared to other tuning principles such as the electro static tuning or the piezo-electric tuning, the electro thermal tuning is slow due to the tuning bandwidth limitation of the mirror. The speed is limited by the thermal time constant of the membrane. A thermal tuning model of the membrane is shown in App. E.
The measurement of the tuning speed of the membrane determines how the tuning bandwidth is affected by increasing of the tuning frequency.

5.2.1. Measurement Setup

The setup of the measurement of the tuning speed is shown in Fig. 5.10. The VCSEL is connected to a current source providing the bias current. The temperature control is done via a temperature controlling unit. The bias-source of the membrane is connected to a signal generator, which adds a sine wave to the bias. The peak to peak amplitude of the sine wave and its frequency can be set by a signal generator. The outcoming light from the VCSEL is coupled into the fibre and its spectrum is measured by an OSA.

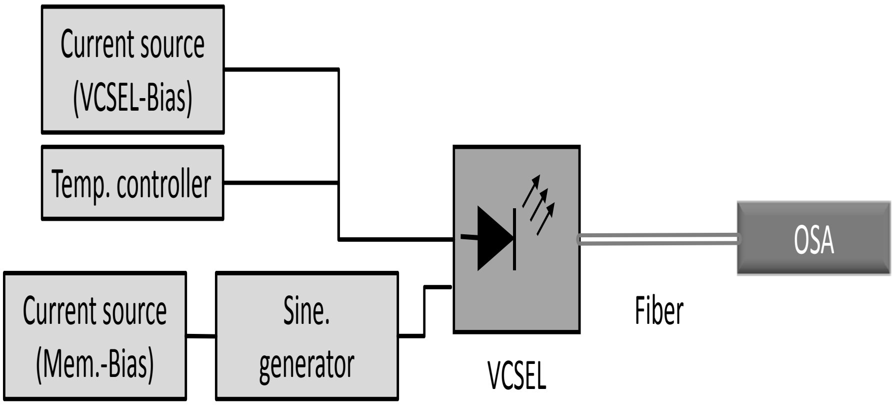

Figure 5.10.: Measurement setup for tuning speed.

5.2.2. Measurement Results

Fig. 5.11 shows the dependency of the resonance wavelength of the fundamental mode on the square of the membrane tuning current, which is proportional to the dissipated electrical power converted into the heat inside the membrane. The sine wave-form generator in Fig. 5.10 is not used in the measurement. The VCSEL (VCSEL (D) Sec. 5.1.2) is tuned by changing the membrane current with a bias current of 7 mA. The figure shows a linear dependency of the lasing wavelength on the heating power. The tuning spectrum of this VCSEL is shown in Fig. 5.7(a) with a tuning range of 37 nm.
To determine the tuning speed of the membrane, a fixed laser bias of 7 mA is kept while the membrane is biased to achieve the lasing at the central wavelength of 848 nm. After setting

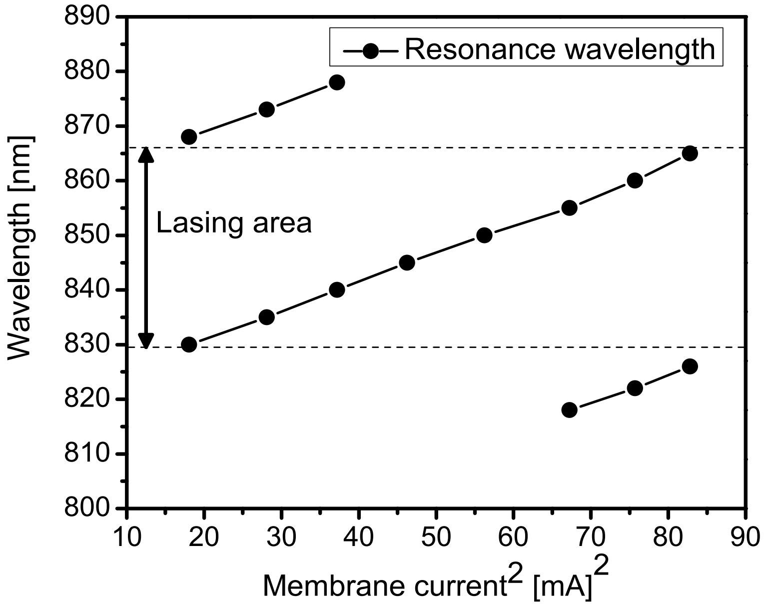

Figure 5.11.: Resonace wavelength versus squared membrane current. The measurement is done on VCSEL (D).

the bias, a sinusoidal wave is added to the bias. The peak to peak amplitude of the sinusoidal wave is chosen in the way that a tuning range of 25 nm is achieved at frequency of 1 Hz. To avoid driving the device to its damage limits, the complete tuning range of 37 nm is not used in this experiment. Fig. 5.12(a) shows the tuning ranges of the VCSEL for different tuning frequencies.

By increasing the tuning frequency and holding the other parameters, the heat inside the membrane is not fully dissipated during the modulation cycle and the tuning range converges towards the central wavelength (Fig. 5.12(a)). Finally with a tuning frequency of 700 Hz (f_{3dB}) the tuning range decreases to 12.5 nm, which is half of the original tuning range of 25 nm.
Fig. 5.12(b) shows the measured tuning ranges for different tuning frequencies. The measured points are fitted to the characteristic of the RC low-pass filter (App. D). A thermal time constant of $\tau_{th} = 0.4$ ms is extracted from the measurement. Due to the independency of frequency response on the operating bias and the modulation amplitude of the membrane, these results can be extended to the entire tuning range of 37 nm [66].

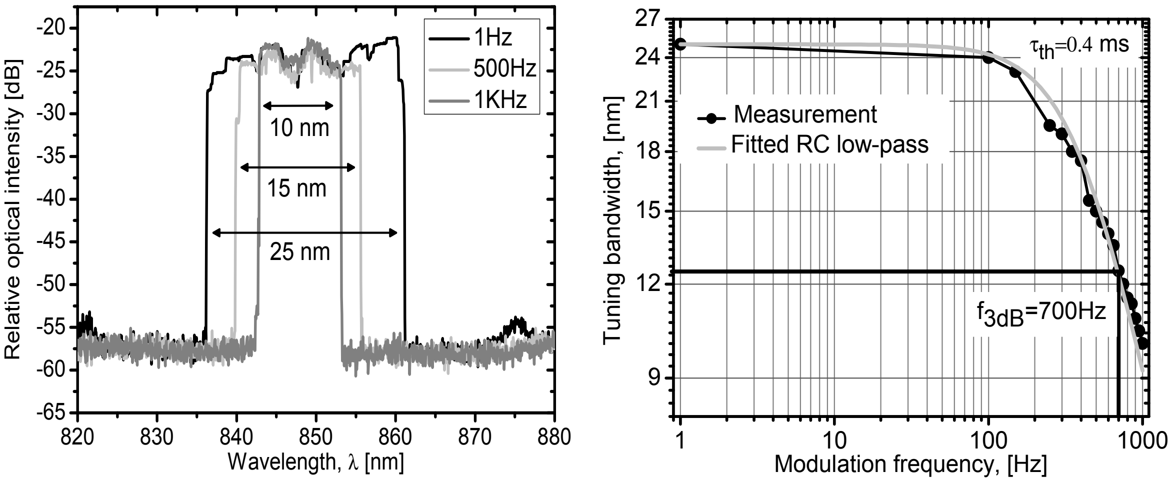

(a) (b)

Figure 5.12.: (a) Envelope of the spectrum during the tuning for tuning frequencies of 1 Hz, 500 Hz and 1KHz (VCSEL (D)). (b) Measured tuning bandwidth of the membrane as a function of membrane current frequency and the RC low-pass characteristic fitted to the measurement (VCSEL (D)).

5.3. Linewidth

The linewidth of the laser is an important parameter for the investigation of the coherent characteristics of the laser. It is caused by phase fluctuations of the output light. In the following the setup for the linewidth measurement is introduced and the results are discussed. It is common to measure the laser linewidth in a delayed self-heterodyne setup [68]. In this method the laser spectrum is shifted to an intermediate frequency via an acousto-optical modulator. This method avoids the measurement of the linewidth around DC-frequencies due to the restrictions in electrical spectrum analyzer (ESA) in the measurements at DC-frequencies. The used ESA in this work provides a spectrum measurement from 50 Hz, which has allowed measuring the linewidth with a delayed self-homodyne setup at DC-frequencies. The investigated VCSEL is a bulk-micromachined VCSEL (VCSEL (F)).

5.3.1. Measurement Setup

The linewidth of the VCSEL is measured with a delayed self-homodyne setup based on an interferometer. The interferometer allows superposing of the signal with itself. The measurement setup is shown in Fig. 5.13. After coupling the light in to the fibre, the light passes an optical isolator to avoid the reflections from the setup into the VCSEL. After it, the light enters an interferometer. The interferometer is based on two 3 dB couplers, one polarizer in one branch and a delay fiber (decorrelation fiber) in the other. The first coupler separates the light into two arms. The delay fiber introduces a delay (τ_0) between the two signals.

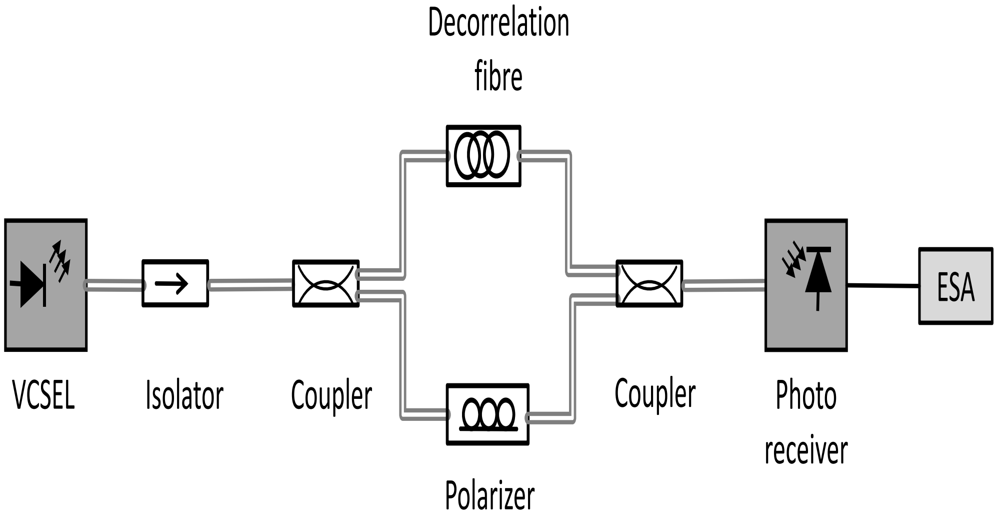

Figure 5.13.: Delayed self-homodyne setup for measuring the linewidth.

In order to realize the incoherent superposition of the light from the two branches, τ_0 should be larger than the coherence time of the laser. To achieve that the condition $\Delta f \tau_0 \gg 1$ should hold. The used decorrelation fiber in the setup has a length of 1400 m, which results in a time delay of $\tau_0 = 6.95\mu s$ for an effective refractive index of $n_{eff} = 1.49$. A minimum laser linewidth of $\Delta f = 300$ MHz results in $\Delta f \tau_0 = 2085$.

The polarization of light on the other arm can be changed via a polarizer to superpose the signals

from both arms with the same polarization. The homodyning takes place in the second coupler of the interferometer.
The light enters the photo receiver after the second coupler. The photo receiver is made of a broad band photo diode and a transimpedance amplifier. The photo receiver converts the superimposed signal from the interferometer to an electrical signal. The central frequency of this signal is 0 Hz and its single sided spectrum of is detected using the ESA.

5.3.2. Measurement Results

The investigated VCSEL (VCSEL (F)) emits at the wavelength of 845 nm without applying any tuning current. The normalized spectra of the delayed self-homodyne beat signal, measured by the ESA, for different output power levels are shown in Fig. 5.14. The measured spectra have the best match to a Voigt-profile. The Voigt-profile ($V(x)$) is the convolution of a Gaussian profile and a Lorentzian profile [69]:

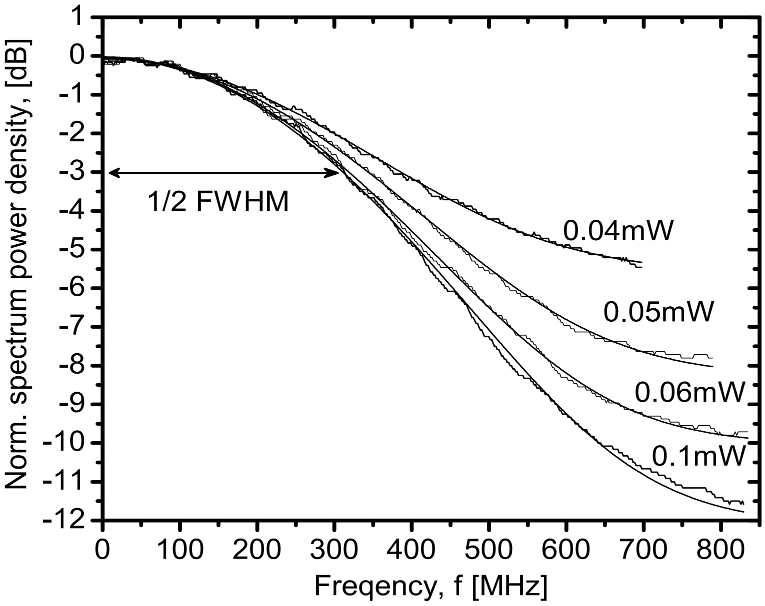

Figure 5.14.: Normalized spectrum power density of delayed self-homodyne signal over the frequency for different output power levels of VCSEL (F). A Voigt-profile has been fitted to each measurement.

$$V(x) = y_0 + A\frac{2\ln 2}{\pi^{3/2}}\frac{w_L}{w_G^2}\int_{-\infty}^{\infty}\frac{e^{-t^2}}{\left(\sqrt{\ln 2}\frac{w_L}{w_G}\right)^2 + \left(\sqrt{4\ln 2}\frac{x-x_c}{w_G} - t\right)^2}dt. \tag{5.1}$$

y_0, A, w_L, w_G and x_c in Eq. 5.1 are free parameters to fit the measurement to the characteristic. The Lorentzian part of the characteristic is due to the intrinsic linewidth of the VCSEL and the Gaussian part is caused by thermal effects. Due to dominance of the Gaussian part, the linewidth is defined as $\Delta f = 1/\sqrt{2} \times FWHM$ (Fig. 5.14) [67]. FWHM indicates the 3dB bandwidth of the Voigt-profil.

By increasing the output power via increasing the bias current, the intrinsic linewidth decreases thus the whole bandwidth of the measured spectrum decreases, as is shown in Fig. 5.14 for four different output powers. The smallest linewidth of 430 MHz is measured for the rollover current of 8 mA and output power of 0.1 mW. Fig. 5.15(a) shows the PI-characteristic of the VCSEL at 845 nm. The VCSEL has a threshold current of about 3 mA. The resulting linewidth Δf over the inverse optical power $1/P$ is shown in Fig. 5.15(b). The linewidth decreases linearly with the inverse optical power and a re-broadening is caused at thermal roll-over due to the increasing spontaneous emission effects [70]. The undulations in characteristic could be caused by polarization switching of the mode. In Fig. 5.15(b) a linear fit to the linewidth-inverse power characteristic shows a quite high linewidth-power product of $\Delta f \times P \approx 24$ MHz mW thus resulting in a high linewidth enhancement factor α_H [68] [70].

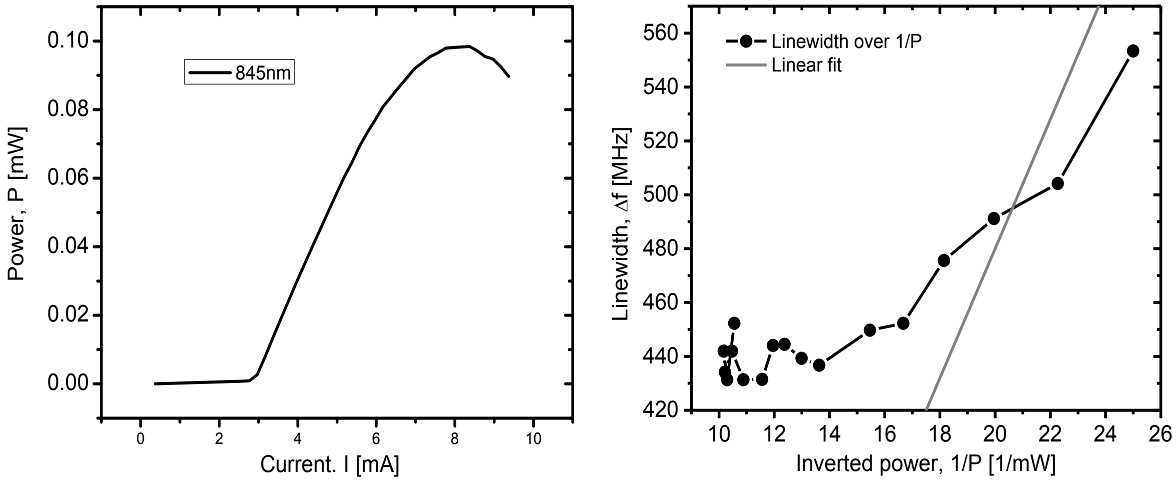

(a) (b)

Figure 5.15.: (a) PI-characteristic of the VCSEL(E) at 845 n m. (b)Linewidth over the inverse power of the VCSEL (E).

5.4. Polarization

The influence of SWG on the polarization of the VCSEL is investigated in this section. To clarify the origin of the stable state of the polarization in the device with SWG, another device from the same chip without the SWG and with the same top mirror is investigated as reference. In order to separate the linear polarizations in (011)- and $(0\bar{1}1)$-direction a polarization diversity setup is used, which is introduced in the following.

5.4.1. Measurement Setup

Two setups are used to characterize the VCSEL. The first setup is already introduced in Sec. 5.1.1. In this setup the outcoming light from the VCSEL is coupled directly into a multi-mode fibre, the power and spectrum are measured in an optical power meter and an OSA, respectively. The other setup, which we call polarization diversity setup, is shown in Fig. 5.16. It is a free space setup, in which the outcoming light from the VCSEL is collimated with a collimation lens and is redirected into the first polarization cube (to separate the two orthogonal polarizations) using a gold mirror with very low polarization dependent attenuation. A half-wave plate is used in front of the cube to fit the polarization axis of the light to the main axis of the cube. Due to the low polarization selectivity of the polarization cube in one direction, a second polarization cube is used. At the output of the cubes the light is focused into the fibers with focusing lenses. The fibers are connected from the other side to a power meter or an OSA [71].

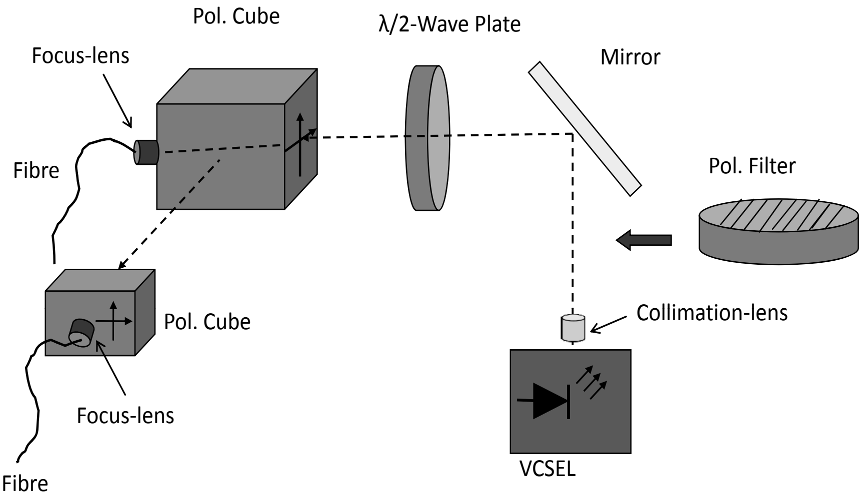

Figure 5.16.: Polarization diversity setup for measuring the Polarization.

Additionally a polarization filter is used after the collimation lens, to determine the orientation of the polarization compared to the gratings orientation of the VCSEL (Fig. 5.16).

5.4.2. Measurement Results

At first, a half-VCSEL without the SWG is investigated (VCSEL (G)). After adjusting the membrane on the half-VCSEL the first measurement setup in Sec. 5.4.1 is used to measure the device. Fig. 5.17(a) shows the tuning spectrum over the entire tuning range when changing the membrane current and a bias current of 5 mA. The figure shows a tuning range (the envelope) of about 12 nm from 827 nm to 839 nm with a SMSR higher than 30 dB. The maximum output power measured at the wavelength of 830 nm is about 0.08 mW at the thermal rollover current of 5.5 mA (3.5 V) with a threshold current of 2.5 mA (2.5 V) (Fig. 5.17(b)).

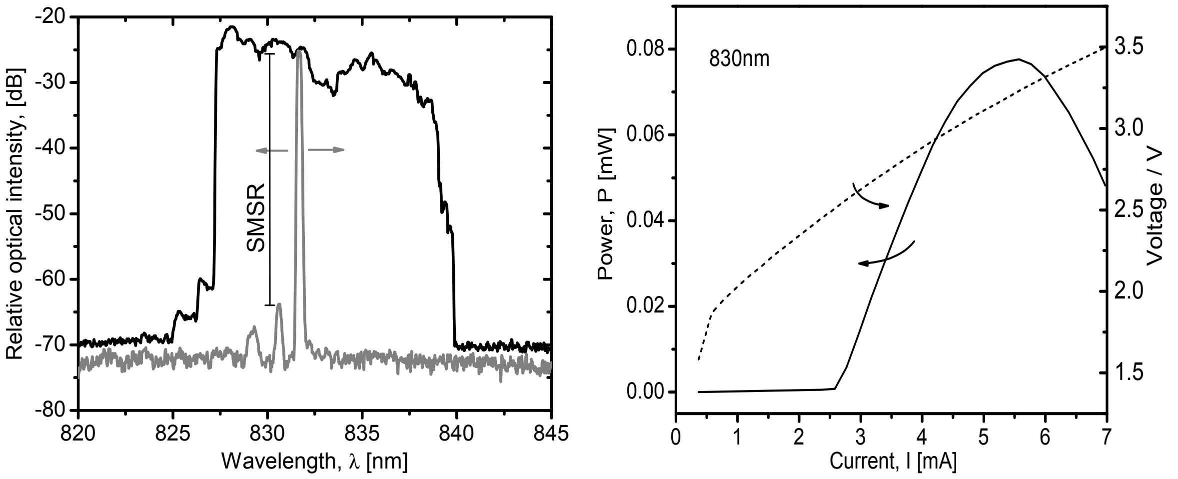

(a)

(b)

Figure 5.17.: (a) Fiber coupled spectrum of a the VCSEL (G) without the sub-wavelength grating. The envelope indicates the tuning range. (b) PIV-characteristic of the VCSEL (G) at 830 nm.

By using the polarization diversity setup in Fig. 5.16 the tuning spectrum for each polarization direction is measured separately as can be seen in Fig. 5.18. The figure shows that the state of polarization in the device without SWG is unstable during the tuning. At the beginning of the tuning at the wavelength of about 827 nm the polarization switches between the (011)-direction and $(0\bar{1}1)$-direction. Starting at the longer wavelength until around 833 nm the dominant polarization is in (011)-direction as shown in Fig. 5.18(a). From 833 nm the polarization direction switches to $(0\bar{1}1)$-direction and remains up to the end of the tuning range (Fig. 5.18(b)).

The same experiments with the same membrane have been then repeated on a half-VCSEL with SWG (VCSEL (H)). The half-VCSEL is on the same chip and has the same parameters as in the previous experiment. The only difference is that it has additionally a sub-wavelength grating in (011)-crystallographic direction. The fiber coupled tuning range of the device in Fig. 5.19(a) is about 11 nm from 834 nm to 844 nm for a constant laser bias of 5 mA. The device has a polarization-mode suppression ratio (PMSR) of larger than 35 dB during the tuning (Fig. 5.19(a)). PMSR is defined as the power difference between the polarization modes.

By separating the polarization directions using the setup shown in Fig. 5.16, it can be seen that the dominant polarization, which has been stabilized by sub-wavelength grating, is the one in $(0\bar{1}1)$-direction and remains stable during the tuning and does not switch to the (011)-direction (Fig. 5.19(b)). The state of polarization remains stable for different laser bias currents too. The PI-characteristics at two wavelength of 839 nm and 843 nm are shown in Fig. 5.20. The figure shows that the polarization mode polarized in $(0\bar{1}1)$-direction remains dominant even for different laser bias currents.

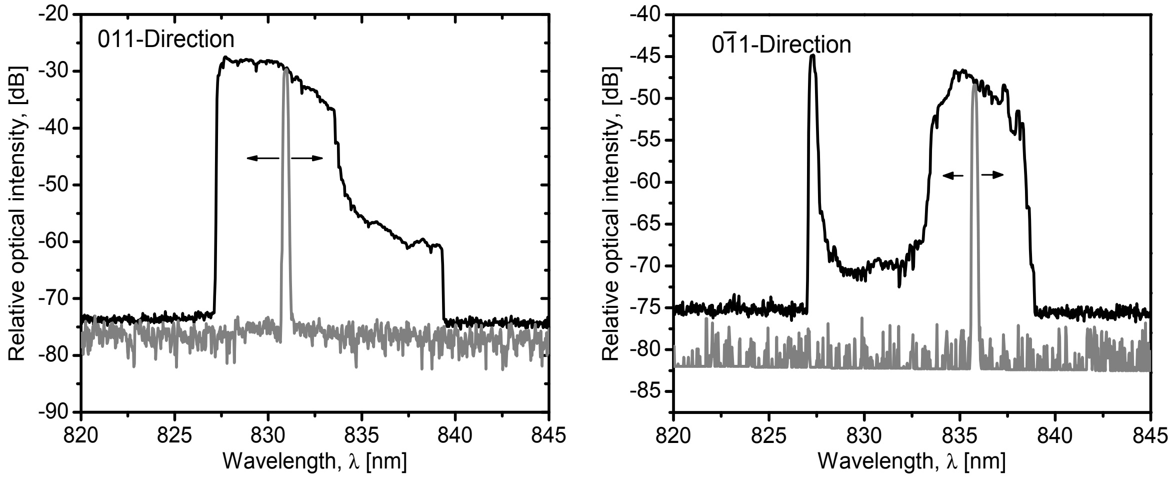

(a) (b)

Figure 5.18.: Spectrum of the VCSEL (G) without the sub-wavelength grating after separating the polarization modes using the polarization setup in Fig. 5.16. (a) (011)-direction. (b) (0$\bar{1}$1)-direction.

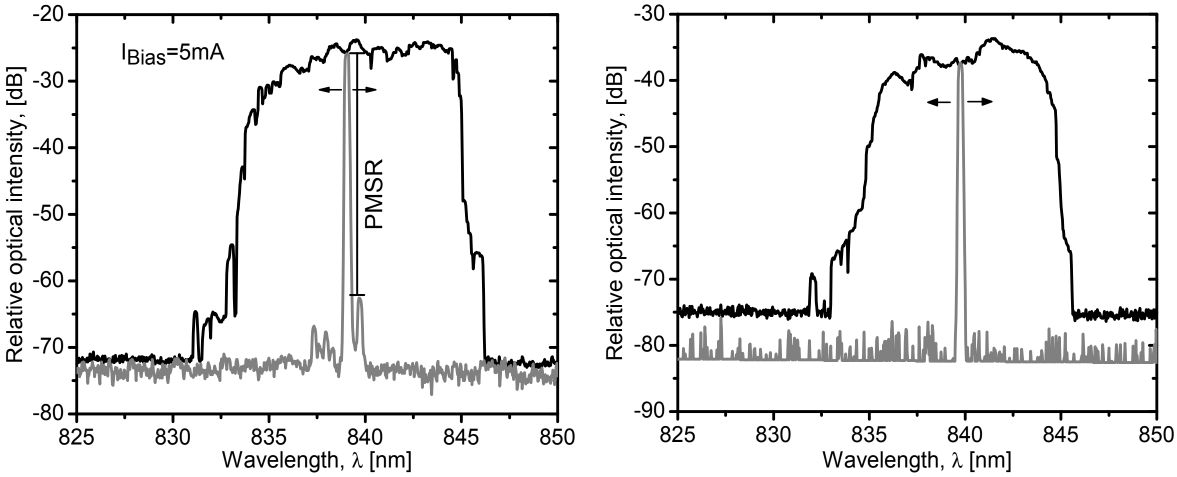

(a) (b)

Figure 5.19.: (a) Fiber coupled spectrum of the VCSEL (H) with the sub-wavelength grating. (b) Spectrum of the VCSEL (H) after separating the polarization modes using polarization setup in Fig. 5.16. The figure shows that the lasing mode over the entire tuning range is polarized in (0$\bar{1}$1)-direction.

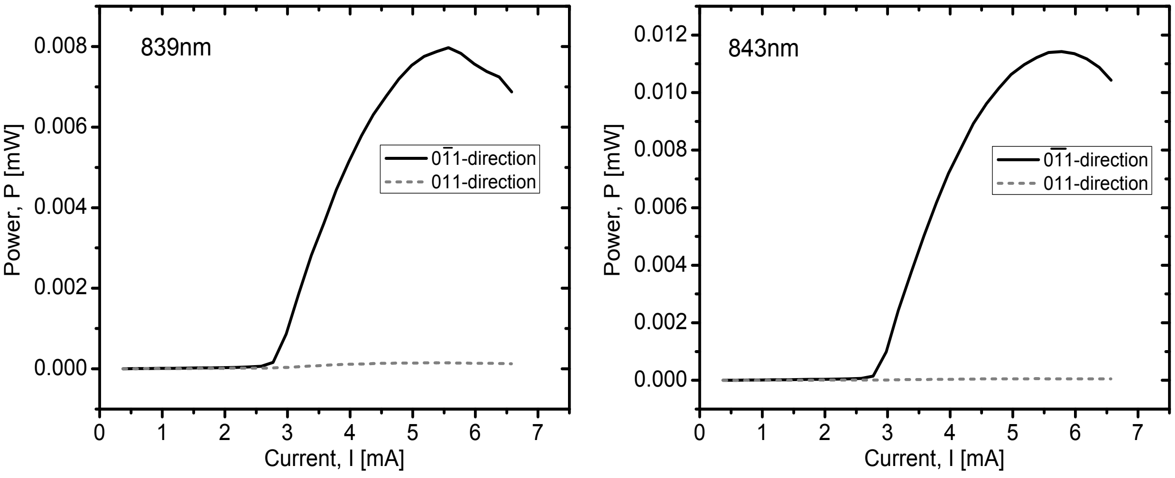

(a) (b)

Figure 5.20.: PI-characteristic of both polarization directions using the polarization diversity setup in Fig. 5.16 VCSEL (H). (a) At a wavelength of 839 nm. (b) At a wavelength of 843 nm.

5.5. Far Field

The beam broadening of the far field due to the transversal modes in a resonator can be characterized by a divergence angle θ_0. By measuring the spatial distribution of the radiated power in the far field, θ_0 can be determined. The information about θ_0 can be used to design a free space experiment or a fiber coupling. Using the Gaussian beam theory, the field distribution in the resonator can be determined as well.

5.5.1. Measurement Setup

To measure the far field of the VCSEL a free space measurement setup is used, as shown in Fig. 5.21. A photodiode, which is manipulated by a rotationary strut, is placed above the VCSEL. The VCSEL is connected to the current sources for the bias and the membrane actuation respectively. The mechanical setup is connected to a step motor that can rotate in ϕ and θ direction. With the help of the mechanical setup and the step motor, the photodiode is able to scan the space above the VCSEL in spherical coordinates. The photodiode converts the detected light into current. The photodiode is connected to a transimpedance amplifier, which converts the current from the photodiode into voltage. At the end, the voltage is measured using a volt meter.

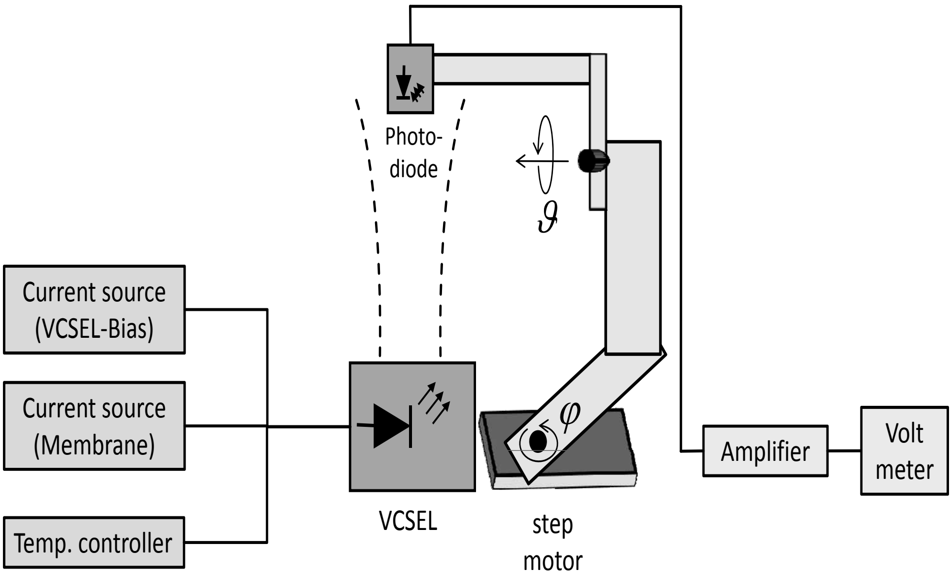

Figure 5.21.: Free space setup for measuring the far field of the VCSEL.

5.5.2. Measurement Results

The measured far field at the distance of z=20 (App. F) is shown in Fig. 5.22. From the figure a beam waist of $\omega(z_0) = 1$cm ($1/e$-bandwidth) is obtained. Using the Eq. F.3, a divergence angle of 2.8^o and a total angular spread of $\Theta_0 = 5.6^o$ are calculated. Putting the Θ_0 in Eq. 2.19, a beam waist of $\omega_0 = 5.5$ cm (spot-size of 11 μm) is obtained. This is in the same range compared to the 12 μm oxide aperture of the investigated VCSEL (VCSEL (I)).

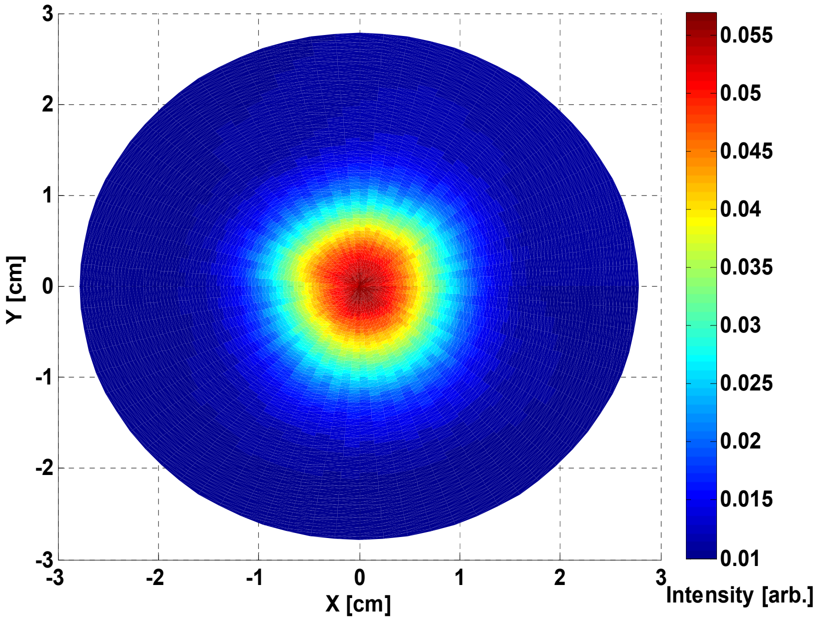

Figure 5.22.: Far field of the VCSEL (I) in a distance of z_0=20 cm .

5.6. Relative Intensity Noise

The measurement setup of the RIN is not complicated, however, extracting of the RIN from the measured signal is not trivial. Due to the noise characteristic of the RIN, it should be separated from the other noise terms in the measurement. The extraction and evaluation of RIN is described in App. G. Due to the absence of the parasitic effects in the RIN measurements, this characterization is very important for the investigation of the dynamics of the VCSELs.

5.6.1. Measurement Setup

The setup for measuring RIN is shown in Fig. 5.23. The VCSEL and the membrane are biased and the temperature is hold at 20^o C. The light from the VCSEL is coupled into the fiber and is detected via a photo receiver with a broad-band photo diode and a transimpedance amplifier. The photo receiver is connected to an ESA for measuring the received spectrum. To measure the DC-power, the photo receiver is connected to a voltmeter too.

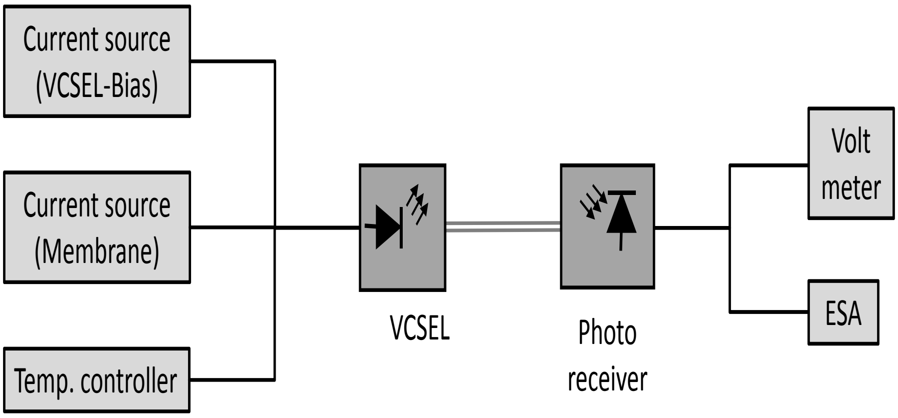

Figure 5.23.: Measurement setup for measuring of the RIN.

5.6.2. Measurement Results

The RIN of the investigated VCSEL (J) for the center wavelength of 840 nm after calculating from the measured spectrum according to App. G for different bias currents is shown in Fig. 5.24(a). VCSEL (J) is a bulk-micromachined VCSEL with a tuning range of 31 nm. The RIN at the resonance frequency f_r is reduced by increasing the bias current and reaches a minimum of about -100 dB/Hz at the rollover current of 6 mA.

By fitting the RIN measurement from Fig. 5.24(a) to Eq. 2.68 the resonance frequency can be extracted. A maximum resonance frequency of 2.3 GHz at the rollover is achieved. The damping rate γ over the square of the resonance frequency is shown in Fig. 5.24(b). From the figure a K-factor of 0.4 ns is extracted. According to the Eq. 2.60, the K factor can be used to estimate the maximum intrinsic modulation bandwidth, i.e. $f_{\text{3dB, damping}} = 22.2$ GHz (Eq. 2.60) limited by the damping rate in the absence of the thermal and the parasitic limitations.

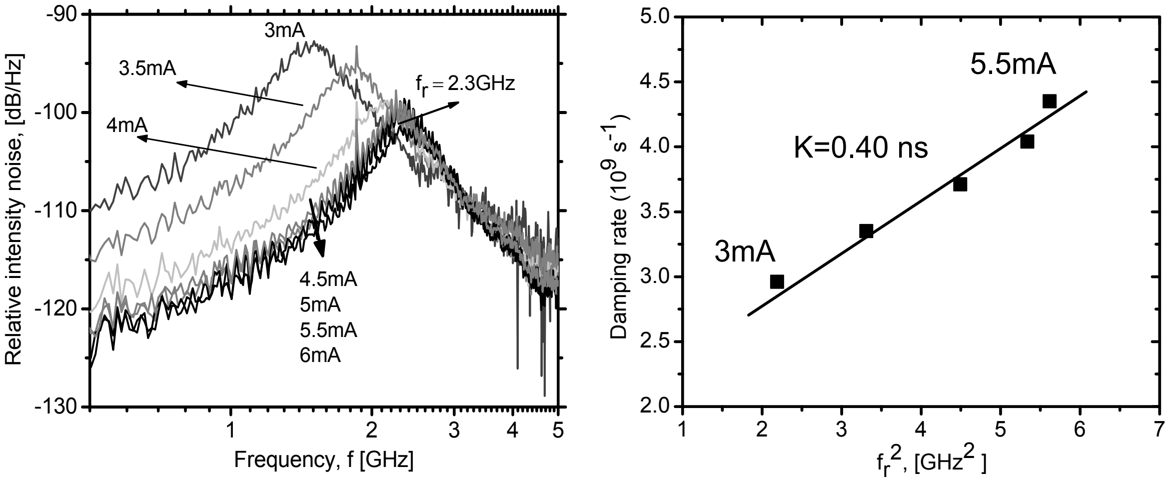

(a) (b)

Figure 5.24.: (a) Calculated RIN from the measured spectrum of the VCSEL (J) at the wavelength of 840 nm for different bias currents (RBW = 1MHz). (b) Damping rate for different resonance frequencies fitted by K=0.4 ns (VCSEL(J))

5.7. Small-Signal Amplitude Modulation

The small-signal AM-measurement determines the practical modulation behavior and the modulation bandwidth of the VCSEL, including thermal and parasitic effects. The small-signal AM-bandwidth shows the range of the maximum possible data rate that can be directly transmitted by the VCSEL. By measuring the reflection parameters (S_{11}), an equivalent circuit for the VCSEL is modeled too.

5.7.1. Measurement Setup

The measurement setup for the small-signal AM is shown in Fig. 5.25. The transmission and the reflection parameters (S_{21} and S_{11} respectively) of the VCSEL are measured with the help of a network analyzer. To measure the S_{21} parameter, the port 1 of the analyzer is connected to a bias-Tee. The bias-Tee adds the modulation signal from the analyzer to the bias current of the VCSEL. Additionally, the VCSEL is temperature controlled and is connected to the membrane current source. The light from the VCSEL is coupled into the fibre and is detected in the photo receiver as described in Sec. 5.6.1. The photo receiver is connected to the port 2 of the network analyzer.

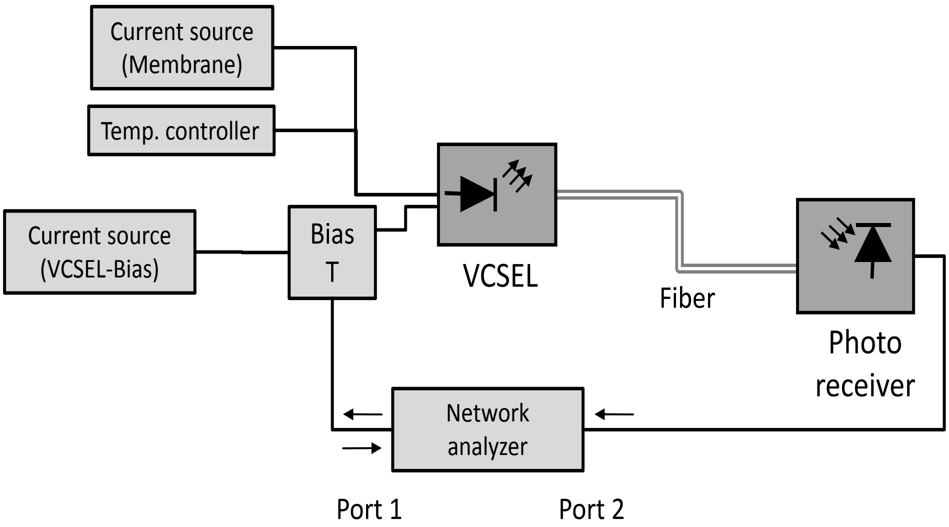

Figure 5.25.: Measurement setup for measuring of the small-signal AM and extracting the equivalent circuit.

For measuring the S_{11} parameters, only port 1 is used. The modulation signal is sent via the bias-Tee to the VCSEL and the reflection from the VCSEL is detected again in port 1.

5.7.2. Measurement Results

The small-signal AM response of a VCSEL at the wavelength of 850 nm for different bias currents from 3 mA to 8 mA is shown in Fig. 5.26 [11]. The measured VCSEL (VCSEL (A)) is the bulk-micromachined VCSEL already presented in Sec. 5.1.2. The modulation bandwidth increases with the bias current and reaches a maximum of about 5.5 GHz for the rollover of

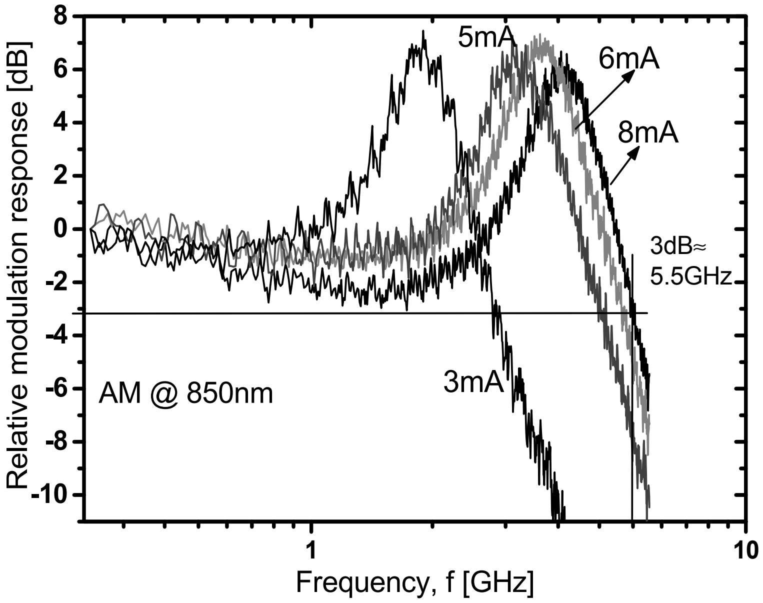

Figure 5.26.: Small-signal AM response of transmission (S_{21}) at different bias currents for a wavelength of 850 nm (VCSEL A).

about 8 mA in Fig. 5.26.

Fig. 5.27(a) shows the small-signal AM-response of a VCSEL (VCSEL (J) Sec. 5.6.2) at the central wavelength of 840 nm. Due to the decrease of the oxide aperture from 13 μm in VCSEL (A) to 11 μm in VCSEL (J) and the increase of parasitic capacitance, the modulation bandwidth decreases to 3.2 GHz at the rollover current, instead of 5.5 GHz (Fig. 5.26).

Comparing the AM-response of the VCSEL to its RIN measurement from Fig. 5.24, it can be seen that the resonant frequencies are in the same range. Thus, we can conclude that the present of parasitic and thermal effects causes the reduction of the modulation bandwidth to 3.2 GHz from the $f_{\text{3dB, damping}} = 22.5$ GHz calculated in Sec. 5.6.2.

Fig. 5.27(b) shows the small-signal AM-response of the surface-micromachined VCSEL (VCSEL (E)) introduced in Sec. 5.1 (Fig. 5.8) at the central wavelength of 868 nm. VCSEL (E) has an oxide aperture of 11 μm. The modulation bandwidth of the VCSEL by rollover current of 7 mA amounts to 3.2 GHZ. Comparing Fig. 5.27(a) with Fig. 5.27(b) shows that the micromachining method does not have any influence on the modulation bandwidth, as the both surface- and bulk-micromachined VCSELs with the same half-VCSEL achieve the same modulation bandwidth at the rollover currents.

The small-signal impedance dependency of the bulk-micromachined VCSEL (VCSEL (J)) in Fig. 5.27(a) on the bias current is extracted from the S_{11} parameters, as shown in Fig. 5.28. An equivalent circuit model is also derived to model these impedance characteristics. The circuit consists of lumped elements to model the physical parasitics in the VCSEL. The half-VCSEL (including parasitic) is represented approximately by the parallel combination of a resistance R_R and a capacitance C_R. The coplanar waveguide feed line is modeled as an ideal transmission line with a characteristic impedance Z_L and a phase delay Φ_L. The parasitic capacitance under the contact pads are represented by the capacitance C_P, while a resistance R_P accounts for the pad loss [33]. The equivalent circuit is simulated in the Agilent®Advanced Design

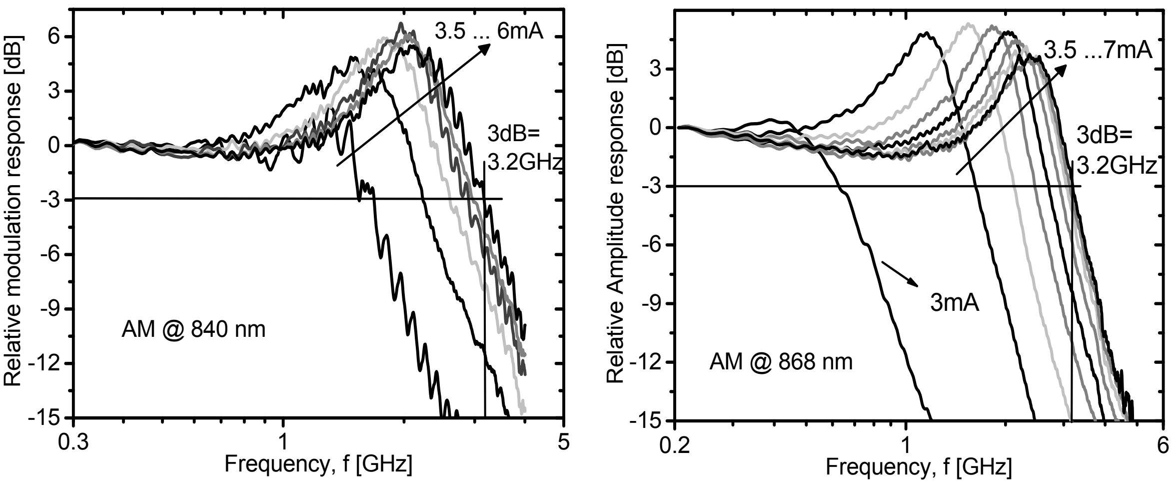

(a) (b)

Figure 5.27.: (a) Small-signal AM response (S_{21}) of a bulk-micromachined VCSEL (VCSEL (J)) with an oxide aperture of 11 μm. (b) Small-signal AM response (S_{21}) of a surface-micromachined VCSEL (VCSEL (E)) with an oxide aperture of 11 μm.

System. The components values are extracted by fitting the simulated input impedance to the measured data. As listed in Fig. 5.28, the external elements for the feed line and contact pads hold constant, while both the capacitance and the resistance of the active region alters under various bias currents. The circuit model provides a way to identify the intrinsic property of the VCSEL active region and allows further impedance matching to improve the transmission efficiency.

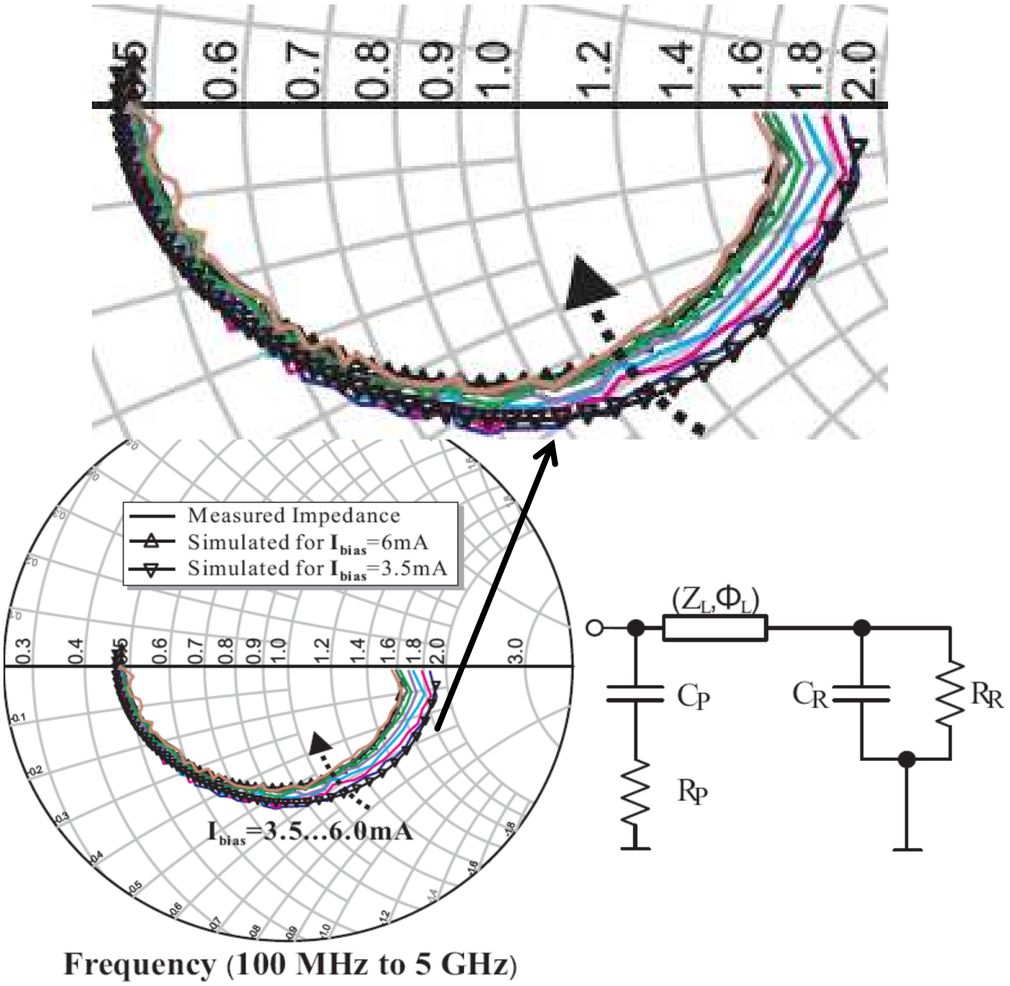

I(mA)	R_P(Ω)	C_P(pF)	Z_L(Ω)	P_L(°@1GHz)	C_R(pF)	R_R(Ω)
3.5	64	0.98	100	6.4	0.37	96
4	64	0.98	100	6.4	0.398	90
4.5	64	0.98	100	6.4	0.404	89
5	64	0.98	100	6.4	0.411	87.6
5.5	64	0.98	100	6.4	0.425	84.5
6	64	0.98	100	6.4	0.436	83
6.5	64	0.98	100	6.4	0.44	82.6

Figure 5.28.: Smith chart and the equivalent circuit with the measured and the calculated frequency-dependent impedance extracted from the complex S_{11} parameters (VCSEL (J)).

5.8. Large-Signal Amplitude Modulation

The large-signal amplitude modulation measurement is performed by data transmission via direct modulation of the VCSEL. The eye diagram is chosen here to determine the quality of the transmitted signal. The transmission is in the back-to-back configuration, which means that the fiber distance between the VCSEL and the receiver is just a few meters.

5.8.1. Measurement Setup

The measurement setup of the large-signal modulation is shown in Fig. 5.29. The data, which are modulated by the VCSEL, are generated with a bit-generator. The generated bits, which are pseudo-random bit stream ($2^{23}-1$), are added to the bias current of the VCSEL with a bias-Tee. The VCSEL has been biased above the threshold. Additionally the VCSEL is under temperature control and the membrane is connected to the current source.

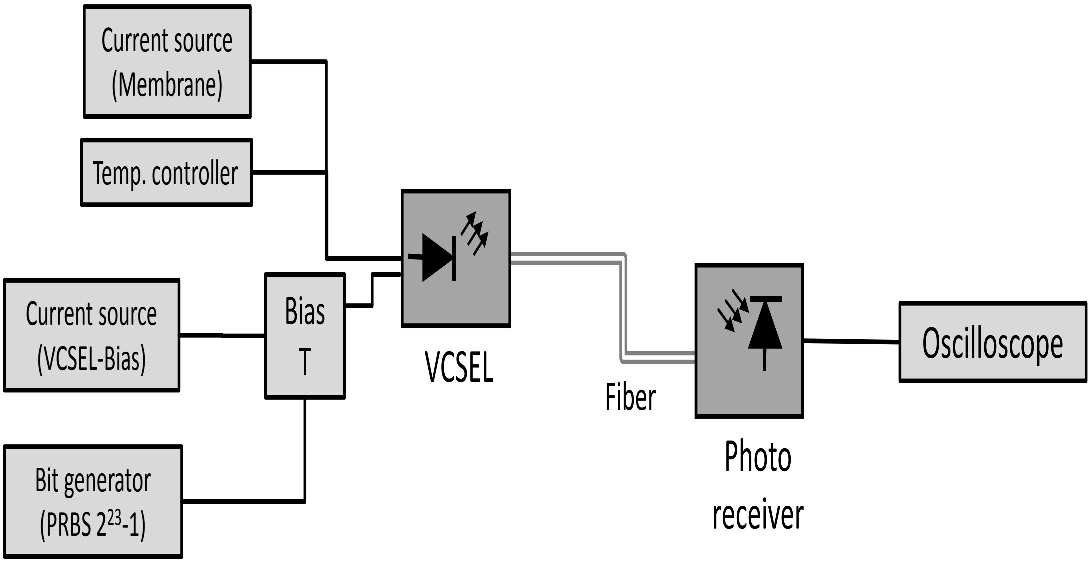

Figure 5.29.: Measurement setup for measuring of large-signal AM.

The output light of the VCSEL is coupled into the fibre with a length of a few meters and is detected with a photo receiver (Sec. 5.23). The photo receiver is connected to a sampling oscilloscope to measure the eye diagram of the received signal.

5.8.2. Measurement Results

The VCSEL under the investigation here is a bulk-micromachined VCSEL (VCSEL (J) Sec. 5.6.2), its RIN and small-signal AM response being already presented in Fig. 5.24 and Fig. 5.27(a) respectively. The VCSEL is operated at the central wavelength of 840 nm.

Fig. 5.30 shows the eye diagram of the received signal with the data rate of 4 Gb/s (Fig. 5.30(a)) and 5 Gb/s (Fig. 5.30(b)). Comparing the two eye diagrams shows that as the data rate increases, the eye opening decreases. This is due to the limitation of the small-signal AM-response to 3.2

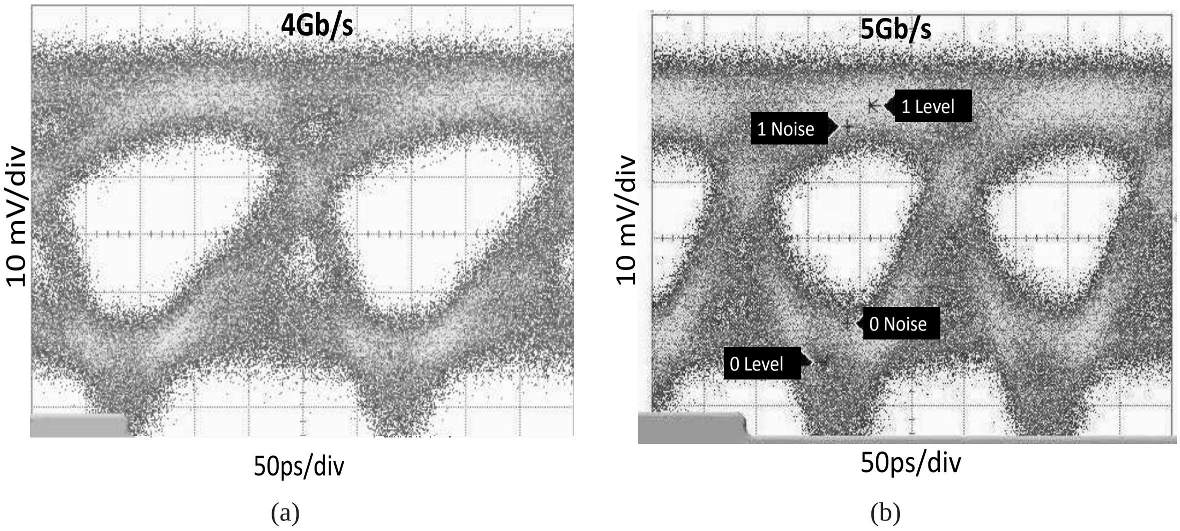

(a) (b)

Figure 5.30.: Received eye diagram in (a) 4 Gb/s operation, (b) 5 Gb/s operation (VCSEL (J)).

GHz, which does not allow the higher data rates. The eye diagrams are inverted because of the negative conversion gain of the photo receiver.

6. Conclusion

6.1. Summary

This thesis demonstrates the latest achievements in the field of the high-speed tunable short-wavelength VCSELs. According to the knowledge of the author, the developed device in this work exhibited the highest amplitude modulation bandwidth of 5.5 GHz for the tunable VCSELs among the published results at the time of its publication in [11]. At the same time the device is the first developed high-speed tunable VCSEL in the short-wavelength range. The developed device exhibits a wide single-mode tuning range of up to 37 nm, which is the highest reported tuning range around 850 nm achieved by VCSELs. To achieve these, the long tradition and experience at the photonic group of the Technical University Darmstadt in fabrication and development of the MEMS-mirrors for the long wavelength VCSELs is combined with the long tradition and experience in Chalmers University of technology in Göteborg Sweden in design and development of high-speed non-tunable short-wavelength VCSELs. The Walter Schottky Institute has provided the wafers for semiconductor DBRs and the IEIIT-CNR in Torino has supported us with the cold cavity simulations. The goal was to develop a high-speed tunable VCSEL, which is suitable for applying in the optical interconnects. This work is presented in 6 chapters.

The first chapter gives a brief introduction to the thesis. It begins with a short introduction in the history of the lasers and specially VCSELs. The comparison of VCSELs with the edge-emitter lasers, the development and the state-of-art short-wavelength tunable VCSELs and some of their potential applications, such as Datacom and optical interconnects, are discussed in this chapter.

The second chapter provides the reader with a basic theory to understand this work. This chapter is divided into three main parts. The first part introduces the passive optical resonators, specially the half-symmetric resonator, which is the basic structure of the developed tunable VCSEL in this work. By using the ABCD-notation the beam waist is calculated from the cavity length and RoC, as shown in App. A. The second part of the chapter introduces the DBR-structure and the transfer-matrix-method to simulate and calculate the reflectivity bandwidth of the implemented DBRs in this work. The last part of the chapter reviews the basics of the active optical resonator with a brief introduction of the laser condition and the rate equations. The small-signal AM, the large-signal AM, RIN and the linewidth are discussed as well. At the end of the chapter, the condition for the single-mode operation and the polarization stability of the device are discussed.

The third chapter introduces the structure and the design of the half-VCSEL. The half-VCSEL is designed and processed by Chalmers University of Technology with the cold-cavity simulation support from University of Torino. TU-Darmstadt contributed in the layout design by performing the microwave simulations and determining the dimensions of the top-layout of the half-VCSEL. The half VCSEL, which mainly consists of the bottom DBR, oxide aperture and

the active area, is grown on a GaAs-substrate.
The forth chapter includes the design and the fabrication of the top movable membrane and the modeling of the device via simulation. Three kinds of movable membranes suitable for the integration with the developed half-VCSEL are developed in this work. They are the semiconductor mirror, the dielectric mirror and the hybrid mirror. The semiconductor and the hybrid mirrors are suitable for the bulk micromachining and the dielectric mirror is optimized for the surface micromachining. Using DBR-simulations and measurements, the differences between these mirrors are highlighted. The fabrication steps of the mirrors are also described in this chapter. Among the developed DBRs, the dielectric DBR exhibits the highest 99.7$\%$ reflectivity stop bandwidth of 97 nm. After the discussion about DBRs, one-dimensionl simulations for the whole device, which are done in University of Torino, are presented. The simulations are done for the devices with SWG as well as for the devices without SWG. At the end, the high frequency simulations are carried out to investigate the effect of the whole mirror on the transmission lines. The simulations show that applying a trench in the membrane frame increases the bandwidth.
The fifth chapter summarizes the measurement results on all devices. Several different measurements such as PIV-measurement, the tuning range, the tuning speed, the linewidth, the polarization, the far field, RIN, the small AM and the large AM are applied on the three main groups of devices to characterize them. These three groups are the bulk-micromachined devices, the surface-micromachined devices and the devices with SWG. The main achievements for the bulk-micromachined devices are a maximum single-mode tuning range of 37 nm, a maximum output power of 0.8 mW, and a maximum modulation bandwidth of 5.5 GHz. For the surface-micromachined device, a single-mode tuning range of 13 nm, a maximum output power of 0.35 mW and a small AM bandwidth of 3.2 GHz are achieved. Investigating the devices with SWG shows that the SWG on the top of the half-VCSEL can stabilize the polarization state of the device.
The last chapter includes the summary and outlook.

6.2. Outlook

Since the development of the presented high-speed device has just started, there are a large variety of future works that can be performed. Some significant directions are outlined in the following paragraphs.

Stability of the devices in terms of performance: The developed devices have shown some variation in performance from chip to chip and even on the same chip. For example, the device with the highest tuning range did not have the highest AM bandwidth and the highest output power. To overcome this problem, more experiments in terms of the design and the manufacturing on both sides (the half-VCSEL and the membrane) should be done to stabilize a more reliable technology to produce stable devices with a high performance and high yield.

Packaging of the device: The measurements presented in this work are carried out by probing the unpackaged devices. That leads to an inaccuracy in the results due to the environment influence and the inaccuracy of the probing itself. Furthermore the life time of the device under test is reduced due to the high mechanical sensibility of the probing setup. To avoid these drawbacks a proper packaging for the device should be developed. The packaging will lead to even better results for the devices.

Surface-micromachining: To achieve mass production and commercializing the product, more work should be done on the surface-micromachining. This work has shown that applying a novel surface-micromachining developed in our Institute is possible on these devices. The developed surface-micromachined devices have shown some performance limits. The limitation in tuning range is mainly due to the mismatching of the surface-micromachining process steps to the surface and design of the half-VCSELs, which were originally designed for the bulk-micromachining. A proper half-VCSEL for the employed surface-micromachining should be developed. During this work, the partners from Chalmers have developed a surface-micromachined chip based on a different surface-micromachining technology and the suitable half-VCSELs. They could achieve better results in terms of the tuning range than ours [68] [74]. Considering the excellent results from our surface-micromachined technique for the long wavelength VCSELs [58], better tuning range results with our technology can be expected.

Life time tests: The last step before applying the developed VCSEL in the commercial products is the life time and the reliability measurements. The performance degradation during the operation time in a defined environment by the temperature, the humidity and pressure should be investigated.

A. Plane-Concave Resonator with Two Media

Fig. A.1 shows a plane-concave resonator with two mediums with different refractive indices n_1 and n_2 inside the resonator. The q-factor at different places in the resonator for the given beam waist (ω_{om} with $m \in \mathbb{Z}$), the radius of curvature (ρ) and the refraction index (n) is given by [73]:

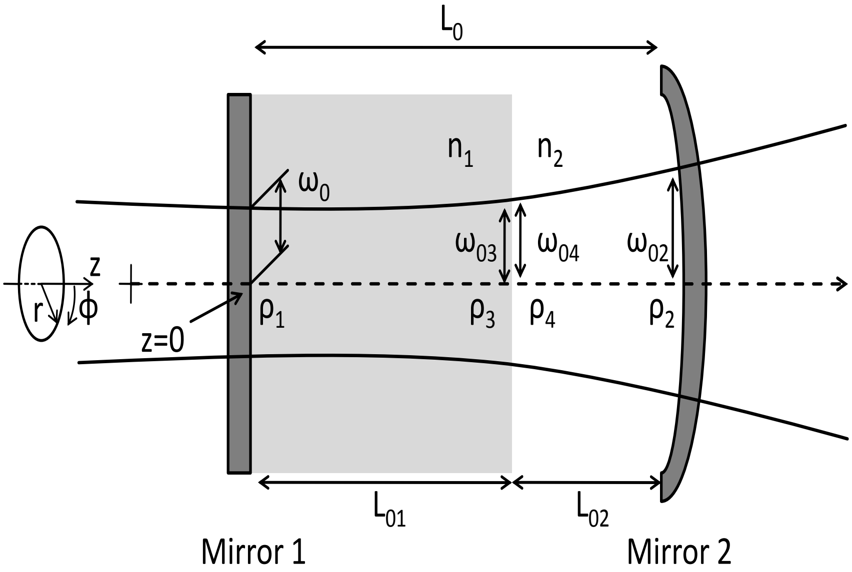

Figure A.1.: Plane-concave resonator with two different medien with different refractive indices inside the resonator.

$$\frac{1}{q} = \frac{1}{\rho} - i\frac{\lambda}{\pi\omega_{0m}^2 n}. \tag{A.1}$$

The q-factor at $z = 0$ (q_0) with $\rho_1 = \infty$ is:

$$q_0 = i\frac{\pi\omega_0^2 n_1}{\lambda}, \tag{A.2}$$

where ω_0 is the beam waist at $z = 0$. The q-factor at the border between two mediums at $z = L_{01}$ ($q = q_3$) in the medium with $n = n_1$ is given by the following equations:

$$q_3 = q_0 + L_{01}, \tag{A.3}$$

$$\frac{1}{q_3} = \frac{1}{\rho_3} - i\frac{\lambda}{\pi\omega_{03}^2 n_1}. \tag{A.4}$$

The ABCD-matrix for changing the medium is $\begin{pmatrix} A & B \\ C & D \end{pmatrix} = \begin{pmatrix} 1 & 0 \\ 0 & \frac{n_1}{n_2} \end{pmatrix}$. Deriving from this matrix the q-factor at $z = L_{01}$ (q_4) in the medium with $n = n_2$ is given by the following equations:

$$q_4 = \frac{n_2 q_2}{n_1}, \tag{A.5}$$

$$\frac{1}{q_4} = \frac{1}{\rho_4} - i\frac{\lambda}{\pi\omega_{04}^2 n_2}. \tag{A.6}$$

Then, the q-factor at $z = L_0$ (q_2) is given by:

$$q_2 = q_4 + L_{02}, \tag{A.7}$$

$$\frac{1}{q_2} = \frac{1}{\rho_2} - i\frac{\lambda}{\pi\omega_{02}^2 n_2}. \tag{A.8}$$

By solving these equations and using substitutions ω_0 can be obtained as:

$$\omega_0 = \sqrt{\frac{\lambda}{\pi n_2}\sqrt{M(\rho_2 - M)}}, \tag{A.9}$$

with $M = \frac{n_2}{n_1}L_{01} + L_{02} + L_{\text{eff}}^1 + L_{\text{eff}}^2$ (Eq. 2.28).

B. Half-VCSEL

Design wavelength: 850 nm										
Composition grading: Linear										
Substrate: Undoped GaAs										
Layer No	**Material**	**Group**	**Repeat**	**Mole Fraction (x)**		**PL (nm)**	**Thickness (µm)**	**Doping**		
				Start	**Finish**			**Level (cm-3)**	**Type**	**Material**
24	GaAs						0,003	1E+20	P	C
23	Al(x)GaAs			0,15			0,004	5E+19	P	C
22	Al(x)GaAs			0,15			0,0205	5E+18	P	C
21	Al(x)GaAs	3	3	0,15			0,071	5E+17	P	C
20	Al(x)GaAs	3	3	0,15			0,05	5E+18	P	C
19	Al(x)GaAs			0,15			0,0641	5E+17	P	C
18	Al(x)GaAs			0,9	0,15		0,02	5E+17	P	C
17	Al(x)GaAs			0,98			0,03	5E+17	P	C
16	Al(x)GaAs			0,9			0,055	5E+17	P	C
15	Al(x)GaAs			0,3	0,6		0,09			
14	Al(x)GaAs			0,3			0,02			
13	GaAs					842,5	0,006			
12	Al(x)GaAs	2	2	0,3			0,008			
11	GaAs	2	2			842,5	0,006			
10	Al(x)GaAs			0,3			0,02			
9	Al(x)GaAs			0,6	0,3		0,09			
8	Al(x)GaAs			0,9			0,0591	2E+18	N	Si
7	Al(x)GaAs			0,15	0,9		0,02	2E+18	N	Si
6	Al(x)GaAs	1	36	0,15			0,0419	2E+18	N	Si
5	Al(x)GaAs	1	36	0,9	0,15		0,02	2E+18	N	Si
4	Al(x)GaAs	1	36	0,9			0,0484	2E+18	N	Si
3	Al(x)GaAs	1	36	0,15	0,9		0,02	2E+18	N	Si
2	GaAs						1	3E+18	N	Si
1	GaAs						0,5			

Table B.1.: Epitaxial structure of the GaAs-based half-VCSEL.

C. DBR

	Wavelength	845 nm									
Loop	Loop	Material	x_Al	y_Ga	z_In	Thickness (nm)	Type	Dose	Pressure (Mpa)	n	
	1	AlGaAs:Si	0,8549	0,1451	0,0000	303,03	Si	1,00E+18		3,0655	**Etching stop 85% Al; 300nm**
3	**1**	AlGaInAs:Si	**0,1607**	**0,8143**	**0,0250**	60,84	Si	1,00E+18	171	3,4733	
	1	AlGaAs:Si	0,8499	0,1501	0,0000	68,86	Si	1,00E+18	99	3,0682	**ca. 85% Al**
3	**1**	AlGaInAs:Si	**0,1525**	**0,8325**	**0,0150**	60,84	Si	1,00E+18	109	3,4784	
	1	AlGaAs:Si	0,8499	0,1501	0,0000	68,86	Si	1,00E+18	99	3,0682	
3	**1**	AlGaInAs:Si	**0,1442**	**0,8508**	**0,0050**	60,83	Si	5,00E+17	48	3,4837	
	1	AlGaAs:Si	0,8498	0,1502	0,0000	68,84	Si	5,00E+17	99	3,0682	
1	**1**	AlGaAs:Si	**0,1400**	**0,8600**	**0,0000**	60,83	Si	5,00E+17	17	3,4864	
8	**1**	AlGaAs:Si	0,8499	0,1501	0,0000	68,30	Si	5,00E+17	99	3,0682	
	1	AlGaAs:Si	**0,1400**	**0,8600**	**0,0000**	60,83	Si	5,00E+17	17	3,4864	
5	**1**	AlGaAs	0,8498	0,1502	0,0000	68,84		0,00E+00	99	3,0682	
	1	AlGaAs	**0,1400**	**0,8600**	**0,0000**	60,59		0,00E+00	17	3,4864	
Pair number **22,5**											

Total Thickness:	**3318,58 nm**
Thickness mirror:	**2906,20 nm**

Table C.1.: Epitaxy-structure of the semiconductor DBR with 22.5 pairs with the thickness of just $\lambda/4$. Maximum indium introduced in layers is 2.5 %.

Wavelength: 845 nm

Loop	**Loop**	**Material**	**x_Al**	**y_Ga**	**z_In**	**Thickness (nm)**	**Time(s)**	**type**	**Dose**	**n**	**Pressure (Mpa)**	
	1	AlGaAs:Si	0,8549	0,1451	0,0000	303,03	1350,71	Si	1,00E+18	3,0655		**Etching stop 85% Al; 300nm**
3	**1**	AlGaInAs:Si	**0,1607**	**0,8143**	**0,0250**	60,84	174,61	Si	1,00E+18	3,4733	171	
	1	AlGaAs:Si	0,8499	0,1501	0,0000	68,86	305,56	Si	1,00E+18	3,0682	99	**ca. 85% Al**
3	**1**	AlGaInAs:Si	**0,1525**	**0,8325**	**0,0150**	60,84	178,75	Si	1,00E+18	3,4784	109	
	1	AlGaAs:Si	0,8499	0,1501	0,0000	68,86	305,56	Si	1,00E+18	3,0682	99	
3	**1**	AlGaInAs:Si	**0,1442**	**0,8508**	**0,0050**	60,83	182,90	Si	5,00E+17	3,4837	48	
	1	AlGaAs:Si	0,8498	0,1502	0,0000	68,84	305,45	Si	5,00E+17	3,0682	99	
1	**1**	AlGaAs:Si	**0,1400**	**0,8600**	**0,0000**	60,83	185,01	Si	5,00E+17	3,4864	17	
8	**1**	AlGaAs:Si	0,8499	0,1501	0,0000	206,50	916,29	Si	5,00E+17	3,0682	99	
	1	AlGaAs:Si	**0,1400**	**0,8600**	**0,0000**	182,50	555,03	Si	5,00E+17	3,4864	17	
5	**1**	AlGaAs	0,8498	0,1502	0,0000	68,84	305,45		0,00E+00	3,0682	99	
	1	AlGaAs	**0,1400**	**0,8600**	**0,0000**	60,59	184,28		0,00E+00	3,4864	17	

Pair number **22,5**

Total-thickness: 5290,27 nm

Thickness mirror: 4987,24 nm

Table C.2.: Epitaxy-structure of the semiconductor DBR with 22.5 pairs with the thickness of $\lambda/4$ und $3\lambda/4$. Maximum indium introduced in layers is 2.5 %.

	Wavelength:			845 nm								
Loop	**Loop**	**Material**	**x_Al**	**y_Ga**	**z_In**	**Thickness (nm)**	**Time(s)**	**Type**	**Dose**	**n**	**Pressure (Mpa)**	
	1	AlGaAs:Si	0,8549	0,1451	0,0000	303,03	1350,71	Si	1,00E+18	3,0655		**Etching stop 85% Al; 300nm**
3	**1**	AlGaInAs:Si	**0,1607**	**0,8143**	**0,0000**	60,84	174,61	Si	1,00E+18	3,4733	17	
	1	AlGaAs:Si	0,8499	0,1501	0,0000	68,86	305,56	Si	1,00E+18	3,0682	99	**ca. 85% Al**
3	**1**	AlGaInAs:Si	**0,1525**	**0,8325**	**0,0000**	60,84	178,75	Si	1,00E+18	3,4784	17	
	1	AlGaAs:Si	0,8499	0,1501	0,0000	68,86	305,56	Si	1,00E+18	3,0682	99	
3	**1**	AlGaInAs:Si	**0,1442**	**0,8508**	**0,0000**	60,83	182,90	Si	5,00E+17	3,4837	17	
	1	AlGaAs:Si	0,8498	0,1502	0,0000	68,84	305,45	Si	5,00E+17	3,0682	99	
1	**1**	AlGaAs:Si	**0,1400**	**0,8600**	**0,0000**	60,83	185,01	Si	5,00E+17	3,4864	17	
8	**1**	AlGaAs:Si	0,8499	0,1501	0,0000	206,50	916,29	Si	5,00E+17	3,0682	99	
	1	AlGaAs:Si	**0,1400**	**0,8600**	**0,0000**	182,50	555,03	Si	5,00E+17	3,4864	17	
5	**1**	AlGaAs	0,8498	0,1502	0,0000	68,84	305,45		0,00E+00	3,0682	99	
	1	AlGaAs	**0,1400**	**0,8600**	**0,0000**	60,59	184,28		0,00E+00	3,4864	17	
Pair number **22,5**		**Total thickness:**				**5290,27 nm**						
		Tickness mirror:				**4987,24 nm**						

Table C.3.: Epitaxy-structure of the semiconductor DBR with 22.5 pairs with the thickness of $\lambda/4$ und $3\lambda/4$. No indium has been inserted into the layers.

Wavelength: 845 nm

Loop	Loop	Material	x_Al	y_Ga	z_In	Thickness (nm)	Type	Dose	n	Pressure (Mpa)	
	1	AlGaAs:Si	0,8549	0,1451	0,0000	303,03	Si	1,00E+18	3,0655		**Etching stop 85% Al; 300nm**
2	**1**	AlGaInAs:Si	**0,1650**	**0,8050**	**0,0300**	60,89	Si	1,00E+18	3,4705	201	
	1	AlGaAs:Si	0,8499	0,1501	0,0000	68,86	Si	1,00E+18	3,0682	99	**ca. 85% Al**
1	**1**	AlGaInAs:Si	**0,1565**	**0,8235**	**0,0200**	60,89	Si	1,00E+18	3,4759	140	
	1	AlGaAs:Si	0,8499	0,1501	0,0000	68,86	Si	1,00E+18	3,0682	99	
1	**1**	AlGaAs:Si	**0,1400**	**0,8600**	**0,0000**	60,89	Si	1,00E+18	3,4864	17	
	1	AlGaAs:Si	0,8499	0,1501	0,0000	68,86	Si	1,00E+18	3,0682	99	
1	**1**	AlGaAs:Si	**0,1400**	**0,8600**	**0,0000**	60,89	Si	1,00E+18	3,4864	17	
1	**1**	Si_3N_4	#REF!	0,0000	0,0000	223,54		0,00E+00	1,8900	70	
8	**1**	SiO_2	**0,0000**	**0,0000**	**0,0000**	144,69		0,00E+00	1,4600	-120	
	1	Si_3N_4	0,0000	0,0000	0,0000	111,77		0,00E+00	1,8900	70	
Pair number		**Total thickness:**			**3157,6 nm**						
12,5		**Thickness mirror**			**2854,57 nm**						

Table C.4.: Epitaxy-structure of the hybrid DBR made of 4.5 semiconductor pairs and 8 dielectric pairs.

Wavelength: 850 nm					
Loop	Loop	Material	Thickness (nm)	n	Pressure (Mpa)
6	1	Si_3N_4	104,16	2,0400	250
	1	SiO_2	145,54	1,4600	100
6	1	Si_3N_4	109,53	1,9400	-75
	1	SiO_2	145,54	1,4600	100
1	1	Si_3N_4	109,53	1,9400	-75
Pair number: 12.5	Total thickness: 3000,13 nm				
	Thickness mirror: 3000,13 nm				

Table C.5.: Epitaxy-structure of the dielectric DBR made of 12.5 dielectric pairs.

D. VCSELs

VCSELs	p-top layer of Half-VCSEL	Oxide-aperture [µm]	Membrane	Air-Gap [µm]	RoC [mm]
A	3 nm	13	Semi.: λ/4 +3λ/4 layers	2.8	6.0
B	10 nm	13	Semi.: λ/4 +3λ/4 layers	3.0	5.5
C	3 nm	13	Semi.: λ/4 layers	5.5	3.0
D	3 nm	16	Semi.: λ/4 layers	5.0	3.0
E	3 nm	11	Dielec.: λ/4 layers	3.5	2.0
F	3 nm	12	Semi.: λ/4 layers	5.0	3.5
G	10 nm	11	Semi.: λ/4 layers	3.5	2.5
H	10nm + SWG	11	Semi.: λ/4 layers	3.5	2.5
I	3 nm	12	Semi.: λ/4 layers	5.5	3.0
J	3 nm	11	Semi.: λ/4 layers	5.0	2.5

Table D.1.: Different VCSELs which are developed and characterized in this work.

E. Tuning Speed

The thermal tuning model of a membrane (Fig. 4.1) can be approximately modeled by a first-order thermal RC low-pass filter shown in Fig. E.1(a). $R_{th} = L/(r_{th}\, A)$ is the thermal resistance

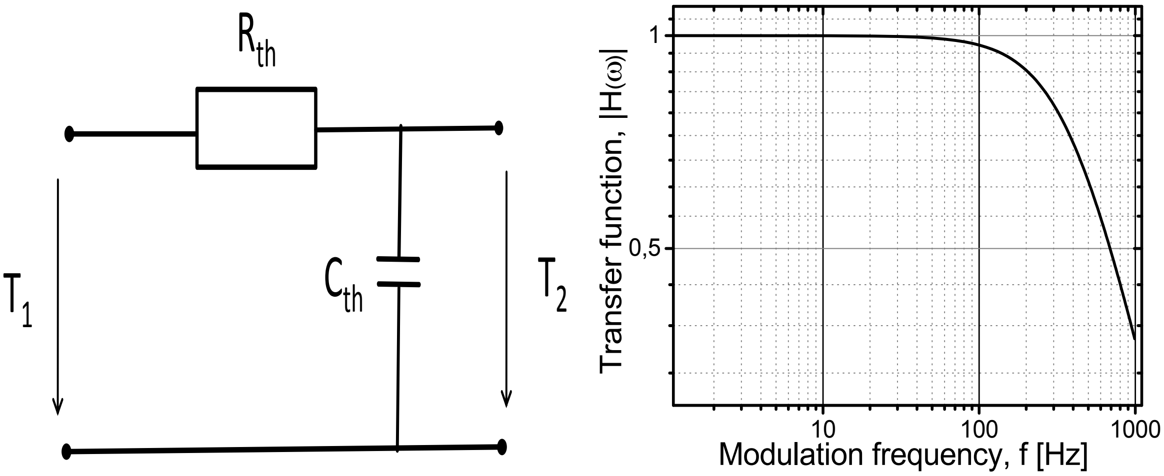

(a) (b)

Figure E.1.: (a) Block-diagram of the first-order thermal RC low-pass filter. (b) Transfer function of the first-order thermal RC low-pass filter.

with L as the beam length of the membrane, A is the cross section area and r_{th} is the specific heat conductivity. $C_{th} = m\, c_{th}$ is the thermal capacitance, where m is the mass of the membrane and c_{th} is the specific heat capacitance.

By using the equivalent electrical low-pass filter, the transfer function of the filter is given by:

$$|H(f)| = \frac{1}{\sqrt{1 + (2\pi\tau_{th})^2}}, \tag{E.1}$$

with $\tau_{th} = R_{th}C_{th}$ as the filter time constant. The 3 dB filter bandwidth (f_{3dB}) is obtained from τ_{th} by:

$$f_{\text{3dB}} = \frac{\sqrt{3}}{2\pi\tau_{th}}. \tag{E.2}$$

It can be seen that by decreasing L, R_{th} will decrease although τ_{th} and thus f_{3dB} will increase.

F. Far Field

As already discussed in Sec. 2.1.2, the laser beam propagates in Gaussian form (Fig. F.1). The beam waist of the Gaussian beam increases with the distance from the source according to Eq. 2.17. The first step to evaluate the far field is to calculate the beam waist of the Gaussian field at the distance of 20 cm (Fig. F.1) from the measured data (Sec. 5.5.2).

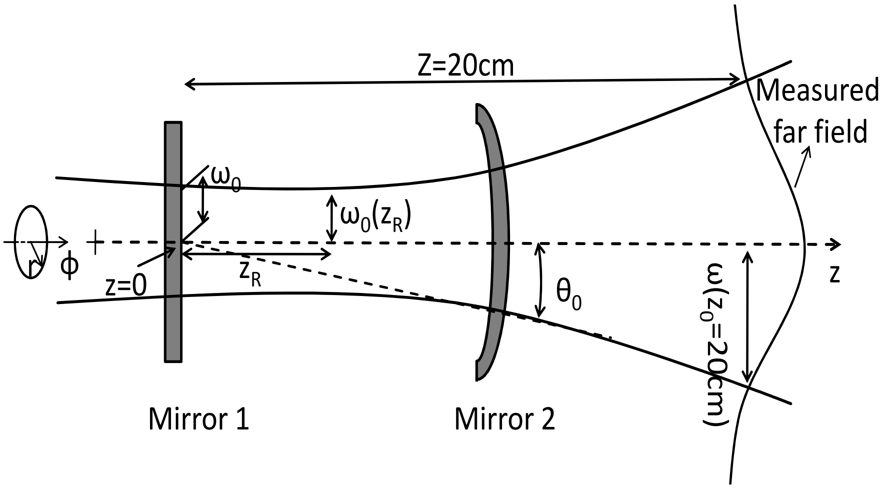

Figure F.1.: Propagation of the Gaussian beam.

The measurement setup measures the data in a spherical coordinate. By using the following equations, the data can be transformed in the Cartesian plane with x- and y-coordinates.

$$x = r\sin\theta\cos\phi, \tag{F.1}$$

$$y = r\sin\theta\sin\phi. \tag{F.2}$$

The next step is to calculate the beam waist of the measured beam. The beam waist ($\omega(z_0 = 20\text{cm})$) is defined as the distance from the center of the beam, in which the intensity of the field drops about $1/e^2$. By using the trigonometric realtions, due to $z_0 \gg z_r$ (Sec. 2.1.2) the divergence angle of the beam (Fig. F.1) can be obtained by:

$$\tan(\theta_0) = \frac{\omega(z_0)}{z_0} \quad \Rightarrow \quad \theta_0 = \arctan(\frac{\omega(z_0)}{z_0}). \tag{F.3}$$

By putting the θ_0 in Eq. 2.19, ω_0 can be obtained.

G. RIN

Due to the presence of other noise sources such as thermal noise and the shot noise of the photo receiver, the RIN should be extracted from the measured spectrum of ESA. The thermal noise of the setup is determined from the spectrum measurement in ESA, when the laser diode is off. The thermal noise can then be removed from the measured spectrum with the laser in operation. The remaining power spectrum density (PSD) includes the shot noise of the photo receiver and the RIN. It is given by $S(f) = 2F\{v(t)v(t-\tau)\}$ for $f > 0$ with the measurement resolution bandwidth (RBW) of 1 Hz, otherwise, the data have to be divided by RBW. $v(t) = GRp(t)$ is the input voltage of ESA, where $G[V/A]$ is the transimpedance gain and $R[A/W]$ is the responsivity of photo receiver. $p(t)$ includes the shot noise power and the intensity noise power. The PSD of the shot noise $S_s(f)$ is given by [72]:

$$S_s(f) = 2F\left\{G^2\left\langle i_s(t)i_s(t-\tau)\right\rangle\right\} = 2G^2RP_0q \quad for \;\; f > 0, \tag{G.1}$$

where P_0 is the average optical power, q is the elementary charge and $i_s(t)$ is the shot noise current. By subtracting the calculated shot noise from the measurement the remaining spectrum is $S_n(f) = S(f) - S_s(f)$. The $S_n(f)$ is given as:

$$S_n(f) = 2F\left\{\left\langle v_n(t)v_n(t-\tau)\right\rangle\right\} = 2F\left\{\left\langle G^2R^2p_n(t)p_n(t-\tau)\right\rangle\right\} \quad for \;\; f > 0, \tag{G.2}$$

where $v_n(t)$ is the voltage fluctuations and $p_n(t)$ is the intensity fluctuations due to intensity noise. The RIN was then extracted from $S_n(f)$ with :

$$RIN(f) = \frac{2F\left\{\left\langle p_n(t)p_n(t-\tau)\right\rangle\right\}}{P_0^2} = \frac{S_n(f)}{P_0^2G^2R^2} \quad for \;\; f > 0. \tag{G.3}$$

In the above calculations the noise terms are assumed to be statistically independent.

Acronyms

AM Amplitude modulation

AFM Atomic force microscope

BCB Benzo-Cyclo-butene

CST Computer simulation technology

DBR Distributed Bragg reflector

DH Double hetero

EBL Electron beam lithography

FP Fabry-Pérot

FSR Free-spectral-range

FWHM Full-width half-maximum

GAN Global area network

GPIB General purpose interface bus

HREM High resolution electron microscope

LAN Local area network

MAN Metropolitan area network

MASER Microwave amplification by stimulated emission of radiation

MBE Molecular beam epitaxy

MEMS Micro-electro-mechanical system

OPC Optical proximity correction

OSA Optical spectrum analyzer

PECVD Plasma-enhanced chemical vapor deposition

PIV Power-current-voltage

PMSR Polarization-mode suppression ratio

PSD Power spectrum density

QW Quantum wells

RBW Resolution bandwidth

RIE Reactive ion etching

RIN Relative intensity noise

RoC Radius of curvature

RTA Rapid thermal annealing

SMSR Side-mode suppression ratio

SOB Selective optical broadcast component

SWG Sub-wavelength grating

TEM Transverse electro magnetic

WAN Wide area network

WDM Wavelength devision multiplex

Bibliography

[1] A. Mutig, “High speed VCSELs for optical interconnects”, Dissertation D 83, TU Berlin, Berlin, Germany, 2010.

[2] J. Hecht, “Laser pioneers”, ISBN 0 12-336030-7, Academic press, USA, 1991.

[3] H. Soda, K. Iga, C. Kitahara and Y. Suematsu, “GaInAsP/InP surface emitting injection lasers”, Jpn. j. appl. phys., Vol. 18, pp.2329-2330, 1979.

[4] J. Y. Law, “Static, dynamic, and noise characteristics of vertical-cavity surface-emitting lasers”, Dissertation, University of Rochester, Rochester, New York, 1997.

[5] F. Koyama, S. Kinoshita and K. Iga, “Room-temperature continuous wave lasing characteristics of GaAs vertical cavity surface-emitting laser”, Appl. phys. lett., Vol. 55, no. 3, pp.221-222, Jul. 1989.

[6] G. P. Agrawal, “Semiconductor lasers: past, present and future”, AIP Press, Woodbury, New York, USA, 1995.

[7] M. C. Larson, “Microelectromechanical wavelength-tunable vertical-cavity light-emitters and lasers”, Dissertation UMI 9630338, Michigan, USA, 1996.

[8] L. Fan, M. C. Wu, H. C. Lee and P. Gordzinski, “10.1 nm range continuous wavelength-tunable vertical-cavity surface-emitting lasers”, Electron. lett., Vol. 30, no. 17, pp.1409-1410, 1994.

[9] P. Wang, P. Tayebati, D. Vakhshoori, C-C Lu, and M. Azimi, “Half-symmetric cavity microelectromechanically tunable vertical cavity surface emitting lasers with single spatial mode operating near 950 nm”, Appl. phys. lett., Vol. 75, no. 7, pp.897-898, 1999.

[10] W. Yuen, G. S. Li, R. F. Nabiev, M. Jansen, D. Davis, and C. J. Chang-Hasnain, “Electrically-pumped directly-modulated tunable VCSEL for metro DWDM applications”, proc. 14th Annu. Meeting lasers elektro-optics society, Vol. 1, pp.70-71, 2001.

[11] H. A. Davani, C. Grasse, B. Kögel, P. Westbergh, C. Gierl, K. Zogal, S. Jatta, G. Böhm, T. Gründl, P. Meissner, A. Larsson and M-C. Amann, “Widely tunable high-speed bulk-micromachined short-wavelength MEMS-VCSEL”, IEEE semiconductor laser conference 2010, Tokyo, Japan, pp.9-10, 2010.

[12] A. Benner, “Cost-effective optics: enabling the exascale roadmaps”, 17^{th} Annual IEEE symposium on high-performance interconnects, New York, USA, August 2009.

[13] R. R. Patel, S. W. Bond, M. D. Pocha, H. E. Garrett, R. F. Drayton, H. E. Peterson, D. M. Krol, R. J. Deri, M. E. Lowry, “Multiwavelength parallel optical interconnects for massively parallel processing”, Selected topics in quantum electronics, Vol. 9, Issue 2, pp.657-666, 2003.

[14] I. Artundo, L. Desmet, W. Heirman, C. Debaes, J. Dambre, J. M. Van Campenhout, H. Thienpont, “Selective optical broadcast component for reconfigurable multiprocessor interconnects”, Selected topics in quantum electronics, Vol. 12, Issue 4, pp.828-837, 2006.

[15] M. C. Larson, A. R. Massengale and J. s. Harris, “Broadly tunable resonant-cavity light-emitting diode”, IEEE Photonics technol. Lett., Vol. 7, no. 11, pp.1267-9, 1995.

[16] M. C. Larson, F. Sugihwo, A. R. Massengale and J. s. Harris, “Micromachined tunable vertical-cavity surface-emitting lasers”, Jour. Electron meeting IEDM, pp. 405-408, 1996.

[17] M. Ortsiefer, “Langwellige Vertikalresonator-Laserdioden im Materialsystem InGaAlAs/InP”, Dissartation ISBN 3-932749-35-9, TU-München, München, Germany 2001.

[18] H. Hogelink and T. Li, “Laser beams and resonator”, Applied Optics, pp.1550-1566, 1966.

[19] G. D. Boyd and H. Kogelink, “Generalized confocal resonator theory”, Bell Systems Technical Journal, Vol. 41, pp.1347-1369, 1962.

[20] A. Halbritter, “Entwicklung und Charakterisierung mikromechanisch abstimmbarer Komponenten fr optische Kommunikationssysteme”, Dissertation D17, TU Darmstadt, Shaker, aachen, Germany, 2005.

[21] N. Hodgson, H. Weber, “Laser resonators and beam propagation”, Springer, NY, USA, 2005.

[22] A. G. Fox and T. Li, “Resonant modes in a master interferometer”, Bell Systems Technical Journal, Vol. 40, pp.453-488, 1961.

[23] N. Hodgson, H. Weber, “Optische Resonatoren”, Springer, Berlin, Heidelberg, Germany, 1992.

[24] M. Ortsiefer, M. Grau, J. Rosskopf, R. Shau, K. Windhorn, E. Rönneberg, G. Bohm, W. Hofmann, O. Dier and M. -C. Amann. “InP-based VCSELs with buried tunnel junction for optical communication and sensing in the 1.32.3 mm wavelength range”, Proc. IEEE Int. Semiconductor Laser Conf., pp.113-114, 2006.

[25] B. W. Kögel, “Mikromechanisch weit abstimmbare Oberflchen-emittierende Laserdioden fr Sensoranwendungen”, Dissertation D17, TU Darmstadt, Cuvillier, Göttingen, Germany, 2009.

[26] D.I. Babic and S. W. Corzine, “Analytic expressions for the reflection delay, penetration depth and absorptance of quarter-wave dielectric mirrors” in Journal of Quantum Electron., Vol. 28, no. 2, pp.514-524, 1992.

[27] S. W. Corzine, R. S. Geels, J. W. Scott, R.-H. Yan and L. A. Coldren, “Design of Fabry-Pérot surface-emitting lasers with a periodic gain structure”, Journal of Quantum Electronics, Vol. 25, no. 6, pp.1513-1524, 1998.

[28] L. A. Coldren, S. W. Corzine, “Diode lasers and photonic integrated circuits”, John Wiley & Sons, NY, USA, 1995.

[29] C. Wilmsen, H. Temkin and L. A. Coldren, “Vertical-cavity surface-emitting lasers”, Cambridge University Press, Cambridge, UK, , 1999.

[30] H. Li, K. Iga, “Vertical-cavity surface-emitting laser devices”, Springer-Verlag, Berlin Heidelberg, Germany, 2003.

[31] R. Michalzik, “VCSELs”, Springer ISBN-13: 978-3642249853, 2013.

[32] R. Nagarajan, M. Ishikawa, T. Fukushima, R. S. Geels, J. E. Bowers, “High speed quantum-well lasers and carrier transport effects”, IEEE J. quantum electron., Vol. 28, Issue 10, pp.1990-2008, 1992.

[33] C. Carlsson, H. Martinsson, R. Schatz, J. Halonen and A. Larsson, “Analog modulation of oxide confined VCSELs at microwave frequencies”, Journal of lightwave technologies, Vol. 20, Issue 9. pp.1740-1749, 2002.

[34] R. S. Tucker, “High-speed modulation of semiconductor lasers”, IEEE transactions on electron devices, Vol. ED-32, No. 12 pp.2572-2684, 1985.

[35] O. Kjebon, R. Schatz, S. Lourdudoss, S. Nilsson and B. Stålnack, “Modulation response measurements and evaluation of MQW InGaAsP laser of various designs”, SPIE proc., Vol. 2684, pp.138-152, 1996.

[36] K. Y. Lau, N. Bar-Chaim, I. Ury, Ch. Harder and A. Yarif, “Direct amplitude modulation of short-cavity GaAs lasers up to X-band frequencies”, Applied physics letters, Vol. 43, pp.1-3, 1983.

[37] D. Wiedenmann, R. King, C. Jung, R. Jäger, R. Michalzik, P. Schnizer, M. Kicherer, K. J. Ebeling, “Design and analysis of single-mode oxidized VCSEL’s for high-speed optical interconnects ”, IEEE j. sel. top. quantum electron, Vol. 5, pp.503-511, 1999.

[38] M. S. Demokan, A. Nacaroglu, “An analysis of gain-switched semiconductor lasers generating pilse-code-modulated light with a high bit rate”, IEEE J. quantum electron., Vol. QE-20, pp.1016-1022, 1984.

[39] R. S. Tucker, “Large-signal switching transients in index-guided semiconductor lasers”, Electron. lett., Vol. 20, pp.802-803, 1984.

[40] K. Petermann, “Laser diode modulation and noise”, Kluwer Academic Publishers, Dordrecht, Boston, London, 1988.

[41] C. Jung, R. Jäger, M. Grabbher, P. Schnitzer, R. Michalzik, B. Weigl, S. Muller, and K.J. Ebeling, “4.8 mW singlemode oxide confined top-surface emitting vertical-cavity laser diodes”, Electron. lett., Vol. 33. pp.1790-1791, 1997.

[42] H. J. Unold, M. C. Riedl, S. W. Z. Mahmoud, R. Jäger and K.J. Ebeling, “Long monolithic cavity VCSELs for high singlemode output power”, Electron. lett., Vol. 37, pp.178-179, 2001.

[43] H. P. D. Yang, I. C. Hsu, F.I. Lai, G. Lin, R.S. Hsiao, N. A. Maleev, S. A. Blokhin, H.C. Kuo, S. C. Wang and J. Y. Chi, “Single-mode InGaAs submonolayer quantum dot photonic crystal VCSELs”, Semicond. sci. technol., Vol. 21, pp.1176-1180, 2006.

[44] A. Furukawa, S. Sasaki, M. Hoshi, A. Matsuzono, K. Moritoh and T. Baba, “High-power single-mode vertical-cavity surface-emitting lasers with triangular holey structure”, Appl. phys. lett., Vol. 85, pp.5161-5163, 2004.

[45] Å. Haglund, J. S. Gustavsson, J. Vukusic, P. Modh, P. Jedrasik and A. Larsson, “Single fundamental mode output power exceeding 6 mW from VCSELs with a shallow surface relief”, IEEE photon. technol. lett., Vol. 16, pp.368-370, 2004.

[46] J. S. Gustavsson, Å. Haglund, E. Söderberg S, J. Vukusic, P. Modh, P. Jedrasik and A. Larsson, “Mode and polarization control in VCSELs using shallow surface structures”, Optoelectrinics, IET, Vol. 1, No. 5. pp.197-205, 2007.

[47] S. L. Chuang, “Physics of optoelectronic devices”, John Wiley & Sons, NY, USA, 1995.

[48] G: Verschaffelt, K. Panajotov, J. Albert, B. Nagler, M. Peeters, J. Danckaert, I. Veretennicoff and H. Thienpont, “Polarisation switching in vertical-cavity surface-emitting lasers: from experimental observations to applications”, Opto. electronics review, Vol. 9, pp.257-268, 2001.

[49] M. Takahashi, N. Egami, T. Mukaihara, F. Koyama and K. Iga,“Lasing characteristics of GaAs(311)A substrate based In GaAs-GaAs vertical-cavity surface-emitting lasers”, IEEE jour. sel. top. quantum electron., Vol. 3, pp.372-378, 1997.

[50] N. Nishiyama, M. Arai, S. Shinada, M. Azushi, T. Miyamoto, F. Koyama and K. Iga, “Highly strained GaInAs-GaAs quantum-well vertical-cavity surface-emitting laser on GaAs (311)B substrate for stable polarization operation”, IEEE j. sel. top. quantum electron., Vol. 7, pp.242-248, 2001.

[51] G. Verschaffelt, W. van der Vleuten, M. Creusen, E. Smalbrugge, T.G. van de Roer, F. Karouta, R.C. Strijbos, J. Veretennicoff, B. Ryvkin, H. Thienpont and G. A. Acket, “Polarization stabilization in vertical-cavity surface-emitting lasers through asymetric current injection”, IEEE photon. technol. lett., Vol. 12, pp.945-947, 2000.

[52] L. J. Sargent, J. M. Rorison, M. Kuball, R. V. Penty, I. H. White, S. W. Corzine, M. R. T. Tan, S. Y. Wang and P. J. Heard, “Investigation of polarization pinning mechanism in deep-line-etched vertical-cavity surface-emitting lasers”, Appl. phys. lett., Vol. 76, pp. 400-402, 2000.

[53] F. Monti di Sopra, M. Brunner and R. Hovel, “Polarization control in strained T-bar VCSELs”, IEEE photon. technol. lett., Vol. 14, pp. 1034-1036, 2002.

[54] J. S. Gustavsson, Å. Haglund, J. Vukusic, J. Bengtsson, P. Jedrasik and A. Larsson, “Efficient and individually controllable mechanisms for mode and polarization selection in VCSELs, based on a common, localiezed, sub-wavelength surface grating”, Opt. express, Vol. 13, No. 17. August, 2005.

[55] P. Debernardi, and G. P. Bava, “Coupled mode theory: a powerful tool for analyzing complex VCSELs and designing advances features” IEEE jour. selected topics quantum electron., optoelectronic devices simulation, Vol. 9, No. 3., pp. 905-917, 2003.

[56] P. Westbergh, J. S. Gustavsson, Å. Haglund, M. Sköld and A. Larsson, “High-peed, low-current-density 850nm VCSEL”, Jour. sel. top. quantum electron, Vol. 15, No. 3. pp. 694-703, 2009.

[57] F. Riemenschneider, I. Sagnes, G. Böhm, H. Halbritter, M. Maute, C. Symonds, M.-C. Amann and Peter Meissner, “A new concept for tunable long wavelength VCSELs”, Optics communications, Vol. 222, pp. 341-350, July 2003.

[58] C. Gierl, T. Gruendl, P. Debernardi, K. Zogal, C. Grasse, H. A. Davani, G. Böhm, S. Jatta, F. Küppers, P. Meissner and M. -C. Amann, “Surface micromachined tunable 1.55 μm-VCSEL with 102 nm continuaous single-mode tuning ”, Optics express, Vol. 19, Issue 18, pp.17336-17343, 2011.

[59] S. L. Wright, T.N. Jackson and R. F. Marks, “ Apparent temperature oscillations during molecular beam epitaxy: A useful interferometric effect”, Journal of vacuum science and technology, Vol 8, Nr 2, Mar/Apr 1990.

[60] F. Riemenschneider, “Mikromechanisch abstimmbare, vertikal emittierende Laserdioden”, Dissertation D17, TU Darmstadt, Darmstadt, Germany, 2008.

[61] F. Riemenschneider, M. Aziz, H. Halbritter, I. Sagnes and Peter Meissner, “Low-cost electrothermally tunable optical microcavities based on GaAs”, IEEE photonics tech. letters, Vol. 14, pp. 1566-1568, November 2002.

[62] S. M. Jatta, “Plasmaunterstützende Abscheidung von dielektrischen Schichten zur Entwicklung von mikromechanisch abstimmbaren optischen Komponenten”, Dissertation D 17, TU Darmstadt, Darmstadt, Germany, 2010.

[63] F. Sugihwo, M. C. Larson and J. S. Harris, “Micromachined widely tunable vertical cavity laser diodes”, J. michroelectromech. syst., Vol. 7, no. 1, pp.48-55, 1998.

[64] F. Sugihwo, M. C. Larson and J. S. Harris, “Micromachined widely tunable vertical cavity laser diodes”, J. michroelectromech. syst., Vol. 7, no. 1, pp.48-55, 1998.

[65] H. A. Davani, C. Grasse, B. Kögel, C. Gierl, K. Zogal, T. Gründl, P. Westbergh, S. Jatta, G. Böhm, P. Meissner, A. Larsson and M-C. Amann, “Widely tunable high-speed bulk-micromachined short-wavelength MEMS-VCSEL”, Conference on lasers and electro-optics/pacific rim, pC829, 2011.

[66] F.Riemenschneider, M. Maute, H. Halbritter, G. Böhm, M.-C. Amann and P. Meissner, “Continuously tunable long-wavelength MEMS-VCSEL with over 40-nm tuning range”, IEEE photonics tech.letters, Vol. 16, no. 10, pp. 2212-2214, Okt. 2004.

[67] H. Halbritter, C. Sydlo, B. KKögel, F. Riemenschneider, H. Ludwig, P. Meissner, “Impact of micromechanics on the linewidth and chirp performance of MEMS-VCSELs”, IEEE journal of selected topics in quantum electronics, VOL. 13, NO. 2, March/April 2007.

[68] B. Kögel, H. Halbritter, S. Jatta, P. Meissner, M. Maute, G. Bohm, M. -C. Amann, “Linewidth of electrically pumped long-wavelength MEMS VCSELs”, CLEO-IQEC 2007, pp. 17-22 June 2007.

[69] T. Ida, M. Ando and H. Toraya, “Extended pseudo-Voigt function for approximating the Voigt profile”, Journal of applied crystallography, ISSN 0021-8898.

[70] C. Gierl, T. Gruendl, K. Zogal, C. Grasse, H. A. Davani, G. Böhm, M. -C. Amann, P. Meissner, F. Küppers, “Linewidth of surface micro-machined MEMS tunable VCSELs at 1.5 μm”, CLEO-IQEC 2012, 2012.

[71] H. A. Davani, B. Kögel, P. Debernardi, C. Grasse, C. Gierl, K. Zogal, Å. Haglund, J. S. Gustavsson, P. Westbergh, T. Gründl, P. Komissinski, T. Bitsch, L. Alff, F. Küppers, A. Larsson, M. -C. Amann and P. Meissner, “Polarization investigation of a tunable high-speed short-wavelength bulk-micromachined MEMS-VCSEL”, SPIE 2012, San Francisco, USA,Proc. SPIE 8276, 82760T (2012).

[72] S. Botacchi, “Noise and signal interference in optical fiber transmission systems”, Willey, NY, USA, 2008.

[73] Amnon Yariv, “Optical electronics”, Holt, Rinehart, Winston, USA, 1971.

[74] B. Kögel, P. Westbergh, Å. Haglund, J. S. Gustavsson, A. Larsson, “Integrated MEMS-tunable VCSELs with modulation bandwidth”, Electronics letters, Vol. 47, No. 13 (2011).

[75] B. Kögel, P. Debernardi, P. Westbergh, J. S. Gustavsson, Å. Haglund, E. Haglund, J. Bengtsson, A. Larsson, “Integrated MEMS-Tunable VCSELs Using a Self-Aligned Reflow Process”, IEEE journal of quantum electronics, Vol. 48, no. 2, pp. 144-152 (2012).

Publications

1. H. A. Davani, C. Grasse, B. Kögel, P. Westbergh, C. Gierl, K. Zogal, S. Jatta, G. Böhm, T. Gründl, P. Meissner, A. Larsson and M-C. Amann. “Widely tunable high-speed bulk-micromachined short-wavelength MEMS-VCSEL”, IEEE semiconductor laser conference 2010, Tokyo, Japan, pp.9-10, 2010.

2. H. A. Davani, C. Grasse, B. Kögel, C. Gierl, K. Zogal, T. Gründl, P. Westbergh, S. Jatta, G. Böhm, P. Meissner, A. Larsson and M-C. Amann. “Widely tunable high-speed bulk-micromachined short-wavelength MEMS-VCSEL”, Conference on lasers and electro-optics/pacific rim, pC829, 2011.

3. H. A. Davani, B. Kögel, P. Debernardi, C. Grasse, C. Gierl, K. Zogal, Å. Haglund, J. S. Gustavsson, P. Westbergh, T. Gründl, P. Komissinski, T. Bitsch, L. Alff, F. Küppers, A. Larsson, M. -C. Amann and P. Meissner. “Polarization investigation of a tunable high-speed short-wavelength bulk-micromachined MEMS-VCSEL”, SPIE 2012, San Francisco, USA, Proc. SPIE 8276, 82760T (2012).

4. C. Gierl, T. Gruendl, P. Debernardi, K. Zogal, C. Grasse, H. A. Davani, G. Böhm, S. Jatta, F. Küppers, P. Meissner and M. -C. Amann“Surface micromachined tunable 1.55 μm-VCSEL with 102 nm continuaous single-mode tuning ”, Optics Express, Vol. 19, Issue 18, pp.17336-17343, 2011.

5. C. Gierl, T. Gruendl, K. Zogal, C. Grasse, H. A. Davani, G. Böhm, M. -C. Amann, P. Meissner, F. Küppers“Linewidth of surface micro-machined MEMS tunable VCSELs at 1.5 μm”, CLEO-Science and innovation, ISBN: 978-1-55752-943-5, San Jose, 2012.

6. C. Gierl, G. D. Cole, B. Kögel, S. Jatta, K. Zogal, H. A. Davani, P. Meissner “Mechanical properties of a movable micro-mirror membrane for electro-statically tunable optical filters and vertical-cavity surface-emitting lasers”, European conference on laser and electro-optics (CLEO/Europa), Paper CB.P.5, Munich, Germany, Jun. 2009.

7. C. Gierl, K. Zogal, H. A. Davani, P. Meissner “Electro thermal and electro statical actuation of a surface micromachined tunable Fabry-Perot filter”, Quantum electronics and laser science conference CLEO, ISBN: 978-1-55752-910-7, Baltimore, Maryland, USA, 2011.

8. C. Gierl, K. Zogal, S. Jatta, H. A. Davani, F. Küppers, P. Meissner, T. Gruendl, C. Grasse, M. -C. Amann, A. Daly, B. Corbett, B. Kögel, A. Haglund, J. Gustavsson, P. Westbergh, A. Larsson, P, Debernardi, M. Ortsiefer “Tunable VCSEL aiming for the application in interconnects and short haul systems”, SPIE Photonics west, Vol. 7959, 795908 San Francisco, CA, USA, 2011.

9. K. Zogal, C. Gierl, H. A. Davani, C. Grasse, M. Maute, P. Meissner, M. -C. Amann “Tuning dynamics of a $>$70 nm continuously tunable MEMS-VCSEL with a hybrid curved mirror”, European conference on laser and electro-optics, ISBN: 978-1-4577-0532-8, Munich, Germany 2011.

10. K. Zogal, T. Gruendl, H. A. Davani, C. Gierl, S. Jatta, C. Grasse, M. -C. Amann, P. Meissner “High speed modulation of a 1.55-μm MEMS-tunable VCSEL”, Quantum electronics and laser science conference CLEO, ISBN: 978-1-55752-910-7, Baltimore, Maryland, USA, 2011.

11. C. Gierl, T. Gruendl, K. Zogal, H. A. Davani, C. Grasse, G. Boehm, F. Kueppers, P. Meissner, M. -C. Amann “Surface micromachined MEMS-tunable VCSELs with wide and fast wavelength tuning”, Electronic letters, Vol. 47, Issue 22, pp. 1242-1243, 2011.

12. C. Gierl, T. Gruendl, P. Debernardi, K. Zogal, H. A. Davani, C. Grasse, G. Boehm, F. Kueppers, P. Meissner, M. -C. Amann “Surface micromachined MEMS tunable VCSEL at 1550 nm with $>$60 nm single mode tuning”, SPIE photonics west, Paper 8276-26, 2012.

13. K. Zogal, T. Gruendl, H. A. Davani, C. Gierl, C. Grasse, , M. -C. Amann, F. Kueppers, P. Meissner “1.55-μm high-speed MEMS-tunable VCSEL”, SPIE Photonics west, Paper 8276-26, 2012.

14. K. Zogal, T. Gruendl, C. Gierl, C. Grasse, H. A. Davani, G. Boehm, M. -C. Amann, F. Kueppers, P. Meissner “Singlemode 50 nm tunable surface micro-machined MEMS-VCSEL operation at 1.95 μm”, Lasers and electro-optics conference CLEO, ISBN: 978-1-4673-1839-6, San Jose, USA,2012.

Curriculum Vitae

Personal information:

Name: Hooman Abdollahzadeh Davani
Date of birth: 05.April.1981
Place of birth: Tehran

Education and training:

10.2001 - 03.2008	Studying electronics and information technology with the focus on optical communications in technical faculty of Christian-Albrechts-Universitt zu Kiel Germany (Dipl. Ing. 2008).
11.2007 - 05.2008	Industrial internship in photonics research and development department of Ericsson GmbH in Backnang Germany.

Work experience:

08.2008 - 04.2012	Research assistant in institute of microwaves and photonics of TU Darmstadt Germany.
01.2013 - 02.2015	Project management and system Ing. in ifm syntron GmbH in Tettnang Germany.